

REPORT DOCUMENTATION PAGE

AFRL-SR-BL-TR-99-

0050

a source
ict of this
5 Jeffersc

Public reporting burden for this collection of information is estimated to average 1 hour per response, including gathering and maintaining the data needed, and completing and reviewing the collection of information. Send collection of information, including suggestions for reducing this burden, to Washington Headquarters Service, Davis Highway, Suite 1204, Arlington, VA 22202-4302, and to the Office of Management and Budget, Paperwork

1. AGENCY USE ONLY (Leave Blank)		2. REPORT DATE 1 February, 1999	3. REPORT TYPE AND DATES COVERED Final Technical, 7/1/96 - 11/30/99	
4. TITLE AND SUBTITLE Modeling Primary Atomization Processes			5. FUNDING NUMBERS F49620-96-1-0239	
6. AUTHOR(S) Stephen D. Heister				
7. PERFORMING ORGANIZATION NAME(S) AND ADDRESS(ES) School of Aeronautics & Astronautics Purdue University 1282 Grissom Hall West Lafayette, IN 47907-1282			8. PERFORMING ORGANIZATION REPORT NUMBER	
9. SPONSORING / MONITORING AGENCY NAME(S) AND ADDRESS(ES) AFOSR/NA 801 N. Randolph Road, Room 732 Arlington, VA 22203-1977			10. SPONSORING / MONITORING AGENCY REPORT NUMBER	
11. SUPPLEMENTARY NOTES				
12a. DISTRIBUTION / AVAILABILITY STATEMENT Approved for public release; distribution is unlimited.			12b. DISTRIBUTION CODE	
13. ABSTRACT (Maximum 200 words) <p>The contributions of atomization processes to combustion instabilities in liquid rocket engines has been assessed via a series of analytic/numerical models. Simulations of high-speed injection of a viscous jet have revealed a jet "swelling" phenomenon for the first time. Modeling of F-1 fuel injectors reveals a potential instability of the fuel columns to transverse acoustic modes in injector designs which showed large instabilities.</p> <p>Limited experimental work relevant to hybrid rocket injection has also been accomplished under the subject program. A new consumable, catalytic igniter has shown to provide reliable, reproducible ignition in hydrogen peroxide/polyethylene hybrid engines. Currently, a complete dense spray simulation tool is under development to assess spray dynamics under time-varying chamber conditions.</p>				
14. SUBJECT TERMS atomization, liquid rocket engines, hybrid rockets, combustion instability			15. NUMBER OF PAGES 124	
			16. PRICE CODE	
17. SECURITY CLASSIFICATION OF REPORT unclassified	18. SECURITY CLASSIFICATION OF THIS PAGE unclassified	19. SECURITY CLASSIFICATION OF ABSTRACT unclassified	20. LIMITATION OF ABSTRACT UL	

NSN 7540-01-280-5500

Standard Form 298 (Rev. 2-89)
Prescribed by ANSI Std. Z39-18
298-102

AFOSR Contract F49620-96-1-0239

MODELING PRIMARY ATOMIZATION PROCESSES

Stephen D. Heister, Associate Professor
School of Aeronautics and Astronautics
Purdue University
1282 Grissom Hall
West Lafayette, IN 47907

1 February 1999

Final Technical Report for Period 1 July 1996 - 30 November 1998

Approved for Public Release,
Distribution is Unlimited

Prepared for:
AFOSR/NA
Attn. Dr. Mitat Birkin
801 N. Randolph Rd. Room 732
Arlington, VA 22203-1977

19990302045

Contents

1	Summary	2
2	Research Objectives	2
3	Status of the Research	2
3.1	Simulation of High-Speed Viscous Jets	3
3.2	Simulation of F-1 Engine Tangential-Mode Instability	3
3.3	Hybrid Rocket Injection Experimental Research	6
3.4	Development of a 3-D BEM Code	6
3.5	Development of a Dense Spray Model	7
4	Professional Activities	10
4.1	Technology Transfer/Coupling Activities	12
5	Appendix A - Viscous Jet Simulations	13
6	Appendix B - F-1 Engine Simulations	36
7	Appendix C - Hybrid Rocket Injection/Combustion Tests	54
8	Appendix D - 3-D Boundary Element Model Development	74
9	Appendix E - Dense Spray Model Description	114

1 Summary

This research program has focused on enhancing the understanding of jet atomization processes and their contribution to combustion instabilities in liquid rocket engines. During the past three years, progress has been made in understanding the role of the atomization process in tangential-mode instabilities in the F-1 engine through the use of Boundary Element Method (BEM) codes developed with previous AFOSR sponsorship. Another important research discovery resulted in the completion of a zonal model capable of addressing viscous forces at the periphery of the high-speed jet. Through the use of this model, a *jet swelling* phenomenon has been fully characterized; its influence on the atomization process is believed to be profound.

In addition, two new major code developments have been initiated during the subject contract. A fully three-dimensional, nonlinear, unsteady BEM code has been developed and validated for use in future atomization simulations. This development represents a major milestone in that “real world” atomization processes are highly three dimensional.

A second new development, initiated in the last few months of the studies, involves a totally new approach to simulating atomization problems. Through the use of a fictitious fluid “pseudo-density” which reflects the local void fraction in the two-phase mixture, very complex atomization problems can be tackled. In the model currently under development, we project a capability to track over 100,000 individual droplets. In addition, each drop is subject to deformation from the gas-phase dynamic pressure forces, to secondary atomization, and to possible collisions with other droplets. Data for these basic subprocesses is derived from research results directly obtained by others supported in AFOSR’s propulsion research program.

2 Research Objectives

The understanding of the complex combustion phenomena present in liquid rocket engines begins with the fundamental process of fuel and oxidizer jet atomization. The objective of this research has been to develop a series of models, incorporating increasingly complex physics, to assess the role of atomization in the combustion instability process. The models have centered on the use of Boundary Element Methods (BEMs) as a means to provide accurate description of these complex, nonlinear processes under arbitrary unsteady conditions. The models have demonstrated a capability to have calculations proceed *beyond atomization events*.

While the basic BEM techniques are inviscid, recent development of a zonal model using an integral method for boundary layer modeling, permits a full viscous capability. This model, described in Appendix A of this report, is the first primary atomization model to provide accurate, fully nonlinear treatment of atomization processes under full-scale Reynolds numbers consistent with actual engine conditions. While these BEM simulations have been useful in describing parent surfaces of modest complexity, other techniques are required to resolve dense sprays formed in many rocket injection processes. For this reason, we have embarked on the development of a viscous, unsteady, nonlinear model capable of addressing flows in which large numbers of droplets are present.

3 Status of the Research

Four major tasks have been accomplished in the research project over the past three years. A viscous BEM simulation of a high-speed jet, such as those employed in rocket injectors, has been completed and documented in the open literature. This study is summarized in Section 3.1. Simulations pertaining to the stability of the F-1 injector have been completed; these results are summarized in Section 3.2. In Section 3.3 we highlight some experimental results obtained in the hybrid rocket injection analysis, while Section 3.4 provides a insight into the new 3-D BEM code which has recently been completed. Finally, we conclude the research status by providing a description and sample results from the new dense spray model which is still under development.

Table 1: F-1 Injector Design Data: Fuel Orifice Test Data

Injector Designation	Orifice			
	Diam. mm	ω_g , Hz	$\Delta P/P_c$ %	ω_g/ω_n
5U-Flatface	3.66	538	150	3.0
5U-Baffled	4.04	460	65	2.9
Double Row Cluster (DRC)	2.79	454	400	1.7
Prelim. Flight Rating Tests (PFRT)	5.79	-	0	5.1*
Flight Rating Test (FRT)	7.14	-	0	7.1*

* Assumes $\omega_g = 460$ Hz 1T chamber mode.

3.1 Simulation of High-Speed Viscous Jets

An unsteady, axisymmetric BEM-based model was developed. The model included an unsteady integral treatment of the thin boundary layer near the liquid/wall and gas/liquid boundary. The most remarkable aspect of these solutions is that they all exhibit a “swelling” in the region very near the orifice exit plane. Physically, the swelling is caused by the fluids transition from a “no-slip” boundary condition inside the orifice, to a free-surface boundary condition outside the nozzle. Figure 1 provides a schematic representation of the predicted jet surface shape in the region near the orifice exit. We have found that the amount of swelling is dependent on the thickness of the boundary layer at the orifice exit plane as illustrated in Fig. 2. Experimental verification of this process is very difficult because it represents a small change (only a few percent) in jet diameter in a region which is normally obscured by droplets. However, we are currently working on indirect verification of the results by correlating our predictions with jet cone angles, breakup lengths, and other measurable parameters.

These results have improved our understanding of the atomization process and how the current theories illustrated in Fig. 1 contribute to this process. In the presence of a gas-phase, the swelling of the jet provides a large-amplitude disturbance for initiation of aerodynamic instabilities which are a critical element of the gas interaction theory. For the high-speed jet, these instabilities could be amplified so fast that atomization occurs in the region very near the exit plane as is observed in experiments under these conditions. Since the amount of swelling is dependent on the thickness of the boundary layer at the orifice exit, we can affect the breakup characteristics of the jet by varying this parameter. For example, if we wish the jet to remain intact, we can design an orifice passage to minimize the thickness of the boundary layer at its exit. These principles are used in the design of orifices for water-jet cutters and fire hoses. On the other hand, if we desire improved atomization (such as in many combustion applications), we simply evaluate designs which promote thick boundary layers at the orifice exit plane.

These findings will help guide the historically empirical orifice design process for combustion devices. By correlating performance of current injectors with the swelling parameter described above, we will be able to tailor future designs to meet requirements without the need of extensive (and expensive) development testing. Finally, the capability to predict atomization performance will lead to designs with increased efficiency, thereby not only reducing product cost, but increasing its capabilities at the same time. Appendix A provides a complete description of the model and the results of numerous simulations.

3.2 Simulation of F-1 Engine Tangential-Mode Instability

In our final report from the previous contract, we provided some findings on the stability of various F-1 injector designs used in the engine development program. Here, 2-D BEM simulations were conducted in which a fuel jet is exposed to transverse acoustic waves presumed to be present in the chamber. Both stable and unstable injector designs from the F-1 engine test program have been investigated. As one might expect, the response of the column grows dramatically when the acoustic frequency (ω_g) is near that of the column natural frequency (ω). Table 1 summarizes critical data for several F-1 injector designs.

Using the model, a simulation was conducted of a highly-unstable F-1 injector configuration (the Double Row Cluster, DRC), as well as the final, stable configuration demonstrated in Flight Rating Tests (FRT).

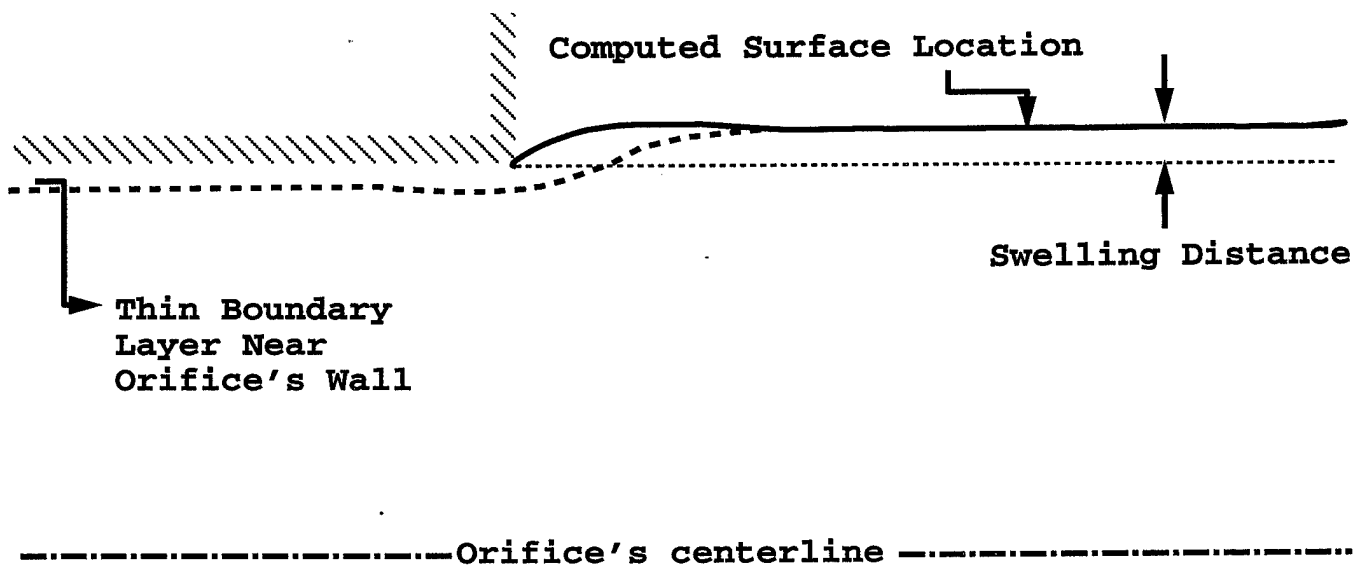


Figure 1: Results of computer simulations (which neglect the presence of the gas phase) indicate a steady, non-atomizing jet profile. The jet expands, or "swells" a small amount near the orifice exit plane.

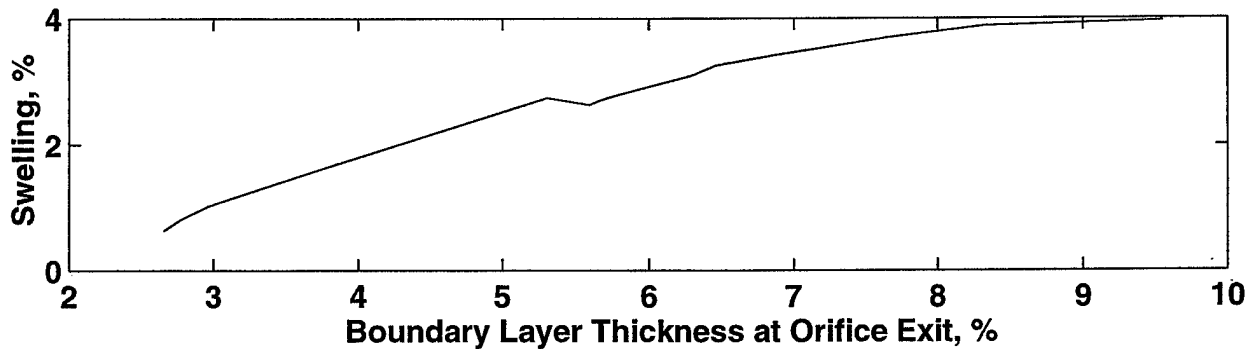


Figure 2: Swelling has been found to be a function of the boundary layer thickness at the orifice exit plane. Here, both axes are plotted as a percentage of the orifice radius.

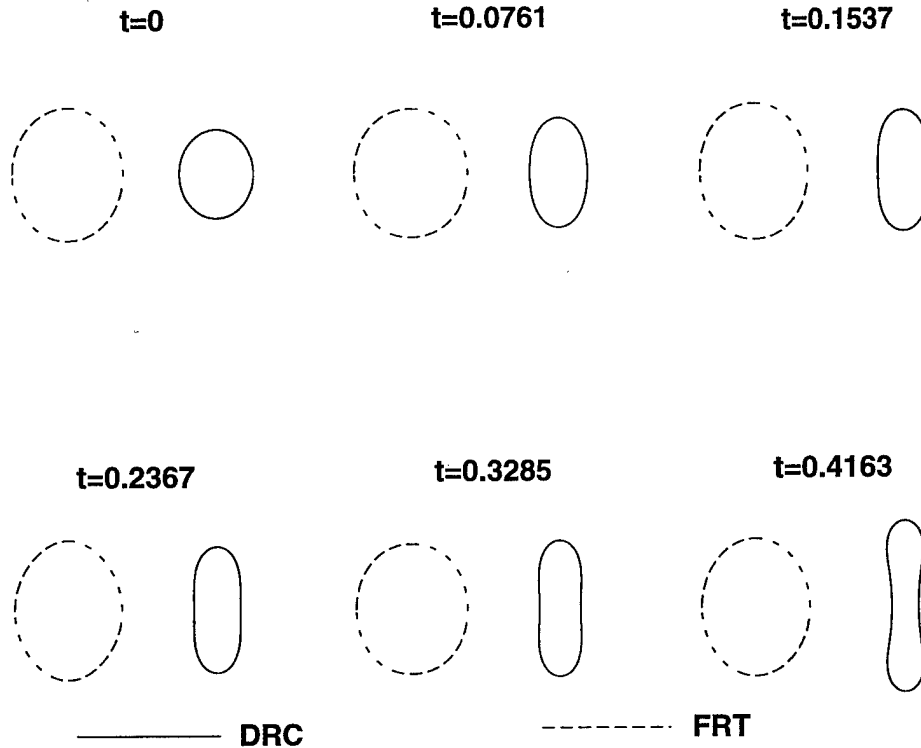


Figure 3: Simulation of Fuel-Jet Response in the Unstable Double-Row Cluster (DRC) and Stable Flight Rating Tests (FRT) F-1 Engine Injectors (times are measured in seconds from start of disturbance)

The DRC design exhibited a 1T instability at 454 Hz which led to chamber pressure oscillations of the order of 400% of the mean. The most prominent difference between these two injectors is the fuel orifice size (3.57 mm radius on FRT vs. 1.4 mm radius on DRC). The combination of the acoustic frequency in the chamber and the natural frequency of the DRC fuel column leads to conditions very near the resonant frequency. In fact, we calculate that $\omega_g/\omega = 1.7$ for the DRC, while the FRT design has $\omega_g/\omega = 7.0$, a value far from the high response region.

To assess the impact of the fuel orifice design differences between the two injectors, we have completed a simulation for both designs at a fixed Weber number of 0.1. Results of the column shapes at various times are shown in Fig. 3 for both designs. This figure shows that the unstable DRC design undergoes violent oscillations, whereas the stable FRT design is relatively unaffected by the imposed oscillation. Clearly, the large deformations of the DRC design will have substantial effect on the jet impingement region - a critical design feature for this impinging element injector. For this reason, **we believe that the sensitivity of the DRC design to transverse acoustic energy may be a major contributor to the instability of this injector design.**

Figure 4 provides results for this simple correlation for the five injector designs highlighted in Table 1. Here, results indicate stability if the frequency ratio exceeds a value of about 3; beyond this value, the column frequency is too low to generate appreciable response from the imposed external perturbation. We feel that these results point to an important new injector design criteria; the stability of injector fluid columns should be assessed with regard to coupling of the column harmonic frequencies and the acoustic modes of the chamber.

Further description of this analysis can be found in the *Journal of Propulsion and Power* article attached as Appendix B.

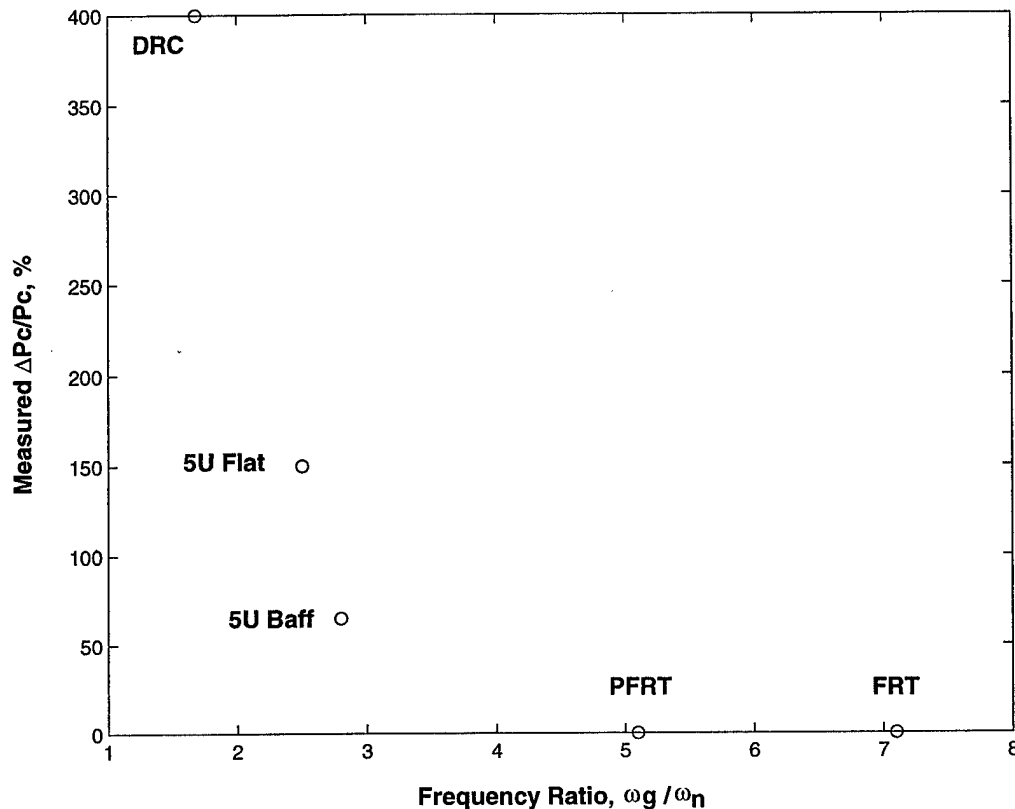


Figure 4: Correlation of F-1 Engine Response with Frequency Ratio, ω_g/ω_n .

3.3 Hybrid Rocket Injection Experimental Research

While the main focus of the studies in this project is analytic/numerical, a limited amount of experimental work was accomplished with funding from this contract (as obtained through AFRL at Edwards AFB). In particular, stable, reproduceable ignition was verified in a hybrid rocket using hydrogen peroxide as oxidizer and polyethylene as fuel. The engine made use of a unique Consumable Catalytic Bed (CCB) ignition system as highlighted in Fig. 5. The CCB permits rapid, reproduceable ignition events with a minimum cost and system complexity; engines were literally “slam started” with no special ignition valve opening procedure. A patent application is in process for the CCB design.

To investigate the functionality of the CCB, a transparent (Plexiglas) chamber was manufactured. Figure 6 provides a sequence of photographs of an actual test, showing the consumption of the device and its overall effect on the flowfield. Small perturbations in the pressure trace during some of the tests are attributed to ejection of small portions of CCB during the end stages of consumption. Overall, this injection/ignition concept is very attractive for hybrid engines not requiring a restart capability. Further details regarding this project are summarized in the manuscript in Appendix C.

3.4 Development of a 3-D BEM Code

A substantial new development resulting from this research involves the creation of a full three dimensional computational tool. The model employs linear elements and has undergone extensive validation on both droplet and liquid jet problems. Sample liquid jet grids are shown in Fig. 9 for various node densities. The code was run on a classic “infinite jet” simulation in order to assess performance against analytic results. Figure 10 summarizes the results of the calculations; the growth rate (surface deformation rate) is compared against the analytic result for a variety of wavenumbers, k . At low wavenumbers, excellent agreement is obtained. However, the results at high wavenumbers are not as accurate due to the fact that

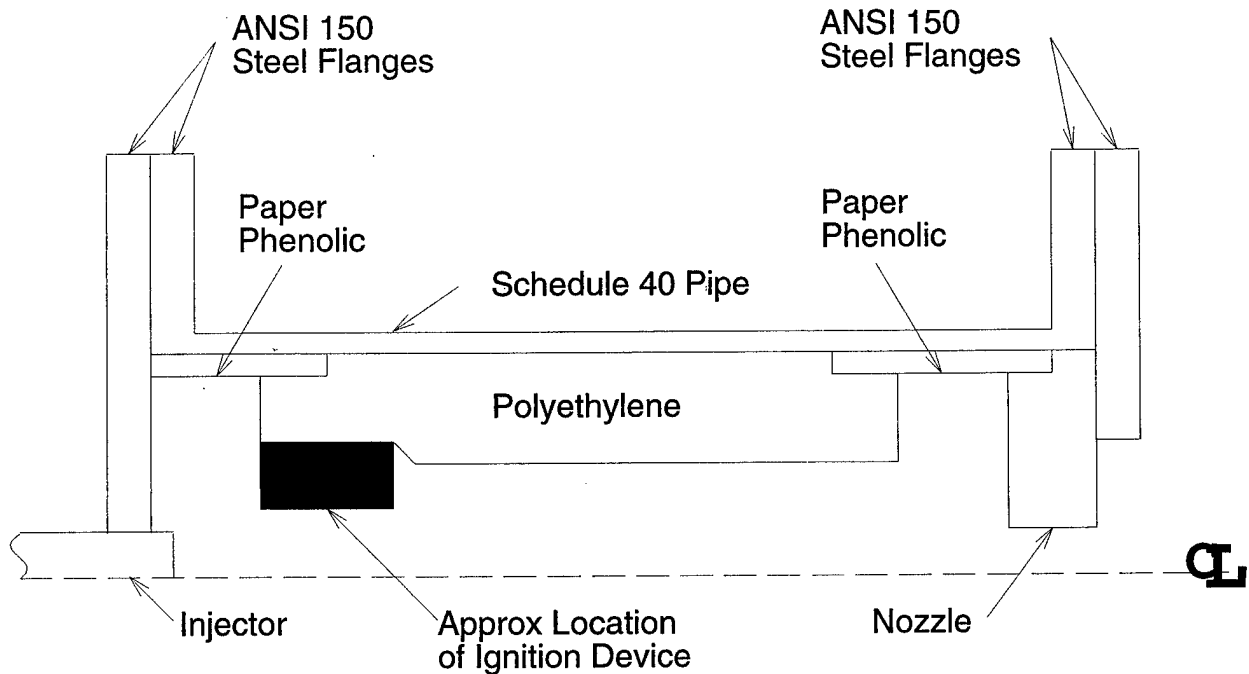


Figure 5: Cross Sectional View of the Combustion Chamber

the computational meshes employed are not sufficient to resolve the surface shape to the desired accuracy. These computations turned out to be very expensive; a single simulation here could take as long as one week on a state-of-the-art computer. More work needs to be performed to speed up the code through the use of parallelization and advanced matrix inversion schemes.

Another issue which warrants discussion is the surface treatment. Originally, we had arranged with Professor Chandrajit Bajaj, a leader in scientific visualization with a large research group in Computer Science, to provide surface remeshing capabilities for our simulations. Unfortunately, Dr. Bajaj left Purdue for a position at the University of Texas in early 1998. Prior to his departure, his students were having great difficulty adapting their current remeshing schemes to our problems since we typically demand much higher accuracy than that of a simple 3-D visualization of some object. For this reason, the present model does not contain a remeshing capability; a factor which negates the use of the code for highly nonlinear calculations. In these cases, mesh distortion due to surface motion makes regridding a necessity. This area is one of current research; we will continue to explore mechanisms to move the surface in a more accurate and effective fashion.

Appendix D provides additional documentation regarding the 3-D model development and validation.

3.5 Development of a Dense Spray Model

The last task initiated in the three-year research program involved the early stages of development of a dense spray model. Here, our motivation is to provide a tool for analysis of very complicated atomization problems (such as those in liquid rocket engines) in which $10^5 - 10^6$ droplets may be present. A unique "quasi-axisymmetric" methodology has been developed in which we analyze the spray produced along a single plane intercepting the axis of the jet/atomizer. Droplets are launched from the inner core of the jet and are permitted to collide and undergo secondary atomization. Droplet collision and secondary atomization modules draw from previous AFOSR research on these fundamental processes. For example, we utilize results from Professor Faeth's drop atomization work at Michigan and from Professor Law's drop collision work at Princeton - both projects were supported by AFOSR funding.

These droplet collision/atomization modules permit the tracking of roughly 100,000 droplets in a mas-

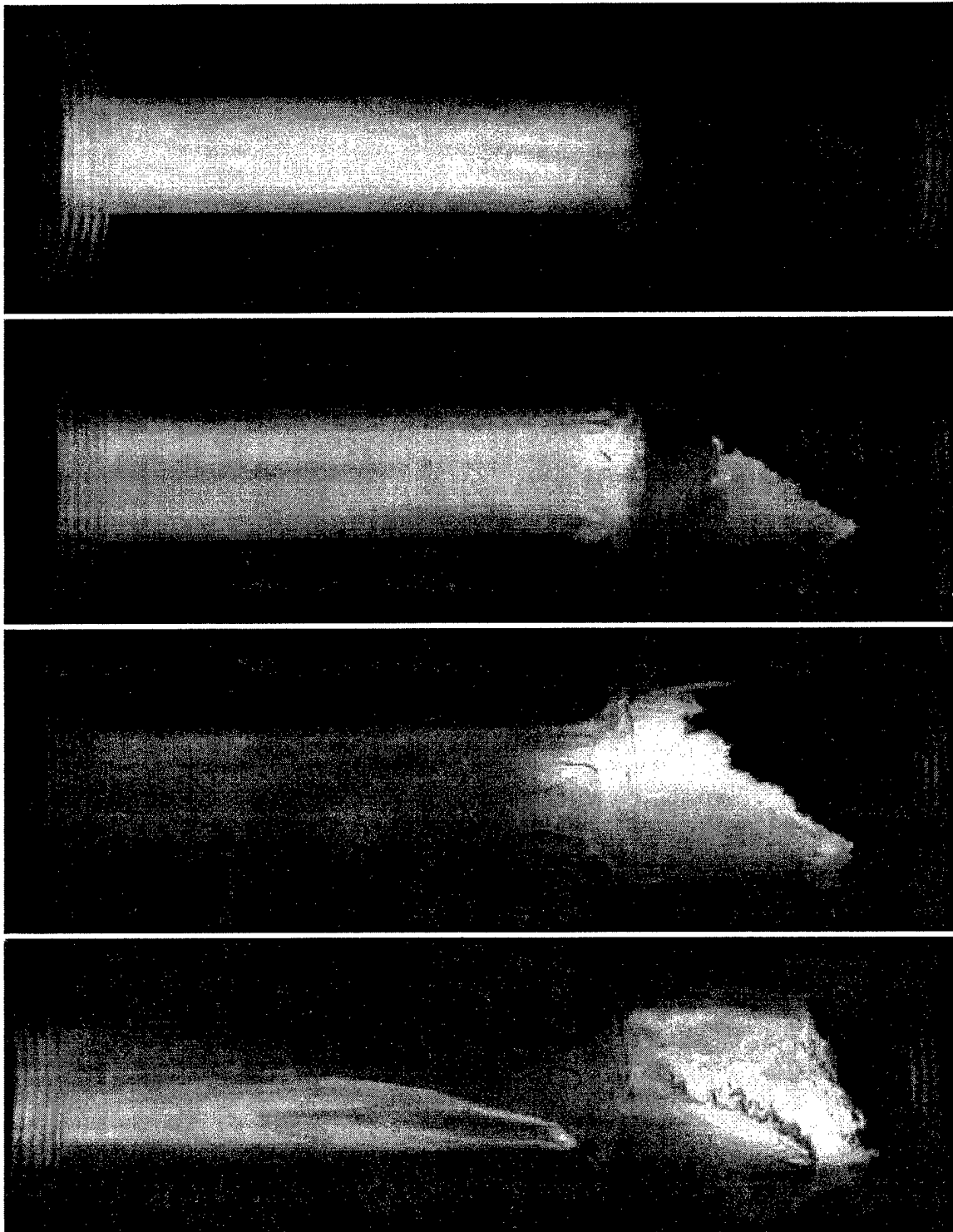


Figure 6: Still Photographs of Motor Y1 showing CCB consumption. Here, the CCB is located on the right hand side of the image and flow is from right to left. From top to bottom, images are for $t = 3.3$, 5.45 , 5.5 , and 11.5 sec

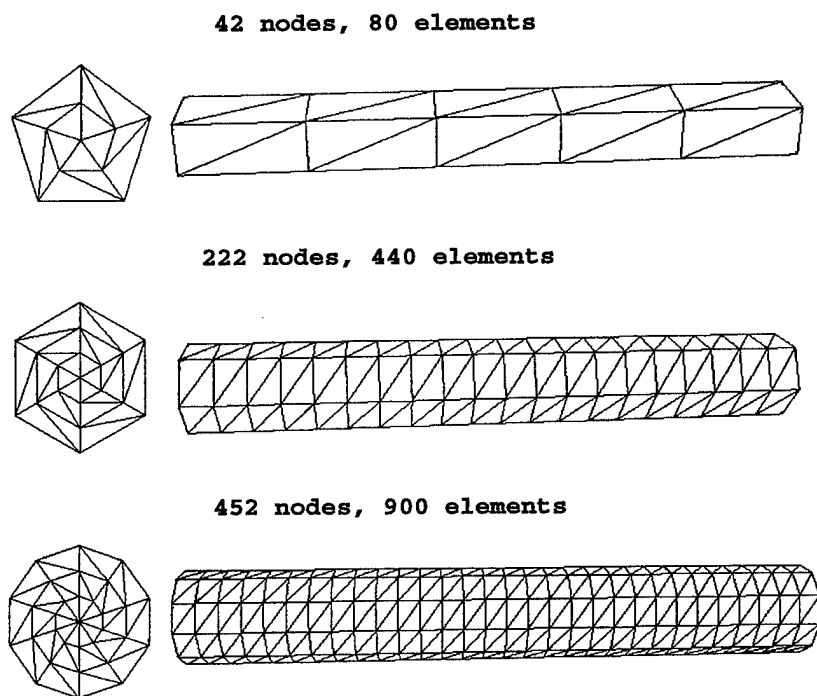


Figure 7: Sample Grids Utilized in 3-D BEM Liquid Jet Simulations

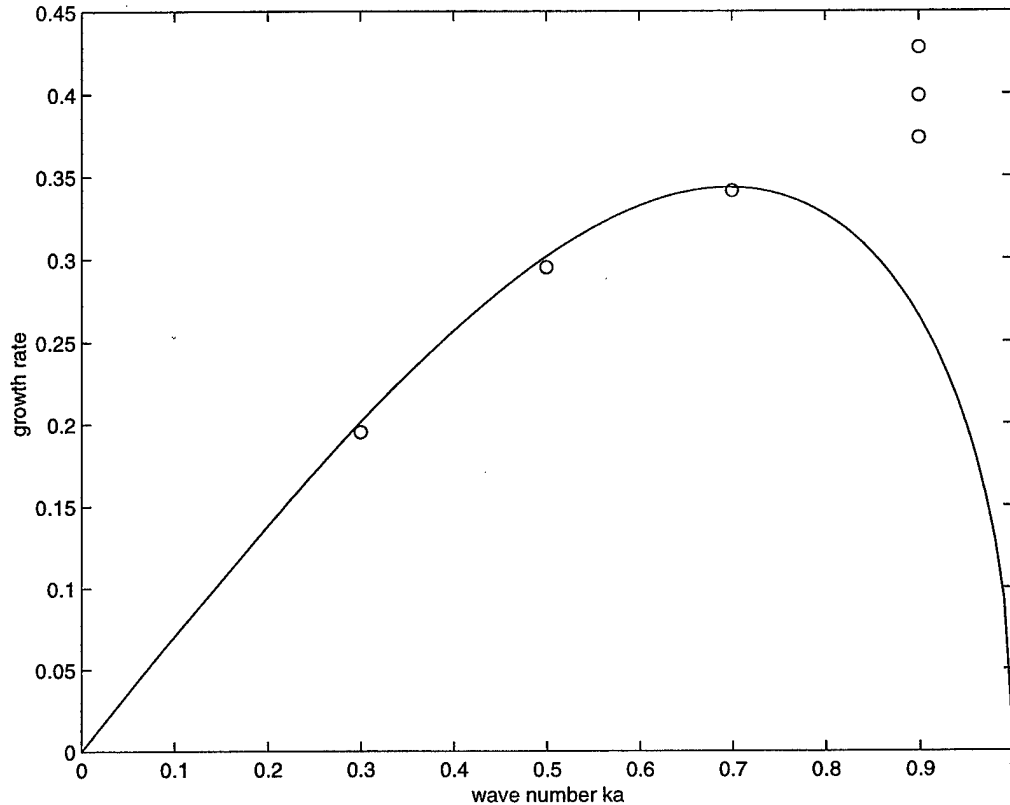


Figure 8: Validation of 3-D BEM on Linear Growth Rates (ω) of a Liquid Jet

sively parallel calculation. The coupling of the flowfield with the gas-phase behavior is accomplished by a parallel unsteady Navier-Stokes calculation which presumes the two-phase flow can be represented by a pseudo-fluid which varies in density between the liquid and gas extremes. We have had substantial success using a pseudo-fluid implementation to simulate complex cavitating flows in which large numbers of bubbles are present. For this reason, the methodology is also attractive for sprays in which large numbers of droplets are present.

The model, which is the subject of a follow-on grant by AFOSR and Dr. Mitat Birkan, is in the final stages of validation. In the coming year, we should have the capability to perform complete simulations of a dense spray and actually generate spray statistics (such as mean diameter, mass fluxes, and velocity fields) for the entire spray. This development will provide a tool useful for *real* sprays of interest to both the liquid rocket and atomization communities. A more detailed description of the model is contained in Appendix E of this report.

4 Professional Activities

The efforts outlined in the previous section of this report were made possible by two grants from AFOSR. A single student, Mr. Chienchi Chao, was supported under the base grant. In addition, some funds were obtained from AFRL at Edwards AFB; these funds appeared as augmentations to the initial award for the present contract. These monies were used to support hybrid rocket injection studies and the Ph.D. student Dr. Eric Wernimont.

Ph.D. Dissertations

Hilbing, J. M., "Modeling Liquid Jet Atomization Processes," August, 1996.

Wernimont, E., "Experimental Study of Combustion in Hydrogen Peroxide Hybrid Rockets," August, 1997.

Chao, C., "Three-Dimensional Nonlinear Jet Atomization Model," December, 1998.

M.S. Theses

Rump, K., "Modeling the Effect of Unsteady Chamber Conditions on the Atomization Process," December, 1996.

Murray, I., "Modeling Acoustically Induced Oscillations of Droplets," August, 1996. (A paper involving this work was awarded First Place in the AIAA Graduate Student Conference held in April, 1996 at Purdue University.)

A list of journal publications (and submissions) associated with these efforts are provided in the following list. Highlighted items (*) have been attached in the Appendices of this report.

Refereed Journal Publications and Submissions

1. Heister, S. D., Rutz, M., and Hilbing, J., "Effect of Acoustic Perturbations on Liquid Jet Atomization", *Journal of Propulsion and Power*, V13, No. 1, pp. 82-88, 1997.
2. Heister, S. D., "Boundary Element Methods for Two-Fluid Free Surface Flows", V19, No. 4, *Engineering Analysis with Boundary Elements*, pp. 309-317, 1997.
3. *Hilbing, J. H., and Heister, S.D., "Nonlinear Simulation of a High-Speed, Viscous, Liquid Jet", *Atomization and Sprays*, V 8, pp. 155-178, 1997.
4. Rump, K. M., and Heister, S. D., "Modeling the Effect of Unsteady Chamber Conditions on Atomization Processes", *Journal of Propulsion and Power*, V 14, pp. 576-578, 1998.
5. Murray, I. F., and Heister, S. D., "On a Droplet's Response to Acoustic Excitation", *International Journal of Multiphase Flow*, To Appear, 1999.
6. Wernimont, E.J., and Heister, S.D., "A Reconstruction Technique for Reducing Hybrid Rocket Combustion Test Data", *Journal of Propulsion and Power*, To Appear, 1999.
7. *Chao, C. and Heister, S. D., "Contributions of Atomization to F-1 Engine Combustion Instabilities", *Journal of Propulsion and Power*, In Review, 1997.
8. *Wernimont, E.J., and Heister, S.D., "Combustion Experiments in a Hydrogen Peroxide Polyethylene Hybrid Rocket with Catalytic Ignition", In Review, *Journal of Propulsion and Power*, 1998.

A list of the conference papers presented in association with work under these grants is provided in the list below. The starred item is included in Appendix E of this report.

Conference Papers and Presentations

1. Hilbing, J.H., Heister,, S.D., and Rump, K., "Recent Advances in Nonlinear Modeling of Atomization Processes", ILASS-96 Conference Proceedings, 1996.
2. Murray, I. F., and Heister,, S.D., "Modeling Acoustically-Induced Oscillations of Droplets", ILASS-96 Conference Proceedings, 1996.
3. Wernimont, E. J., and Heister, S. D., "Progress in Hydrogen Peroxide Oxidized Hybrid Rocket Experiments", AIAA 96-2696, 32nd AIAA Joint Propulsion Conference, 1996.

4. Rump, K. M., and Heister, S. D., "Modeling the Effect of Unsteady Chamber Conditions on Atomization Processes", AIAA 97-3298, 33rd AIAA Joint Propulsion Conference, 1997.
5. Heister, S. D., "Modeling Atomization Processes", 52nd Annual Industrial Waste Conference Proceedings, 1997.
6. *Heister, S. D., "Modeling Primary Atomization Processes", AIAA 98-3837, 34th AIAA Joint Propulsion Conference, 1998.
7. Heister, S. D., Wernimont, E. J., and Rusek, J. J., "High Test Peroxide Hybrid Rocket Research", Hydrogen Peroxide Propulsion Workshop, Surrey England, July, 1998. (see also: [http :
//www.ee.surrey.ac.uk/EE/CSER/UOSAT/conf/sheister.htm](http://www.ee.surrey.ac.uk/EE/CSER/UOSAT/conf/sheister.htm))

4.1 Technology Transfer/Coupling Activities

Numerous technology transfers have occurred during the period associated with these grants. These items are summarized the the table provided above. Models currently under development should be of great interest to the liquid and hybrid rocket engine community.

TECHNOLOGY TRANSFER

	Performer	Customer	Result	Application
1	S. D. Heister Purdue University Ph: (317) 494-5126	KB Sciences R. Humble Ph: (719) 333-6554	Provided Injector Designs	KEW Engines using Non-Toxic Propellants
2	S. D. Heister Purdue University Ph: (317) 494-5126	Allied Signal B. Marriot Ph: (219) 254-5235	Ramjet Inlet & Combustor Analysis	Talos Missile Target Drone
3	S.D. Heister Purdue University Ph: (317) 494-5126	TRW Space Group J. Calvinac Ph: (310) 812-5314	Pintle Injector Design	Shuttle Non-Toxic LOX/Ethanol Thruster
4	S.D. Heister Purdue University Ph: (317) 494-5126	TRW Space Group R. Sackheim Ph: (310) 813-9304	Pintle Injectors	Combustion Instability Studies
5	S. D. Heister Purdue University Ph: (317) 494-5126	KB Sciences R. Humble Ph: (719) 333-6554	Designed Injector	LLNL GOX/GH2 Water Rocket Concept

5 Appendix A - Viscous Jet Simulations

Hilbing, J. H., and Heister, S.D., "Nonlinear Simulation of a High-Speed, Viscous, Liquid Jet", *Atomization and Sprays*, V 8, pp. 155-178, 1997.

NONLINEAR SIMULATION OF A HIGH-SPEED, VISCOUS LIQUID JET

J. H. Hilbing* and S. D. Heister†

* Staff Engineer, TRW Space & Electronics Group, Redondo Beach, CA 90278

† Associate Professor, School of Aeronautics and Astronautics, Purdue University, W. Lafayette, IN 47907

Abstract

A model has been developed to simulate the nonlinear, unsteady evolution of a high-speed viscous liquid jet issuing from a circular orifice. The model is based on a zonal approach in which an integral method is utilized for a thin viscous region at the jet periphery, while a boundary element method is used for the inviscid "core" flow. Results indicate that steady-state solutions are possible neglecting the presence of the gas. Under these conditions, the jet "swells" in diameter and the boundary layer thins to a shear layer over a length of about half an orifice radius. Because boundary layer relaxation is occurring during these simulations in which steady-state solutions appear, atomization mechanisms relying on this process cannot explain the observed behavior. The swelling phenomenon has the potential to explain several fundamental experimental atomization observations regarding turbulence and orifice design.

Introduction

In many applications (combustors, paint, cosmetic, and agricultural sprays to name a few), it is highly desirable to inject a liquid in such a fashion that rapid atomization takes place. In spite of the high interest in spray-producing injectors, the design of these devices is largely empirical due to a lack of knowledge of the basic atomization mechanisms. Understanding of these mechanisms is incomplete because of difficulties in making experimental observations very near the nozzle and in modeling the often turbulent, two-phase flow in this region.

At the present time, several mechanisms have been suggested to contribute (or explain) the atomization process. Aerodynamic interactions are of obvious importance in generating Kelvin-Helmholtz type instabilities and in causing secondary atomization of larger drops shed from the periphery of the jet. Theory for this mechanism is due to G.I. Taylor¹, with more recent extensions and modifications². Unfortunately, this mechanism cannot explain all atomization behavior. Several researchers^{3,4} have shown that the design of the orifice passage definitely contributes to atomization behavior in many instances. Additionally, cavitation^{5,6} in the orifice also can play an important role in some cases.

Many researchers have proposed that the state of the boundary layer exiting the orifice is a critical atomization mechanism. For example, some have suggested that boundary layer turbulence plays a critical role in the atomization process. While turbulence may play a role in destabilizing low-speed jets^{7,8}, at the higher speeds consistent with the atomization regime, results indicate^{3,9} that nozzles with turbulent boundary layers provided poorer atomization (as evidenced by a smaller cone angle) than laminar jets. In addition, theoretical work^{10,11} suggests that turbulent velocity profiles are actually more stable than the more fully-developed profiles associated with laminar flows.

Other authors^{12,13} have suggested that boundary layer velocity profile rearrangement (due to the change from a no-slip to a free surface condition at the orifice exit) can explain atomization behavior. While there is some doubt that this mechanism can fully explain atomization³, this factor has not been eliminated as a potential contributor at this point in time.

Recent development of fully-nonlinear models based on boundary element methods¹⁴⁻¹⁶ have enhanced abilities to simulate complex atomization processes under the assumption of inviscid flow. Most recently, models have been created¹⁶⁻¹⁸ to include the effects of orifice geometry on the atomization process. The present work provides an extension to these previous models via the incorporation of a viscous region at the periphery of the jet (as well as inside the orifice passage). The model is applied over a range of Reynolds and Weber numbers to shed light on the role of boundary layer development on the atomization process.

Model Development

At the present time, there are very few analytic/numerical tools available to provide high-resolution, nonlinear simulations of liquid jets in the atomization regime. This regime is typically characterized by thin boundary layers (typically less than 10% of the orifice radius) and high Reynolds numbers (of the order of 10^4 - 10^5). While the fully-viscous treatments of Unverdi and Tryggvason¹⁹ and Osher and Sethian²⁰ have demonstrated abilities to provide high-resolution simulations of capillary flows, these methods are currently limited (due to computational resources) to Reynolds numbers of the order of 10^2 .

Boundary element methods (BEMs) are quite attractive for inviscid problems, however the nonlinearity of the governing equations for viscous flow present substantial complications for this modeling technique. Recent development of the Dual Reciprocity Method²¹ has extended BEM capabilities to viscous flows, but this technique also has trouble in providing adequate resolution for high Reynolds number problems¹⁷.

For this reason, it appears that a zonal approach which provides a separate treatment for the viscous region would be attractive. Such techniques have been supplied successfully by Wu^{22,23} by solving a set of boundary layer equations (by standard CFD methods) in viscous regions, and using BEM at the edge of the boundary layer. In free surface problems with moving grids, application of a full CFD grid to the boundary layer would be a substantial expense in today's computing environment. For this reason, we have chosen an integral method to model the behavior of the viscous zone. Hailey, et. al.²⁴ had successfully adopted this technique to solve viscous external flows over solid boundaries. Using this approach in an axisymmetric unsteady calculation, the entire jet can be modeled with two lines of nodes: one at the gas/liquid or liquid/wall interface, and one at the edge of the liquid boundary layer.

We presume that all variables have been nondimensionalized by choosing the liquid density, the orifice radius, and the ideal (Bernoulli) orifice exit velocity as dimensions. When compared with the well-known Karman-Pohlhausen technique, the present analysis is complicated due to unsteadiness in the boundary layer, and due to the fact that the boundary layer is axisymmetric (rather than two dimensional). This latter point is important, since the boundary layer will naturally tend to be reduced in thickness under outward radial motion due to conservation of mass considerations. The governing equations for the viscous region can be developed by assuming a polynomial approximation for the velocity profile, solving for the coefficients of the polynomial based on edge conditions, and finally substituting the assumed profile into the integral form of the momentum equation and completing the integrations. The following subsections outline this procedure for two cases: a boundary layer on a solid wall, and a boundary layer on a free surface.

Solid Wall Boundary Layer

The integral analysis derived herein provides an extension to the results derived by Howarth²⁵ for the case of a unsteady, axisymmetric flow over a solid boundary. Here, we have unique treatments due to the fact that we have an internal flow within the orifice passage, and because of the free-surface boundary condition applied outside the orifice. The boundary layer profile is assumed to be approximated by a fourth-order polynomial:

$$\frac{u}{u_e} = a_0 + a_1 \eta + a_2 \eta^2 + a_3 \eta^3 + a_4 \eta^4 \quad (1)$$

where u and u_e are velocities parallel to the wall within and at the edge of the boundary layer, respectively. The parameter $\eta = y/\delta$ varies from 0 at the wall to 1 at the edge of the inviscid core. The five coefficients ($a_0 - a_4$) are determined from the following boundary conditions²⁶:

$$\begin{aligned} u(0) &= \left(\frac{\partial u}{\partial y} \right)_{y=\delta} = \left(\frac{\partial^2 u}{\partial y^2} \right)_{y=\delta} = 0 \\ u(\delta) &= u_e \quad ; \quad \left(\frac{\partial^2 u}{\partial y^2} \right)_{y=0} = \text{Re} \left(\frac{\partial p}{\partial x} \right) \end{aligned} \quad (2)$$

The fifth condition in Equation 2 comes from examination of the x -momentum equation at the wall, using $u(0) = v(0) = 0$ and $\partial^2 u / \partial x^2 \ll \partial^2 u / \partial y^2$. Solving for the coefficients in Equation 1 using the given boundary conditions yields:

$$\frac{u}{u_e} = (2\eta - 2\eta^3 + \eta^4) + \frac{\Lambda}{6} (1 - \eta)^3 \eta \quad (3)$$

where

$$\Lambda = -\frac{\delta^2 \text{Re}}{u_e} \left(\frac{\partial p}{\partial x} \right) \quad (4)$$

is a pressure gradient parameter, and is derived from examination of the unsteady momentum equation at the outer edge of the boundary layer.

The governing integral momentum equation can be derived by considering an incremental width of the boundary layer at some radial location r_0 of the orifice wall, as shown in Figure 1. An x - y axis system is aligned with the orifice wall such that the y -axis extends into the fluid and makes an angle of ζ with a line in the radial direction. Note that $\zeta = 0$ for a simple, non-tapered orifice passage. A momentum balance in this annular section of the boundary layer follows the derivation given by Howarth²⁵, and for this unsteady, internal flow can be written:

$$\frac{\partial}{\partial x} (u_e^2 \theta) + u_e \left(\frac{\partial u_e}{\partial x} \right) \delta^* + \frac{u_e^2 \theta}{r_0} \left(\frac{dr_0}{dx} \right) + \int_0^\delta \bar{y} \left(\frac{\partial u_e}{\partial t} - \frac{\partial u}{\partial t} \right) dy = \frac{1}{\text{Re}} \left(\frac{\partial u}{\partial y} \right)_{y=0} \quad (5)$$

where

$$\bar{y} = r_0 - y \cos \zeta \quad (6)$$

δ^* is the displacement thickness, and θ the momentum thickness, defined as:

$$\delta^* = \int_0^\delta \left(1 - \frac{y}{r_0} \cos \zeta \right) \left(1 - \frac{u}{u_e} \right) dy \quad (7)$$

and

$$\theta = \int_0^\delta \left(1 - \frac{y}{r_0} \cos \zeta \right) \left(1 - \frac{u}{u_e} \right) \left(\frac{u}{u_e} \right) dy \quad (8)$$

respectively. Substituting the assumed profile from Equation 3 into Equations 7 and 8 results in integrals which can be evaluated analytically. Performing these integrations gives:

$$\delta^* = \delta \left[\frac{3}{10} - \frac{\Lambda}{120} + \frac{\delta}{r_0} \cos \zeta \left(\frac{\Lambda}{360} - \frac{1}{15} \right) \right] \quad (9)$$

for the displacement thickness, and:

$$\theta = \delta \left[\frac{37}{315} + \frac{\Lambda}{945} - \frac{\Lambda^2}{9072} - \frac{\delta}{r_0} \cos \zeta \left(\frac{5}{126} - \frac{\Lambda}{945} - \frac{\Lambda^2}{30240} \right) \right] \quad (10)$$

for the momentum thickness.

Equations 9 and 10 can be substituted into Equation 5 to give a single equation involving δ , δ^2 , $(\partial\delta/\partial x)$, and $\delta(\partial\delta/\partial x)$. The remaining quantities in the equation (Λ , Λ^2 , ζ , etc.) are known along the boundary layer interface since we presume that $\partial p/\partial x = -u_e (\partial u_e/\partial x)$ in accordance with standard boundary layer assumptions. The momentum equation can be solved by utilizing a first-order backwards difference to approximate the derivative of the boundary layer thickness at node i :

$$\left(\frac{\partial \delta}{\partial x} \right)_i \approx \frac{\delta_i - \delta_{i-1}}{\Delta x} \quad (11)$$

Assuming that the δ and δ^2 quantities in the equation are evaluated at node i , the equation reduces to a cubic equation for the boundary layer thickness:

$$c_3 \delta_i^3 + c_2 \delta_i^2 + c_1 \delta_i + c_0 = 0 \quad (12)$$

which can be solved for δ_i . Since δ_{i-1} is assumed known and is included in the c_i coefficients in Equation 12, this equation can be solved by marching along the boundary layer using an initial value of the boundary layer thickness at the first node. This differencing and solution procedure is consistent with the parabolic nature of the boundary layer equations. The c_i values are quite complicated functions whose definitions are included in the Appendix.

Free Surface Boundary Layer

Equation 1 is again assumed to approximate the boundary layer profile along the free surface of the jet. Here, the boundary conditions are chosen as:

$$\begin{aligned} u(0) &= u_s \quad ; \quad u(\delta) = u_e \\ \left(\frac{\partial u}{\partial y}\right)_{y=0} &= \left(\frac{\partial u}{\partial y}\right)_{y=\delta} = \left(\frac{\partial^2 u}{\partial y^2}\right)_{y=\delta} = 0 \end{aligned} \quad (13)$$

so that their substitution yields the boundary layer profile:

$$\frac{u}{u_e} = \left(1 - \frac{u_s}{u_e}\right) (6\eta^2 - 8\eta^3 + 3\eta^4) + \frac{u_s}{u_e} \quad (14)$$

where u_s is the velocity at the surface of the jet.

Figure 1 shows the nomenclature for the boundary layer along the free surface of the jet. As in the case of the solid wall, the integral momentum equation is derived by applying conservation of momentum to the annular region containing the boundary layer. This equation can be written in general form as:

$$\hat{e}_x \cdot \left\{ \frac{d}{dt} \left[\int_V \bar{u} \, dm \right] + \int_S \bar{u} \, d\dot{m} = \int_S \sigma_{ij} n_i \, dA \right\} \quad (15)$$

where V and S denote the volume and surface area of the annular section, respectively, \hat{e}_x denotes the tangential unit vector, $dm = \rho \, dV$, and $d\dot{m} = \rho(\bar{u} - \bar{u}_s)\hat{n} \, dA$. Here, σ_{ij} is the stress tensor, defined as:

$$\sigma_{ij} = -p\delta_{ij} + \mu \left(\frac{\partial u_i}{\partial x_j} + \frac{\partial u_j}{\partial x_i} \right) \quad (16)$$

with δ_{ij} , the Kronecker delta. Carrying out the dot product, the first term can be written:

$$\hat{e}_x \cdot \left\{ \frac{d}{dt} \left[\int_V \bar{u} \, dm \right] \right\} = \frac{d}{dt} \left[\hat{e}_x \cdot \int_V \bar{u} \, dm \right] - \frac{d\hat{e}_x}{dt} \cdot \left[\int_V \bar{u} \, dm \right] \quad (17)$$

which can be further simplified to:

$$\hat{e}_x \cdot \left\{ \frac{d}{dt} \left[\int_V \bar{u} \, dm \right] \right\} = \frac{d}{dt} \left[\int_V u \, dm \right] - \left(\frac{d\hat{e}_x}{dt} \right)_y \int_V v \, dm \quad (18)$$

Note that $d\hat{e}_x/dt$ is nonzero during free surface motion, but only has a component in the direction normal to the surface, denoted with a subscript y in the equation. In evaluating the right hand side of Equation 15, second derivatives of the x -velocity are neglected in accordance with standard boundary layer theory²⁶. However, the x -derivatives of the y -velocity are retained. Using these assumptions, and Equation 18, the momentum equation in integral form becomes^{18,25}:

$$\begin{aligned} & \frac{d}{dt} \left[\int_0^\delta \bar{y} u \, dy \right] + \left(\frac{d\hat{e}_x}{dt} \right)_y \int_0^\delta \bar{y} v \, dy + \\ & (r_0 - \delta \cos \zeta) u_e \left(\frac{\partial \phi}{\partial y} + q_s \right) + \frac{\partial}{\partial x} \left[\int_0^\delta \bar{y} u (u - u_s) \, dy \right] = \\ & \frac{1}{\text{Re}} \left[(r_0 - \delta \cos \zeta) \left(\frac{\partial v}{\partial x} \right)_{y=\delta} - r_0 \left(\frac{\partial v}{\partial x} \right)_{y=0} \right] - \frac{\partial p}{\partial x} \int_0^\delta \bar{y} \, dy \end{aligned} \quad (19)$$

where \bar{y} is defined as:

$$\bar{y} = r_0 - y \cos \zeta \quad (20)$$

Here, evaluation of volume integrations leads to terms involving conditions at the boundary shared with the inviscid (potential) core. For example, the term involving $\partial\phi/\partial y$ represents the velocity normal to the inner edge of the boundary layer shown in Fig. 1. The quantity ϕ represents the velocity potential in the inviscid core region. If the assumed boundary layer profile in Equation 14 is substituted into Equation 19,

the integrals can be evaluated, and the result is an equation involving δ , $(\partial\delta/\partial x)$, $\delta(\partial\delta/\partial x)$, $(\partial\delta/\partial t)$ and $\delta(\partial\delta/\partial t)$. The remaining quantities are known along the entire surface. In the same manner used in the previous section, backwards differences can be used to approximate $(\partial\delta/\partial x)$ and $(\partial\delta/\partial t)$:

$$\left(\frac{\partial\delta}{\partial x}\right)_i^n \approx \frac{\delta_i^n - \delta_{i-1}^n}{\Delta x} \quad \left(\frac{\partial\delta}{\partial t}\right)_i^n \approx \frac{\delta_i^n - \delta_i^{n-1}}{\Delta t}$$

Substitution of these approximations into Equation 19 results in an equation of the form:

$$b_0 + b_1 \delta_i^n + b_2 (\delta_i^n)^2 = 0 \quad (21)$$

where the subscript i denotes the node, and the superscript n , the time level. Values of the boundary layer thickness at previous nodes and previous time levels are present in the known b_0 and b_1 coefficients of Equation 21, so a time and space marching method can be used to solve for the boundary layer thickness along the free surface. In the current method, δ is calculated starting at the orifice exit, and the boundary layer in the orifice must be calculated before that for the free surface. The Appendix contains the rather involved definitions of the b_i coefficients.

Surface Velocities and Flow Kinematics

Solution of Laplace's equation in the inviscid core results in components of the velocity vector $(\partial\phi/\partial s$ and $q)$ at the inner edge of the boundary layer¹⁶. Two additional conditions are required to determine the tangential and normal velocities at the free surface.

An examination of the x -momentum equation on the free surface yields an equation for the tangential velocity on the surface, u_s . In Lagrangian form, the dot product of the vector momentum equation and tangential unit vector can be written:

$$\hat{e}_x \cdot \left(\frac{D\vec{u}}{Dt} = -\nabla p + \frac{1}{\text{Re}} \nabla^2 \vec{u} \right) \quad (22)$$

Carrying out the dot product produces another term involving the time derivative of the tangential unit vector:

$$\frac{Du_s}{Dt} - \vec{u} \cdot \frac{D\hat{e}_x}{Dt} = -\frac{\partial p}{\partial x} + \frac{1}{\text{Re}} \nabla^2 u_s \quad (23)$$

Since only the normal component of this change in the tangential unit vector is non-zero, Equation 23 reduces to:

$$\frac{Du_s}{Dt} = q_s \left(\frac{D\hat{e}_x}{Dt} \right)_y - \frac{\partial p}{\partial x} + \frac{1}{\text{Re}} \left(\frac{\partial^2 u_s}{\partial x^2} + \frac{\partial^2 u_s}{\partial y^2} \right) \quad (24)$$

Again, $(\partial^2 u_s / \partial x^2)$ is neglected in the boundary layer, and substitution of the boundary layer profile permits evaluation of the remaining second derivative:

$$\frac{Du_s}{Dt} = q_s \left(\frac{D\hat{e}_x}{Dt} \right)_y - \frac{\partial p}{\partial x} + \frac{12\delta^2 (u_e - u_s)}{\text{Re}} \quad (25)$$

Equation 25 is integrated in time to solve for the change in tangential velocity along the free surface.

The normal velocity at the surface can be derived by examination of the integral continuity equation in the annular section shown in Figure 1. This equation can be solved for q_s to yield:

$$q_s = - \left(1 - \frac{\delta}{r_0} \cos \zeta \right) \frac{\partial \phi}{\partial y} - \frac{1}{r_0} \frac{\partial}{\partial x} \left[\int_0^\delta \bar{y} u \, dy \right] \quad (26)$$

where $\partial\phi/\partial y$ is defined as positive in the direction into the fluid. Substituting the boundary layer profile into this equation, integrating to the boundary layer thickness, and differentiating the last term with respect to x , gives:

$$\begin{aligned} q_s = & - \left(1 - \frac{\delta}{r_0} \cos \zeta \right) \frac{\partial \phi}{\partial y} \\ & - \frac{1}{5} \left[\left(\frac{\delta}{r_0} \frac{\partial r_0}{\partial x} + \frac{\partial \delta}{\partial x} \right) (3u_e + 2u_s) + \delta \left(3 \frac{\partial u_e}{\partial x} + 2 \frac{\partial u_s}{\partial x} \right) \right] \\ & + \frac{\delta}{10} \left[\left(\frac{2 \cos \zeta}{r_0} \frac{\partial \delta}{\partial x} - \frac{\delta \sin \zeta}{r_0} \frac{\partial \zeta}{\partial x} \right) (4u_e + u_s) + \frac{\delta \cos \zeta}{r_0} \left(4 \frac{\partial u_e}{\partial x} + \frac{\partial u_s}{\partial x} \right) \right] \end{aligned} \quad (27)$$

For small δ , dilatation and rotation of the boundary layer due to changes in r_0 , u_e , and u_s is minor and the equation reduces to the straightforward result $q_s \approx -\partial\phi/\partial y$. Inside the orifice passage, the solid surface dictates that $q_s = 0$ in this region.

For the node at the tip of the jet (on the jet centerline), Eq. 27 becomes:

$$(q_s)_{r_0=0} = - \left(1 + \delta \frac{\partial\zeta}{\partial x} \right) \frac{\partial\phi}{\partial y} - \frac{\delta}{5} \left[6 \frac{\partial u_e}{\partial x} + 4 \frac{\partial u_s}{\partial x} + \delta \frac{\partial\zeta}{\partial x} \left(4 \frac{\partial u_e}{\partial x} + \frac{\partial u_s}{\partial x} \right) \right] \quad (28)$$

where we have used the basic geometric result:

$$\lim_{r_0 \rightarrow 0} \frac{\cos\zeta}{r_0} = -\frac{\partial\zeta}{\partial x} \quad (29)$$

in deriving this relation.

The surface is tracked along its instantaneous velocity vector in a manner similar to the method used in Hilbing, et. al.¹⁶ with axial and radial components of the surface velocity given by:

$$\frac{Dz_s}{Dt} = u_s \cos\zeta - q_s \sin\zeta \quad (30)$$

and

$$\frac{Dr_s}{Dt} = u_s \sin\zeta + q_s \cos\zeta \quad (31)$$

where z_s , r_s are coordinates of nodes lying on the interface. These equations are integrated with a 4-th order Runge-Kutta integration scheme to solve for the surface evolution in time. The boundary layer is tracked with respect to nodes on the jet surface, so that the location of the inviscid core region is given by:

$$\begin{aligned} z_c &= z_s + \delta \sin\zeta \\ r_c &= r_s - \delta \cos\zeta \end{aligned} \quad (32)$$

where (z_c, r_c) are the coordinates of the node at the edge of the boundary layer, and ζ is the local slope of the free surface of the jet. The unsteady Bernoulli equation requires a modification since the nodes at the edge of the inviscid core region are no longer moving with their instantaneous velocity. Neglecting gravity, Bernoulli's equation¹⁶ can be written as:

$$\frac{\partial\phi}{\partial t} = -\frac{1}{2}(\nabla\phi)^2 - \frac{\kappa}{We} \quad (33)$$

where ϕ is the velocity potential, κ is the surface curvature, and We is the Weber number as defined in the Nomenclature. Performing an Eulerian-Lagrangian transformation for nodes moving with the local *surface* velocity gives:

$$\frac{D\phi}{Dt} = -\frac{1}{2}(\nabla\phi)^2 + u_z \left(\frac{\partial\phi}{\partial z} \right) + u_r \left(\frac{\partial\phi}{\partial r} \right) - \frac{\kappa}{We} \quad (34)$$

where

$$\frac{\partial\phi}{\partial z} = \frac{\partial\phi}{\partial s} \cos\beta - q \sin\beta \quad (35)$$

and

$$\frac{\partial\phi}{\partial r} = \frac{\partial\phi}{\partial s} \sin\beta + q \cos\beta \quad (36)$$

with β the local slope of the boundary layer interface with respect to the centerline of the jet. In Equation 34, u_z and u_r are the nodal velocities on the free surface. They are calculated by the first-order forward differences:

$$u_z^{n+1} = \frac{z_c^{n+1} - z_c^n}{\Delta t} \quad (37)$$

and

$$u_r^{n+1} = \frac{r_c^{n+1} - r_c^n}{\Delta t} \quad (38)$$

where superscripts denote the time level. Surface curvature in Eq. 34 is calculated using fourth-order centered differences¹⁶.

Solution Procedure

We use the following procedure to solve for the evolution of a finite-length liquid jet and the subsequent development of the boundary layer inside the orifice and along the surface of the jet:

- Update the integrated quantities $u_s, z_s,$ and r_s on the jet surface and ϕ at the inner edge of the boundary layer using a Runge-Kutta integration scheme on Equations 25, 30, 31, and 34;
- At every node along the free surface, update quantities dependent on the surface geometry, including the slopes β and ζ , the curvature κ , the pressure along the free surface p , and the derivatives $\partial p/\partial x$, $\partial r_0/\partial x$ and $\partial \zeta/\partial x$;
- Solve for the inviscid flow in the core region using the BEM solver for Laplace's equation¹⁸. This procedure returns values of the velocity potential ϕ , and normal velocity q , at the boundary of the entire inviscid region;
- Calculate properties at the edge of the boundary layer, including the velocities $\partial \phi/\partial s$, u_e and $\partial \phi/\partial y$, the pressure gradient parameter Λ , and the derivatives $\partial q/\partial s$, $\partial u_e/\partial s$, $\partial u_s/\partial s$, $\partial v/\partial x$, $\partial q_s/\partial x$, $\partial p/\partial x$ and $\partial \Lambda/\partial x$;
- Solve for the boundary layer thickness inside the orifice using Equation 12 by marching from the orifice inlet using a specified value of δ at the inflow boundary;
- Solve for the boundary layer thickness along the free surface of the jet using Equation 21 by marching from the orifice exit to the jet tip;
- Calculate $\partial \delta/\partial x$ with a 5-point difference scheme on the calculated values of δ ;
- Solve for the surface normal velocity using Equation 27; and
- Update the location of the edge of the inviscid core region using Equation 32.

Initial Conditions

Since the transition from a no-slip to a free surface boundary condition is an important element of this model, the inflow boundary is placed at a specified distance into the nozzle. The computational domain is shown in Figure 2, with nodes at the interior edge of the boundary layer omitted for clarity. While this figure depicts a simple cylindrical orifice interior, arbitrary axisymmetric contours can be considered with the model. The boundary layer thickness at the entry to the domain (δ_0) is a required input for the analysis.

Since the choice of initial conditions essentially determines the nature of the results, starting the calculation is a key part of this model. A natural choice is to assume that the jet is at rest at $t = 0$, and turn on the inflow at $t = 0^+$ with some specified function. A problem with this method, however, is that if any fluid exists outside the orifice before the calculation begins, the fluid exiting the orifice tends to create a bulging on the jet surface just outside the orifice (klystron effect). Although the formation of surface waves just after the orifice is a desired result for this model, we are not interested in waves formed by the klystron effect, but rather in waves due to the presence of the boundary layer. If the jet begins with very little fluid outside the orifice, there may be a large computational cost involved in marching the solution to a "steady state," as well as problems in calculating the boundary layer thickness on the free surface of the jet.

The calculations performed in previous inviscid models¹⁶ began with a cylindrical length of fluid with a hemisphere endcap moving at a uniform axial velocity. If the viscous calculations start with similar initial conditions, the initial solution of the boundary layer thickness in the nozzle gives a step change in profile which leads to numerical instabilities in solving for the boundary layer thickness on the free surface. One way to alleviate this problem is to begin the calculation with $Re \approx \infty$ and $\delta = 0$ at the inflow boundary. After beginning the calculation, the Reynolds number is allowed to decrease to the desired value over some period of time, and the boundary layer thickness at the inflow, δ_0 , allowed to increase to the desired value over the same period.

Physically, this starting procedure amounts to a "ramping" of the viscosity from zero (inviscid case) up to the desired value over a finite startup interval. While surface waves are generated as a result of this starting transient, the waves are convected downstream such that the near-orifice behavior at $t \gg 0$ is independent

of the particular starting transient selected for the simulation. During the startup interval, defined as Δt_μ , δ_0 is assumed to vary linearly, and the Reynolds number is assumed to decrease according to the following function:

$$\log_{10} \text{Re} = \left(\frac{t - t_0}{\Delta t_\mu} \right) \log_{10} \text{Re}_1 + \left(\frac{t_1 - t}{\Delta t_\mu} \right) \log_{10} \text{Re}_0 \quad (39)$$

where $\Delta t_\mu = t_1 - t_0$, and Re_0 and Re_1 are the initial and final values of the Reynolds number, respectively. At time t_0 , the surface velocity in the nozzle transitions from $u_s = 1$ to $u_s = 0$ instantaneously, and the initial Reynolds number is chosen as $\text{Re}_0 = 10^{12}$.

Results

A series of calculations were performed to insure that the near-orifice exit behavior was insensitive to the assumed initial start transient at times much greater than the start-up interval. Therefore, the viscosity-ramping technique was employed for all results presented here. In addition, a series of simulations were conducted to verify that results were insensitive to both temporal and spatial discretization step sizes. A typical calculation presumes a nozzle internal length of 1 jet radius, an initial jet length of 4 radii, and uses a time step of $\Delta t = 0.002$. Algebraic stretching¹⁶ is used to place the 15 nodes in the nozzle with points concentrated more heavily near the orifice exit plane. The grid spacing on the jet is $\Delta s = 0.05$ after the orifice for 2 jet radii, and then transitions to $\Delta s = 0.10$. Grid function convergence studies have been conducted to insure that results are insensitive to both temporal and spatial step sizes thereby demonstrating that solutions are independent of these parameters. Algebraic stretching and two different grid spacings are used as a method of reducing the total number of nodes and therefore the computational time. Typical run times were on the order of a few days on an IBM RISC/System 6000 machine.

Figure 3 depicts the typical free-surface evolution in the region near the orifice exit during and immediately after the start-up interval. Note that the vertical scale is amplified dramatically; wave slopes are quite small when plotted on a true scale. This calculation was performed with $\text{We} = 10^4$, $\text{Re} = 10^4$ and $\delta_0 = 0.05$. The viscosity is turned on at $t = 0.01$ time units, with a startup interval of $\Delta t_\mu = 2$ time units. As the viscosity is increased during the start transient, a surface wave is formed. This disturbance is convected downstream at the mean velocity of the jet. While the wave associated with the start transient grows with time and convects downstream, the surface near the orifice exit takes on a steady shape with a "swelling" in diameter as compared to that of the orifice. Physically, the swelling results from the fact that the growth of the boundary layer inside the nozzle serves as a "vena contracta". Immediately outside the nozzle, an expansion process takes place in which the edge of the jet adjusts to the local pressure in the inviscid core. This phenomena is observed during die-casting manufacturing operations, and is known as *die swell*. Numerous researchers²⁷⁻²⁹ have investigated this problem numerically for steady, 2-D flows.

When the value of Δt_μ is changed, surface waves associated with the start transient are affected, but not the swelling exhibited after the start transient disturbance convects downstream. The surface shape and boundary layer profile is shown in Figure 4 for $\Delta t_\mu = 1, 2$ and 4 time units. When Δt_μ is decreased, the amplitude of the surface wave increases. Note that the assumed ramping generates a waveform with two peaks. The peaks exhibit a spacing of about one orifice radius; the last peak formed has an amplitude roughly double that of the initial crest. This trend is apparent at very short start intervals and ultimately leads to waves which are too steep to resolve with the assumed boundary layer profiles. Since the waves form near the end of the ramp interval, the shorter intervals form the wave earlier in the calculation and the wave has longer to move downstream in the figure. The boundary layer thickness and jet surface shapes appear nearly identical after the wave has been convected downstream from the orifice as discussed previously.

Figure 5 shows how the surface and boundary layer edge velocities change in the nearfield region over the first 5.5 time units of the calculations. For $\Delta t_\mu = 1$ time unit, the edge velocity exhibits a few ripples (associated with the more violent start transient), but essentially remains constant at $u_e = 1$ along the surface at all times. The distance over which the surface velocity transitions from the no-slip condition to $u_s = 1$ grows steadily with time, and is shown to be the same in all three cases. Very near the orifice exit (say, for $z < 1$), results begin to asymptotically approach a fixed u_s value. Unfortunately, computational restrictions prohibit simulations to greater times in which the entire nearfield flow becomes steady. Fortunately, the free surface development occurs in the region very near the orifice exit ($z < 0.5$), such that the current calculations reveal at steady behavior in this region as highlighted in Fig. 4 and subsequent results.

The growth of the boundary layer thickness for a $\Delta t_\mu = 2$ time unit ramp interval is shown in Figure 6. The boundary layer grows rapidly during the start transient, but after about 3 time units, the behavior is invariant with time. In addition, note the dramatic thinning of the boundary layer in this region immediately downstream of the orifice exit. At a distance of only $1/2$ a jet radius downstream of the orifice, the boundary layer has all but vanished. Keeping in mind that a substantial velocity difference exists between surface and edge velocities at this spatial location, the boundary layer is actually transitioning to a shear layer in the region very near the orifice exit. Viscous forces would presumably lead to a broadening of the shear layer as the flow progresses downstream. Since the Reynolds numbers in the simulations are very large, the relaxation lengths are also very large and cannot be resolved due to computational time restrictions.

Figure 7 shows the actual boundary layer profiles near the orifice exit once steady-state conditions have been attained ($t \approx 5.5$). Once again, note that the vertical scale has been amplified dramatically for presentation purposes. In the upper plot, the abscissa represents the velocity relative to the local surface velocity and the ordinate is the distance from the surface (essentially the $-r$ direction). As expected, the boundary layer grows until the orifice exit (Point "3" in the figure). Outside the orifice, the rapid thinning of the boundary layer is evident, and by Point "7" the layer is very thin. The thinning of the boundary layer to a shear layer (vortex tube), is known to be an inherently unstable phenomenon. As the shear layer develops, the presumed boundary layer velocity profile (Eq. 14) becomes erroneous in that it cannot properly model rotation within the boundary layer. Therefore, there will be a tendency toward instability in the region far downstream of the orifice exit plane. In spite of this fact, the near field solution is resolved adequately using Eq. 14 velocity profiles. More research is required to determine whether or not viscous dissipation will ultimately limit the formation of this unstable vortex tube.

Effect of δ_0 , Re and We

A series of calculations were performed to quantify the amount of swelling (as a percentage of orifice radius) for various initial conditions. These calculations were performed at $We = 10^4$ for various δ_0 and Re values. Analysis of the results indicated that the swelling correlated most closely with the thickness of the boundary layer at the exit of the orifice passage. Figure 8 presents a summary of swelling results plotted against this thickness. Results indicate that the amount of swelling is essentially independent of Reynolds number (except for its obvious implications in setting the boundary layer thickness at the exit plane). Assuming that all the swelling takes place within about the first $1/2$ jet radius (which is consistent with our calculations), the net "cone angles" corresponding to the swelling results in Fig. 8 lie in the range of $1-5^\circ$. These small angles would be difficult to observe experimentally. In addition, the bulk of experiments with images near the orifice exit are for conditions where substantial gas-phase pressure interactions are present.

Simulations performed at Reynolds numbers other than 10^4 show similar behavior to that noted in Figs. 3-7. In general, the waves associated with the start transient become more prominent at lower Re values, but the steady-state behavior is quite insensitive to this parameter (for a given value of δ at the orifice exit). Results indicated an insensitivity to Weber number as well; nearly identical surface shapes were obtained for a range of Weber numbers for simulations employing fixed δ_0 and Re values. For these reasons, the swelling phenomena can effectively be characterized by δ_0 alone; the amount of viscosity present is only important in as much as it affects this parameter.

Discussion

Assessing the results shown in the previous section in the light of experimental observations of other researchers as described in the introduction, we can draw several important conclusions. First we note that the present study has shown that steady-state solutions do exist for a high-speed laminar jet in the absence of pressure perturbations from the gas phase. This result indicates that atomization mechanisms which rely on boundary layer relaxation or velocity profile rearrangement cannot generate the instabilities required to atomize the jet. Here, we note that the experiments of Reitz and Bracco³ and others also support this conclusion.

The swelling phenomena depicted in all calculations with this model can aid in explaining many of the experimental observations. In the presence of a gas-phase, the swelling of the jet provides a large-amplitude disturbance for initiation of aerodynamic instabilities which are a critical element of Taylor's model. For the high-speed jet, these instabilities could be amplified so fast that atomization occurs in the region very near

the exit plane. Disturbances from these atomization events could be fed back to the exit plane such that a steady-state solution no longer exists. This scenario is quite plausible for a realistic situation in which the "start transient" is more chaotic and three-dimensional in nature than the idealized approach used in our modeling.

Since the amount of swelling correlates well with the boundary layer thickness at the exit plane, we can also draw some conclusions about the effect of boundary layer turbulence and orifice design. Inasmuch as turbulence reduces the thickness of the boundary layer (as compared to laminar case), the amount of jet swelling would tend to be reduced, and the corresponding perturbations from the gas-phase would also be smaller. On this basis, the high-speed jet (where gas-phase pressure distribution has a major effect) would be *more stable* under the case of a turbulent boundary layer. This conclusion agrees with experimental observations of atomizing jets^{3,9}.

In the low-speed regime, turbulence could play a significant role. Since our solutions (Figs. 3-8) presume no gas-phase interaction and a laminar boundary layer, we predict that steady solutions could be possible in the low-speed regime (particularly for orifice designs generating thin boundary layers at the exit). Under these conditions, forces due to turbulent fluctuations in the radial direction could be the dominant mechanism destabilizing the jet. These observations are consistent with the experimental measurements^{7,8} which were conducted in a lower-speed regime.

As the orifice passage is lengthened (with fixed flowrate), the boundary layer at the exit plane thickens and the swelling phenomena becomes more pronounced. On this basis, one would predict that increasing L/D would cause the jet to be more unstable - a result consistent with experimental observations of McCarthy and Molloy⁴ for the case of a low-speed jet. However, for high-speed jets, Reitz and Bracco observed the opposite trend with increased L/D . As pointed out by these (and other) authors, cavitation may play a substantial role complicating the behavior since it can provide a mechanism for generating *freestream turbulence*⁶ which is not included in our model. In addition, very long nozzles tend to damp out flow perturbations caused by surface imperfections at the orifice inlet. Recent research³¹ has shown this phenomena to be important in determining jet atomization characteristics in some cases. Obviously, this mechanism could also obscure conclusions made regarding orifice L/D effects.

Conclusions

A model has been developed to describe the nonlinear, unsteady evolution of an axisymmetric liquid jet which contains a thin boundary layer. Results from simulations indicate that steady-state solutions do exist for the case of a laminar boundary layer with negligible gas-phase interactions. Under these conditions, the jet swells a few percent in diameter and the boundary layer thins to a shear layer within the first $1/2$ orifice radius of the exit plane. These results demonstrate that atomization mechanisms which rely on boundary layer relaxation cannot explain this process. Moreover, the swelling phenomena could provide a large-amplitude perturbation for amplification of gas-phase pressure interactions and explain experimental observations in both high-speed (atomizing) and low-speed regimes.

The behavior predicted by the model is consistent with experimental observations regarding orifice L/D effects in the case of low-speed flows. However, discrepancies do exist when comparing with the experiments on L/D effects in higher speed flows consistent with the atomization regime. These discrepancies might be explained by cavitation or surface imperfections which complicate this issue.

Acknowledgement

The authors gratefully acknowledge the support of this work by the Air Force Office of Scientific Research under contract number F49620-94-1-0151. In addition, we acknowledge the contributions of Professor Marc Williams in providing us insight in both the development of the model and interpretation of the results.

Nomenclature

\hat{e} = unit vector
 p = pressure
 q = normal velocity
 r = radial coordinate
 Re = Reynolds number
 s = distance along the surface
 t = time
 u = velocity parallel to the wall or free surface
 v = velocity perpendicular to the wall or free surface
 We = Weber number, $We = \rho U^2 a / \sigma$
 x = coordinate parallel to the wall or free surface
 y = coordinate perpendicular to the wall or free surface
 z = axial coordinate
 β = slope of the boundary layer interface
 δ = boundary layer thickness
 δ^* = displacement thickness
 η = boundary layer parameter, $0 \leq \eta = y/\delta \leq 1$
 κ = surface curvature
 Λ = pressure gradient parameter
 μ = viscosity
 ϕ = velocity potential
 σ_{ij} = stress tensor
 θ = momentum thickness

Subscripts:
 e = edge of the boundary layer
 s = surface
 c = core region

Superscripts:
 n = time level

References

1. Taylor, G. I., "Generation of Ripples by Wind Blowing Over a Viscous Fluid", *The Scientific Papers of Sir Geoffrey Ingram Taylor*, 1963.
2. A. A. Amsden, P. J. O'Rourke, and T. D. Butler, KIVA-II - A Computer Program for Chemically Reactive Flows with Sprays, Los Alamos National Labs., LA-11560-MS, 1989.
3. R. D. Reitz and F. V. Bracco, Mechanism of Atomization of a Liquid Jet, *Physics of Fluids*, vol. 25, pp. 1730-1742, 1982.
4. McCarthy, M. J., and Molloy, N. A., "Review of Stability of Liquid Jets and the Influence of Nozzle Design", *The Chemical Engineering Journal*, V 7, pp. 1-20, 1974.
5. Bergwerk, W., "Flow Pattern in Diesel Nozzle Spray Holes," Proceedings of the Institution of Mechanical Engineers, Vol. 173, No. 25, 1959, pp. 655-660.
6. Tamaki, N., Nishida, K., Hiroyasu, H., and Shimizu, M., "Effects of the Internal Flow in a Nozzle Hole on the Breakup Process of a Liquid Jet", Institute for Liquid Atomization and Spray Systems Conference ILASS-96, San Francisco, CA, 1996.
7. Mansour, A., and Chigier, N., "Rayleigh Breakup of Turbulent Columns", Institute for Liquid Atomization and Spray Systems Conference ILASS-94, Bellevue, WA, 1994.
8. Wu, P.-K., Miranda, R. F., and Faeth, G. M., "Effects of Initial Flow Conditions on Primary Breakup of Nonturbulent and Turbulent Round Liquid Jets", *Atomization and Sprays*, V5, pp. 175-196, 1995.
9. Ruiz, F., and Chigier, N., "Parametric Experiments on Liquid Jet Atomization Spray Angle", *Atomization and Sprays*, V1, pp. 23-45, 1991.
10. Leib, S. J., and Goldstein, M. E., "The Generation of Capillary Instabilities on a Liquid Jet", *Journal of Fluid Mechanics*, V 168, pp. 479-500, 1986.
11. Hevert, S., Mahlingham, S., and Daily, J. W., "Velocity Profile Effects on the Stability of a Liquid Jet", Center for Combustion Research, University of Colorado and Boulder, CCR Report No. 91-06, 1991.
12. Shkadov, V. Y., "Wave Formation on the Surface of a Viscous Liquid Due to Tangential Stress", *Fluid Dynamics*, V5, p 423, 1970.
13. Rupe, J. H., "On the Dynamic Characteristics of Free-Liquid Jets and a Partial Correlation with Orifice Geometry", JPL Technical Report No. 32, 1962.
14. Mansour, N. N., and Lundgren, T. S., "Satellite Formation in Capillary Jet Breakup", *Physics of Fluids*, V2, pp. 1141-1144, 1990.
15. Spangler, C. A., Hilbing, J. H., and Heister, S. D., "Nonlinear Modeling of Jet Atomization in the Wind-Induced Regime", *Physics of Fluids*, V 7, No. 5, pp 964-971, 1995.
16. Hilbing, J. H., Heister, S. D., and Spangler, C. A., "A Boundary Element Method for Atomization of a Finite Liquid Jet", *Atomization and Sprays*, V 5, No. 6, pp 621-638, 1995.
17. Hilbing, J. H., "Nonlinear Modeling of Atomization Processes", Ph.D. Dissertation, Purdue University, 1996.
18. Rump, K. M., "Modeling the Effect of Unsteady Chamber Conditions on Atomization Processes", M.S. Thesis, Purdue University, 1996.
19. Unverdi, S. O., and Tryggvason G., "A Front Tracking Method for Viscous, Incompressible, Multi-Fluid Flows", *J. Computational Physics*, V100, pp. 25-37, 1992.
20. Osher, S. and Sethian, J. A., "Fronts Propagating with Curvature Dependent Speed: Algorithms based on Hamilton-Jacobi Formulations", UCLA Computational and Mathematics Report 87-12, 1987.
21. Partridge, P. W., and Brebbia, C. A., "Computer Implementation of the BEM Dual Reciprocity Method for the Solution of General Field Equations", *Communications in Applied Numerical Methods*, V6, pp. 83-92, 1990.

22. Wu, J. C., "Boundary Element Solution of Viscous Flow Problems", *Boundary Element Techniques: Applications in Fluid Flow and Computational Aspects*, C. A. Brebbia and W. S. Venturini, Eds., pp. 1-15, 1987.
23. Wu, J. C., "Boundary Elements and Viscous Flows", *Boundary Element Technology VII*, C. A. Brebbia and M. S. Ingber, Eds., pp. 3-18, 1992.
24. Hailey, C. E., Ingber, M. S., and Tadios, E. L., "Coupling of the Boundary Element Method with an Integral Momentum Boundary-Layer Technique to Calculate Forces and Moments on Three-Dimensional Bodies", *Boundary Element Techniques: Applications in Engineering*, pp. 255-269, 1989.
25. Howarth, L., *Modern Developments in Fluid Dynamics: High Speed Flow*, Oxford University Press, 1953.
26. Currie, I. G., *Fundamental Mechanics of Fluids*, McGraw Hill Publishing Co., 1974.
27. Bush, M. B., and Tanner, R. I., "Numerical Solution of Viscous Flows Using Integral Equation Methods", *International Journal for Numerical Methods in Fluids*, V3, pp. 71-92, 1983.
28. Jin, Xiaoshi, "Boundary Element Study on Particle Orientation Caused by the Fountain Flow in Injection Molding", *Polymer Engineering and Science*, V33, pp. 1238-1242, 1993.
29. Kamiya, N. and Nakayama, K., "Prediction of Free Surface of Die Swell Using the Boundary Element Method", *Computers and Structures*, V46, pp. 387-395, 1993.
30. Karasawa, T., Tanaka, M., Abe, K., Shiga, S., and Kurabayashi, T., "Effect of Nozzle Configuration on the Atomization of a Steady Spray", *Atomization and Sprays*, V2, pp. 411-426, 1992.

Appendix

Detailed equations for the coefficients of the momentum equations for a solid wall (Eq. 12) and along the free surface (Eq. 21) are provided herein.

Solid Wall Boundary Layer Equations

By expanding derivatives and integrals in Eq. 5, the integral form of the momentum equation can be written:

$$A\delta\theta + u_e^2\delta\frac{\partial\theta}{\partial x} + u_e\delta\frac{\partial u_e}{\partial x}\delta^* + B\delta^2 - C\delta^3 = D$$

where:

$$\begin{aligned} A &= 2u_e \left(\frac{\partial u_e}{\partial x} \right) + \frac{u_e^2}{r_o} \left(\frac{\partial r_o}{\partial x} \right) \\ B &= \frac{1}{120} \left[36 \left(\frac{\partial u_e}{\partial t} \right) - \frac{\partial}{\partial t} (\Lambda u_e) \right] \\ C &= \frac{1}{360} \frac{\cos \xi}{r_o} \left[24 \left(\frac{\partial u_e}{\partial t} \right) - \frac{\partial}{\partial t} (\Lambda u_e) \right] \\ D &= \frac{u_e}{\text{Re}} \left(2 + \frac{\Lambda}{6} \right) \end{aligned}$$

Next, we substitute for displacement and momentum thicknesses (Eqs. 9,10) and use the backward difference (Eq. 11) as a local approximation to $\partial\delta/\partial x$. Following this procedure, we group terms to obtain the form shown in Eq. 12. The resulting coefficients can be written:

$$\begin{aligned} c_o &= D \\ c_1 &= E\delta_{i-1}/\Delta x \\ c_2 &= AK + I + B + F + (E + G\delta_{i-1})/\Delta x \\ c_3 &= J - AL + H - C - G/\Delta x \end{aligned}$$

where:

$$\begin{aligned} E &= u_e^2 \left(\frac{37}{315} + \frac{\Lambda}{945} - \frac{\Lambda^2}{9072} \right) \\ F &= \left(\frac{1}{945} - \frac{\Lambda}{4536} \right) \left(\frac{\partial \Lambda}{\partial x} \right) u_e^2 \\ G &= u_e^2 \frac{\cos \xi}{r_o} \left(\frac{5}{63} - \frac{2\Lambda}{945} - \frac{\Lambda^2}{15120} \right) \\ H &= L \frac{u_e^2}{\cos \xi} \left[\sin \xi \left(\frac{\partial \xi}{\partial x} \right) + \frac{\cos \xi}{r_o} \left(\frac{\partial r_o}{\partial x} \right) \right] + u_e^2 \left(\frac{\partial \Lambda}{\partial x} \right) \frac{\cos \xi}{r_o} \left(\frac{1}{945} + \frac{\Lambda}{15120} \right) \\ I &= u_e \left(\frac{\partial u_e}{\partial x} \right) \left(\frac{3}{10} - \frac{\Lambda}{120} \right) \\ J &= u_e \left(\frac{\partial u_e}{\partial x} \right) \left(\frac{\Lambda}{360} - \frac{1}{15} \right) \frac{\cos \xi}{r_o} \\ K &= \left(\frac{37}{315} + \frac{\Lambda}{945} - \frac{\Lambda^2}{9072} \right) \\ L &= \frac{\cos \xi}{r_o} \left(\frac{5}{126} - \frac{\Lambda}{945} - \frac{\Lambda^2}{30240} \right) \end{aligned}$$

and

Free Surface Boundary Layer Equations

In this case, the original form of the momentum equation can be written (after substitution for momentum and displacement thicknesses) as:

$$a_0 + a_1\delta + a_2\delta^2 + a_3\frac{\partial\delta}{\partial x} + a_4\delta\frac{\partial\delta}{\partial x} + a_5\frac{d\delta}{dt} + a_6\delta\frac{d\delta}{dt} = 0$$

Upon application of a backward difference in both space and time, the equation can be rearranged to the result shown in Eq. 21. Here, the b_i values can be expressed:

$$b_0 = a_0 - a_3\frac{\delta_{i-1}^n}{\Delta x} - a_5\frac{\delta_i^{n-1}}{\Delta t}$$

$$b_1 = a_1 + \frac{a_3}{\Delta x} - a_4\frac{\delta_{i-1}^n}{\Delta x} + \frac{a_5}{\Delta t} - a_6\frac{\delta_i^{n-1}}{\Delta t}$$

$$b_2 = a_2 + \frac{a_4}{\Delta x} + \frac{a_6}{\Delta t}$$

where the coefficients $a_0 - a_6$ are:

$$a_0 = r_o u_e \left(q_s + \frac{\partial\phi}{\partial y} \right) - \frac{r_o}{Re} \left[\left(\frac{\partial v}{\partial x} \right)_{y=\delta} - \left(\frac{\partial v}{\partial x} \right)_{y=0} \right]$$

$$a_1 = \frac{r_o}{2} \left(\frac{d\hat{e}_x}{dt} \right)_y \left(q_s - \frac{\partial\phi}{\partial y} \right) + \left(\frac{da_5}{dt} \right) - \cos\xi u_e \left(q_s + \frac{\partial\phi}{\partial y} \right) + \frac{\cos\xi}{Re} \left(\frac{\partial v}{\partial x} \right)_{y=\delta} + r_o \left(\frac{\partial P}{\partial x} \right)$$

$$+ \frac{1}{35} \left\{ \frac{\partial r_o}{\partial x} (17u_e^2 - 13u_e u_s - 4u_s^2) + r_o \left[34u_e \frac{\partial u_e}{\partial x} - 13 \left(u_e \frac{\partial u_s}{\partial x} + u_s \frac{\partial u_e}{\partial x} \right) - 8u_s \frac{\partial u_s}{\partial x} \right] \right\}$$

$$a_2 = \frac{1}{2} \frac{da_6}{dt} - \frac{\cos\xi}{4} \left(\frac{d\hat{e}_x}{dt} \right)_y \left(q_s - \frac{\partial\phi}{\partial y} \right) - \frac{\cos\xi}{2} \left(\frac{\partial P}{\partial x} \right)$$

$$+ \frac{1}{105} \left\{ \sin\xi \left(\frac{\partial\xi}{\partial x} \right) (37u_e^2 - 32u_e u_s - 5u_s^2) - \cos\xi \left[(74u_e - 32u_s) \frac{\partial u_e}{\partial x} - (32u_e + 10u_s) \frac{\partial u_s}{\partial x} \right] \right\}$$

$$a_3 = \frac{r_o}{35} (17u_e^2 - 13u_e u_s - 4u_s^2)$$

$$a_4 = -\frac{2\cos\xi}{105} (37u_e^2 - 32u_e u_s - 4u_s^2)$$

$$a_5 = \frac{r_o}{5} (3u_e + 2u_s)$$

$$a_6 = -\frac{\cos\xi}{5} (4u_e + u_s)$$

The velocity derivative $\partial v/\partial x$ can be written in terms of derivatives of ϕ and q , as well as local surface geometry (ξ , β). Other spatial derivatives appearing in these equations are evaluated using centered differencing since at a given time, arguments in these derivatives are known along the entire surface. Time derivatives appearing in the above relations are evaluated using a backward difference as utilized for the unknown δ .

Figure Captions

Figure 1. Axisymmetric Boundary Layer Nomenclature.

Figure 2. Computational Domain for the Finite-Length Viscous Jet. (Nodes Along Inner Edge of Boundary Layer are not Shown for Clarity)

Figure 3. Boundary Layer Development, $We = 10^4$, $Re = 10^4$, $\Delta t_\mu = 2.0$. Here the Upper Curves Represent the Jet Surface While the Lower Curves Denote the Inner Edge of the Boundary Layer.

Figure 4. Jet Profile Near the Orifice Exit for $We = 10^4$, $Re = 10^4$ and $t = 5.8$ Time Units.

Figure 5. Edge and Surface Velocities, $We = 10^4$, $Re = 10^4$, and $\Delta t = 0.5$ Between Curves, (a) $\Delta t_\mu = 1$, (b) $\Delta t_\mu = 2$, (c) $\Delta t_\mu = 4$ Time Units.

Figure 6. Boundary Layer Thickness, $We = 10^4$, $Re = 10^4$, $\Delta t_\mu = 2.0$, with $\Delta t = 0.5$ Between Curves.

Figure 7. Boundary Layer Velocity Profiles at Various Locations Along the Jet, $We = 10^4$, $Re = 10^4$.

Figure 8. Jet Swelling as a Function of Boundary Layer Thickness at the Orifice Exit Plane and as a Percentage of Orifice Radius, $We = 10^4$.

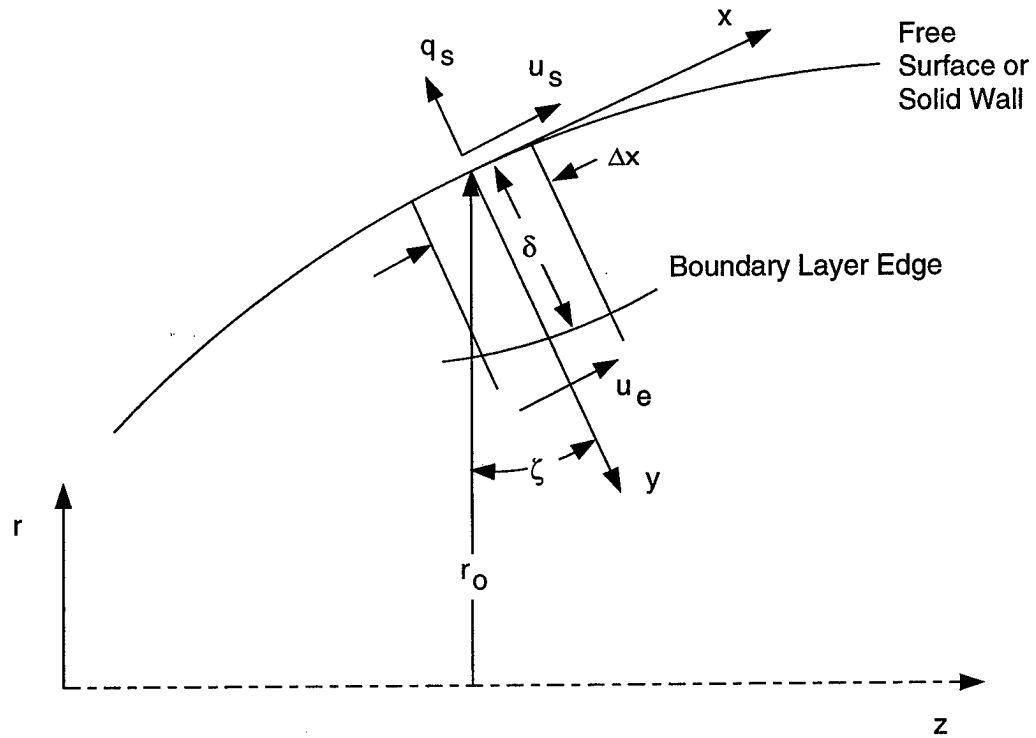


Figure 1: Axisymmetric Boundary Layer Nomenclature.

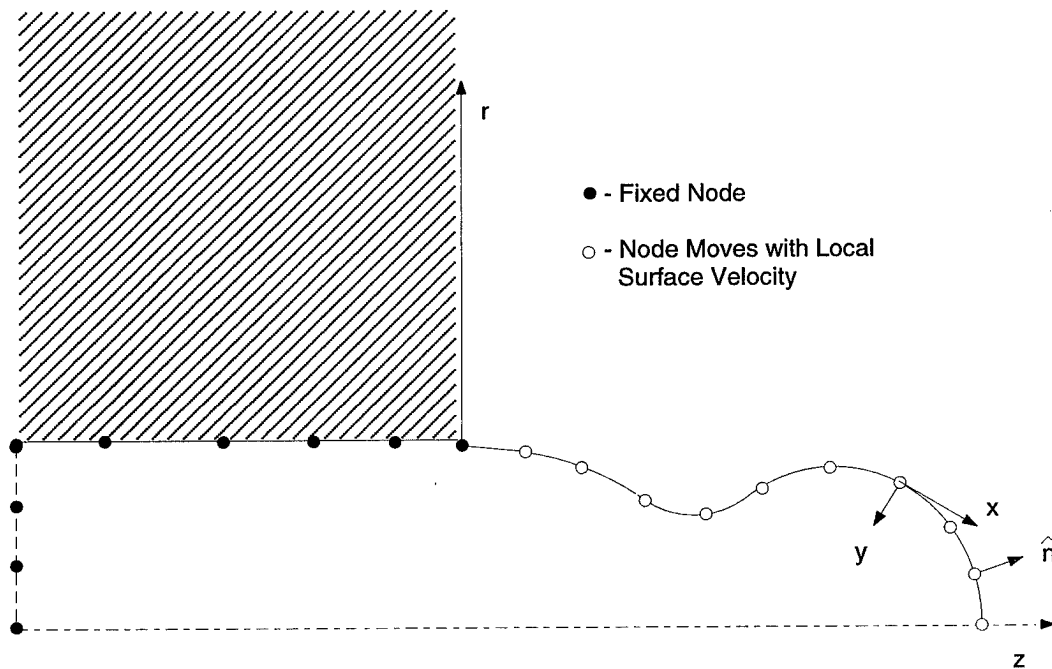


Figure 2: Computational Domain for Finite-Length Viscous Jet. (Nodes Along Inner Edge of Boundary Layer are not Shown for Clarity)

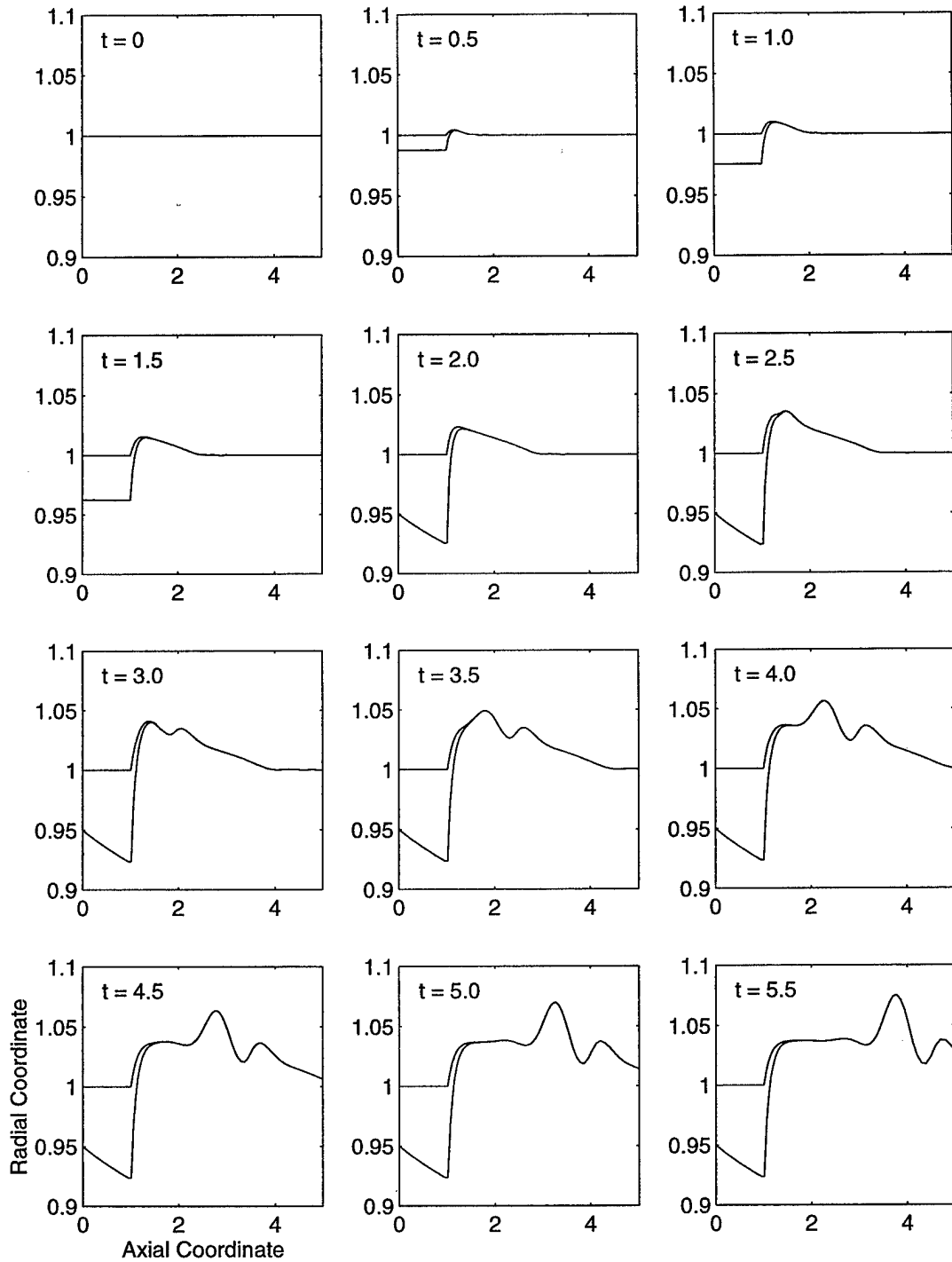


Figure 3: Boundary Layer Development, $We = 10^4$, $Re = 10^4$, $\Delta t_\mu = 2.0$. Here the Upper Curves Represent the Jet Surface While the Lower Curves Denote the Inner Edge of the Boundary Layer.

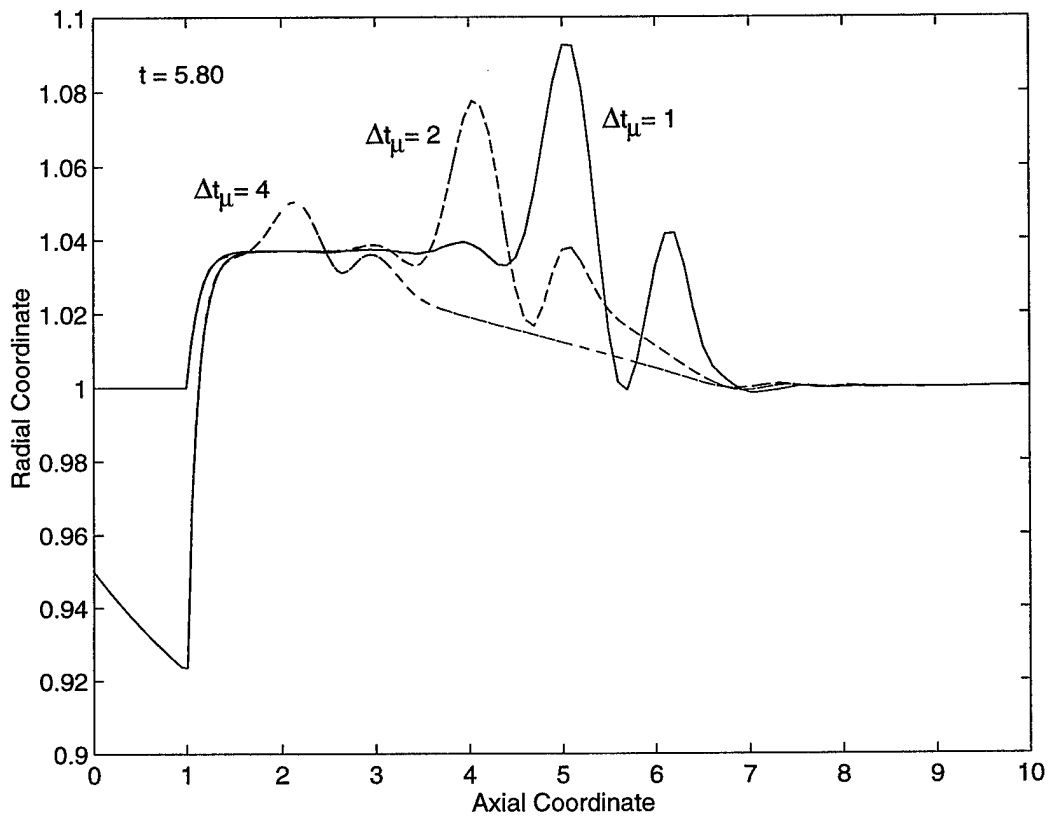


Figure 4: Jet Profile Near the Orifice Exit for $We = 10^4$, $Re = 10^4$ and $t = 5.8$ Time Units.

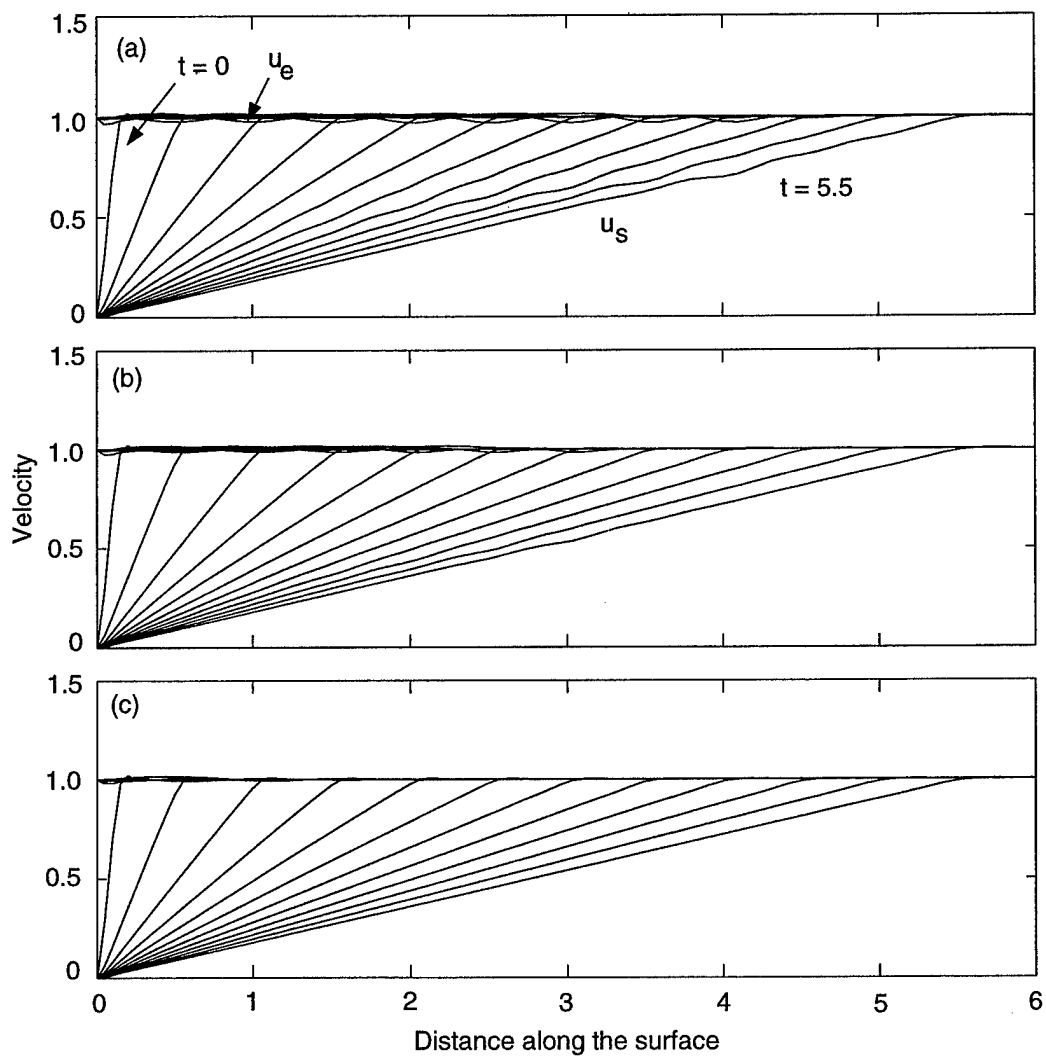


Figure 5: Surface Velocity, $We = 10^4$, $Re = 10^4$, and $\Delta t = 0.5$ Between Curves, (a) $\Delta t_\mu = 1$, (b) $\Delta t_\mu = 2$, (c) $\Delta t_\mu = 4$ Time Units.

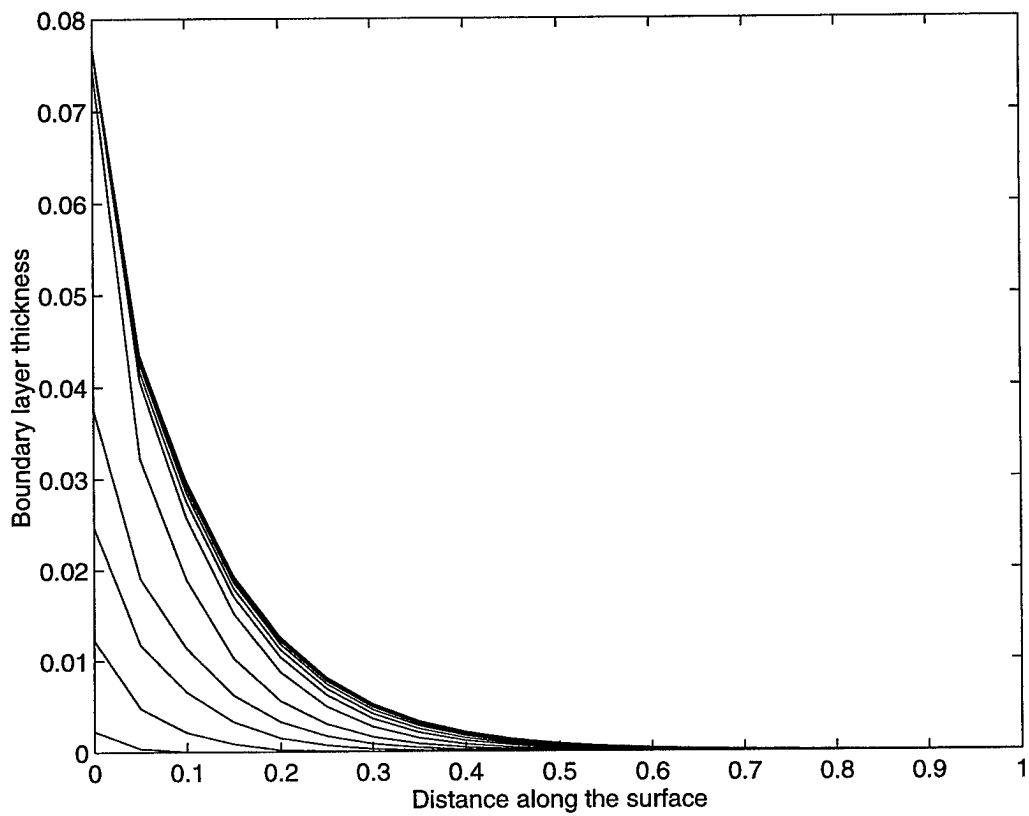


Figure 6: Boundary Layer Thickness, $We = 10^4$, $Re = 10^4$, $\Delta t_\mu = 2.0$, with $\Delta t = 0.5$ Between Curves.

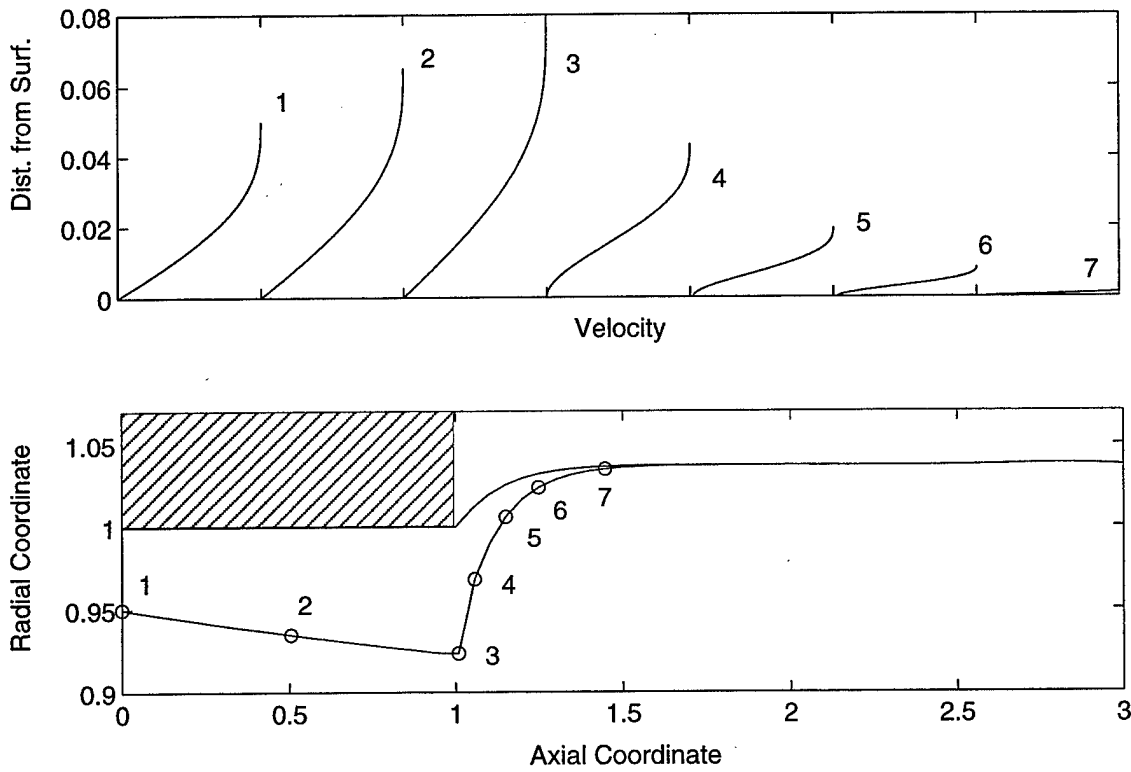


Figure 7: Boundary Layer Velocity Profiles at Various Locations Along the Jet, $We = 10^4$, $Re = 10^4$.

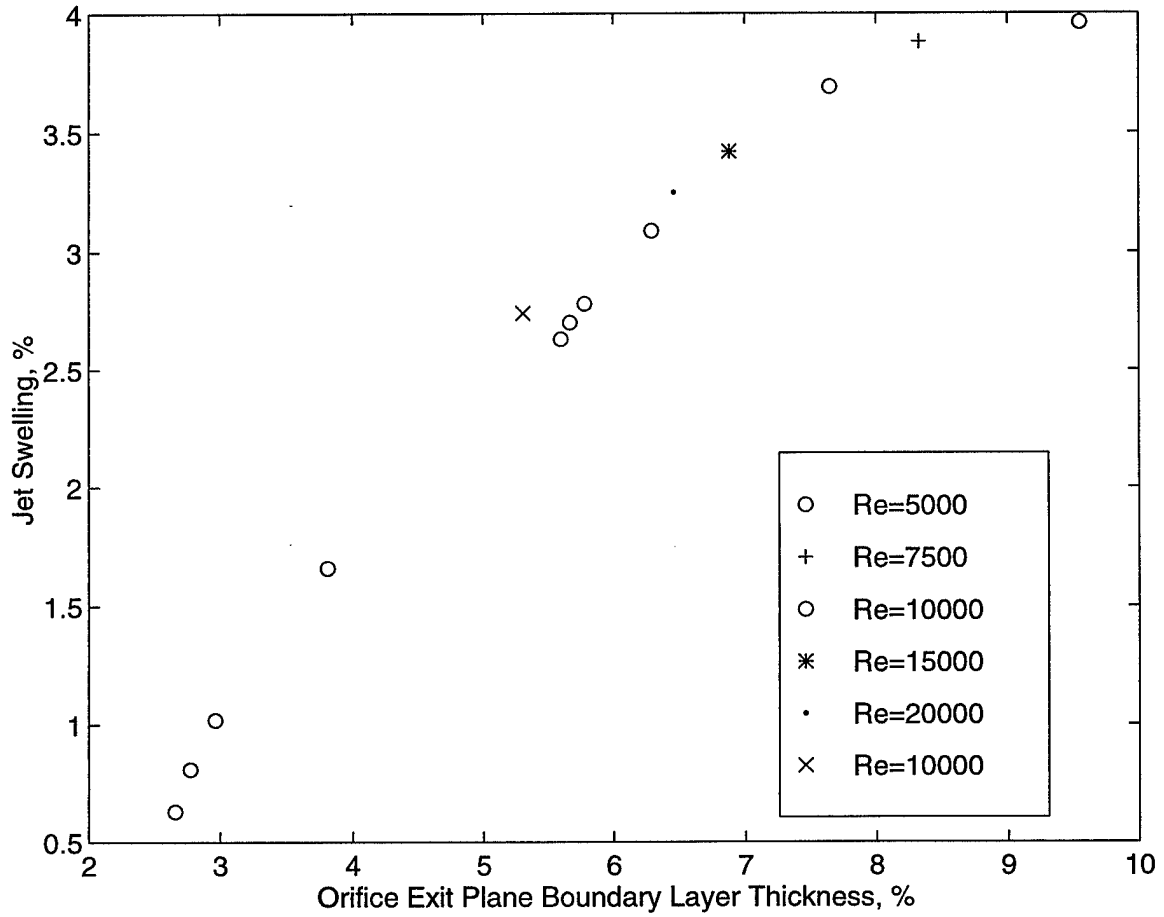


Figure 8: Jet Swelling as a Function of Boundary Layer Thickness at Orifice Exit Plane as a Percentage of Orifice Radius, $We = 10^4$.

6 Appendix B - F-1 Engine Simulations

Chao, C. and Heister, S. D., "Contributions of Atomization to F-1 Engine Combustion Instabilities", *Journal of Propulsion and Power*, In Review, 1997.

CONTRIBUTIONS OF ATOMIZATION TO F-1 ENGINE COMBUSTION INSTABILITIES

S. D. Heister *; and C. Chao †

January 28, 1999

Nomenclature

a = orifice radius
 P = pressure
 q = velocity normal to local surface
 t = time
 U = velocity
 We = Weber number, $We = \rho_g U_g^2 a / \sigma$
 x = horizontal coordinate
 y = vertical coordinate
 κ = surface curvature
 ρ = density
 ϵ = density ratio, ρ_g / ρ
 σ = surface tension
 ω_g = acoustic oscillation frequency
 ω_n = natural frequency of column (Eq. 1)
 ϕ = velocity potential

Subscripts

$()_g$ = gas phase

Abstract

Numerical simulations have been performed to assess the nonlinear, unsteady behavior of fuel jets emanating from an injector in the presence of a transverse (tangential) acoustic wave. Conditions for the simulations have been set to pertain to injector designs used during the development of the F-1 liquid rocket engine. Results indicate that injector designs which were unstable have substantial coupling between the acoustic wave and the natural frequency of oscillation of the fuel column emanating from the orifice. This instability scenario is discussed in the context of other theories offered as explanation for F-1 instabilities.

*Associate Professor, Associate Fellow, AIAA
Purdue University, West Lafayette, Indiana, 47907

†Graduate Research Assistant, School of Aeronautics and Astronautics. Member, AIAA
Copyright © 1997 by the American Institute of Aeronautics and Astronautics, Inc. All rights reserved.

Introduction

During the development of the F-1 liquid rocket engine which was used as first stage propulsion on the Saturn V launch vehicle, tangential mode instabilities were observed in a variety of injector designs. Literally thousands of tests were conducted¹, providing the most extensive fullscale database available even today. For this reason, the F-1 engine continues to be a subject of study; providing a substantial amount of engine response data with which to correlate new experiments and analytic/numerical models.

The F-1 engine utilized liquid oxygen and RP-1 (kerosene) propellants in an impinging-type injector design depicted schematically in Fig. 1. Fuel was injected in an impinging doublet pattern in which the angle between the jets was typically 40°, while the LOX was injected in a triplet pattern in which an axial center jet is mixed with two canted jets at the impingement point. The angle between the canted jets was typically kept at 40° as in the case of the fuel jets. Various injector designs were tested in the program; main differences between injectors include the orifice size/number and the presence (or absence) of baffles. Many of the engines using the early injector designs exhibited instabilities in the 450-550 Hz range consistent with the first tangential mode for this large engine.

In recent years, several theories have been adopted to explain the presence of these instabilities in F-1 and other impinging element injector designs. Most of these theories focus on the behavior of the fuel jets because they are the least volatile of the two propellants and most likely to provide a rate-controlling mechanism for combustion processes. A stability correlation after Hewitt² indicates that the maximum sustainable instability frequency decreases as the injection parameter a/U_i is increased. Here, U_i is the fuel injection velocity and a is the corresponding orifice radius. The basic jet atomization frequency resulting from the impingement process has been shown to be of the same order as those observed in testing^{2,3}, thereby providing one mechanism in agreement with Hewitt's criteria. In addition, flame straining and extinction times have been shown⁴ to provide frequencies in accordance with the observed trends and those predicted by Hewitt's criteria.

Finally, fuel jet aerodynamic excitation⁵ has been suggested as a potential contributor since the column of liquid has a natural frequency of excitation which may be near that of the acoustic frequency. In this paper, we investigate this latter theory with some detailed simulations for both stable and unstable F-1 injector designs. The next section provides a brief description of the model, followed by results and discussion in the context of the other theories described above.

Model Description

The two-dimensional model used in the simulations conducted herein makes use of Boundary Element Methods (BEMs) to provide high-resolution, time-accurate modeling of a liquid column subjected to acoustic forces from the gaseous phase. Since we have described details of the fully-coupled, nonlinear models in previous work⁵⁻⁸, we shall provide only a brief discussion in the present study. The model used for the present simulations presumes incompressible, inviscid flow in both liquid and gaseous phases. Since the orifice diameter is typically 2-3 orders of magnitude less than the chamber diameter, an acoustic wave can effectively be represented as a time-varying incompressible flow; i.e. spatial variations across the tiny jet length scale are assumed to be negligible. The inviscid assumption is necessary for use of BEMs; transient flow separation present in a complete viscous solution introduces formidable complications in the modeling.

We choose the jet radius (a), liquid density (ρ), and a characteristic peak acoustic velocity (U_g) as dimensions. Under this nondimensionalization, the Weber number, $We = \rho_g U_g^2 a / \sigma$ and the gas/liquid density ratio, $\epsilon = \rho_g / \rho$ are two dimensionless variables characterizing these flows. A third parameter which is important in these unsteady simulations is the natural (lowest order) excitation frequency of the column. In Ref. 5, a linear analysis, similar to that conducted by Lamb for vibrations of a droplet, provides the natural frequency of the fuel jet under transverse excitation:

$$\omega_n = \sqrt{\frac{6\epsilon}{(1+\epsilon)We}} \quad (1)$$

The ratio of the imposed acoustic frequency (ω_g) and ω_n represents another important parameter in this particular problem.

For an inviscid gas or liquid domain, velocity potentials ϕ_g, ϕ exist and must satisfy Laplace's equation:

$$\nabla^2 \phi = \nabla^2 \phi_g = 0 \quad (2)$$

The unsteady Bernoulli equation provides conditions relating velocity potentials at the gas/liquid interface:

$$\frac{\partial \phi}{\partial t} + \frac{1}{2}(\nabla \phi)^2 + P_g + \frac{\kappa}{We} = 0 \quad (3)$$

where P_g is the dimensionless gas pressure at the interface, and κ is the local surface curvature. On the gas side of the interface, Bernoulli's equation is:

$$\epsilon \frac{\partial \phi_g}{\partial t} + \frac{\epsilon}{2}(\nabla \phi_g)^2 + P_g = 0 \quad (4)$$

Mathematically, Eqs. 2-4 provide a well-posed set of equations for velocity potentials, the gas pressure at the interface, and the shape of the interface (implicit in the surface curvature, κ). This set of equations is solved using a BEM which begins with an integral representation of Laplace's equation:

$$\alpha \phi(\vec{r}_i) + \int_{\Gamma} \left[\phi \frac{\partial G}{\partial n} - qG \right] d\Gamma = 0 \quad (5)$$

where $\phi(\vec{r}_i)$ is the value of the potential at a point \vec{r}_i , Γ denotes the boundary of the domain, and G is the free-space Green's function corresponding to Laplace's equation. An analogous form of Eq. 5 can also be derived for the gas phase potential. For a well-posed problem, either ϕ or $q = \partial \phi / \partial n$ must be specified at each "node" on the boundary. Here n is the outward normal to the boundary so that q represents the velocity normal to the boundary. The quantity α in Eq. 5 results from singularities introduced as the integration passes over the boundary point, \vec{r}_i .

In the case of a 2-D flow (letting x and y represent the coordinates), the free-space Green's function may be written:

$$G = \frac{1}{2\pi} \ln |\vec{r} - \vec{r}_i| = \frac{1}{4\pi} \ln [(x - x_i)^2 + (y - y_i)^2] \quad (6)$$

We presume that both ϕ and q vary linearly along the length of a given element. This assumption permits the construction of a set of matrices involving the nodal values of ϕ and q and the integrals (over a given element) given in Eq. 5. For this linear element case, the integration across a segment can be carried out analytically. Singularities resulting from integration across a segment containing the base point are also integrable⁶.

The main challenge in developing models capable of tracking large deformations of an interface lies in the treatment of the free surface itself. Here, the use of a BEM is desirable since nodes can be tracked such that they always lie on the interface; no interpolations of surface location (and the inherent numerical errors) are required. Since capillary forces are important, it is crucial to develop a treatment capable of accurately determining surface curvature at all times during the simulation. For this reason, all models employ fourth-order centered differencing (on a generalized, variable spacing mesh) to determine surface curvature⁷.

We track surface nodes along the local *liquid* velocity vector. Under this assumption, flow kinematics require:

$$\frac{Dx}{Dt} = \frac{\partial \phi}{\partial x} \quad \frac{Dy}{Dt} = \frac{\partial \phi}{\partial y} \quad (7)$$

where the notation $D()/Dt$ implies a Lagrangian derivative for points on the surface moving with the local liquid velocity. Recognizing that our BEM solver will return velocities normal to the surface, we employ the velocity transformations:

$$\frac{\partial \phi}{\partial y} = \frac{\partial \phi}{\partial s} \sin(\beta) + q \cos(\beta) \quad \frac{\partial \phi}{\partial x} = \frac{\partial \phi}{\partial s} \cos(\beta) - q \sin(\beta) \quad (8)$$

where β is the local wave slope and $\partial \phi / \partial s$ is the velocity tangential to the local surface. This tangential velocity is calculated using 5-point centered differences on surface values of ϕ . The local wave slope, β , is calculated by determining the slope of a parabola fit through three points in the region of interest⁹.

Dynamics of the interface are addressed through the unsteady Bernoulli equation. The relations in Eqs. 3 and 4 are valid for an Eulerian system in which the grid remains fixed. Since we desire nodes on the interface to move in a Lagrangian sense, an Eulerian – Lagrangian transformation is required. Here, we “track” nodes on the interface by assuming that they travel with the local *liquid* velocity. Under this assumption, the Eulerian – Lagrangian transformation can be written:

$$\frac{D(\cdot)}{Dt} = \frac{\partial(\cdot)}{\partial t} + \nabla\phi \cdot \nabla(\cdot) \quad (9)$$

and the applicable forms of the Bernoulli equations (Eqs. 3,4) become:

$$\frac{D\phi}{Dt} = \frac{1}{2} (\nabla\phi)^2 - P_g - \frac{\kappa}{We} \quad (10)$$

$$\epsilon \frac{D\phi_g}{Dt} = \epsilon \nabla\phi \cdot \nabla\phi_g - \frac{\epsilon}{2} (\nabla\phi_g)^2 - P_g \quad (11)$$

Equations 7, 10, and 11 are integrated in time using a fourth-order Runge-Kutta scheme. A stable, consistent procedure⁶ has been developed to handle the coupled, nonlinear boundary conditions at the interface (Eqns 10,11). Equation 10 is integrated to update ϕ values on the interface which permits solution of Laplace’s equation in the liquid phase to obtain surface velocities. Since we track nodes along this velocity vector, we must have $q_g = -q$ for gas nodes on the free surface. Using this condition, Laplace’s equation is solved in the gas phase to determine ϕ_g on the surface. This current ϕ_g value is used in a first order backward difference to estimate $D\phi_g/Dt$ such that Eq. 11 can be used to solve to the updated P_g values.

Since the nodes on the interface are allowed to move with their local velocity, over time they tend to group themselves in regions of high curvature. This phenomena leaves regions of lower curvature poorly defined. To alleviate this problem, the surface mesh is regrided using a series of cubic splines (for surface coordinates and ϕ) at each time step to keep the spacing between the nodes constant along the surface.

Computational Grid and Boundary Conditions

Figure 2 highlights the computational grid and boundary conditions for the simulation of jet behavior in the presence of a transverse acoustic excitation. The 2-D assumption restricts us to considering a “slice” of the jet upstream of the impingement point shown in Fig. 1. The Weber number (We), gas/liquid density ratio (ϵ), and gas/liquid frequency ratio (ω_g/ω_n) are input parameters for a given simulation. We presume that the acoustic oscillation can be represented by a simple cosine wave, so that the gas-phase velocity potential far from the column may be written:

$$\phi_g = x \cos(\omega_g t/2) \quad (12)$$

The factor of 1/2 is included inside the cosine function to account for the fact that the inviscid solution is insensitive to the direction of gas flow, i.e. the column will broaden under the presence of an acoustic wave moving either direction. Numerical experiments⁵ using the known analytic solution for uniform flow over a cylinder indicate that farfield conditions may be accurately assumed if the outer gas boundary is placed 15 jet radii from the origin.

The column is subjected to a virtual mass force due to the accelerating external flow. Since there is a freestream pressure gradient present, the flow is not symmetric about the y axis. However, for low gas density flows, similar analyses on droplets¹⁰ indicate that the apparent mass force is negligible. In addition, we have also run numerous simulations for the complete upper half plane⁵ (as shown in Fig. 2); at the conditions of interest, the quarter-plane results are equivalent. The advantage in using the quarter-plane is obvious; it halves the number of nodes in the simulation. Since the matrix inversion time scales with the cube of the number of nodes, the quarter-plane domain takes about 1/8 the time to run as compared to the half-plane domain. For this reason, we utilized the domain shown in Fig. 2 for all simulations presented herein.

For liquid nodes along the assumed symmetry axes in Figure 2 the normal velocity, q , is assumed to be zero. For the gas domain, symmetry dictates that $q_g = 0$ along the line $y = 0$, the assumed symmetry along the $x = 0$ line dictates that ϕ_g be a constant equivalent to the value prescribed by the freestream potential

Table 1: F-1 Injector Design Data: Fuel Orifice Test Data

Injector Designation	Dimm. mm	ω_g , Hz	$\Delta P/P_c$ %	ω_g/ω_n
5U-Flatface	3.66	538	150	3.0
5U-Baffled	4.04	460	65	2.9
Double Row Cluster (DRC)	2.79	454	400	1.7
Prelim. Flight Rating Tests (PFRT)	5.79	-	0	5.1*
Flight Rating Test (FRT)	7.14	-	0	7.1*

* Assumes $\omega_g = 460$ Hz 1T chamber mode.

in Eq. 12. The Bernoulli equations (Eqs. 11,12) prescribe the necessary conditions for the interface. A dimensionless time step of 0.005 was used in all simulations.

Typical grids employ 21 nodes on outer boundary of gas and 15 gas nodes along each symmetry plane for the gas phase. In the liquid phase, 26 nodes had been used on the interface and nine nodes along each symmetry plane. Figure 3 depicts the column aspect ratio as a function of time for typical We and ϵ values for three different computational grids. In this figure, the fine and coarse grids employ double and half the number of nodes respectively, as compared to the “basis grid” described above. The simulation demonstrates that the solution is independent of grid provided we use at least as many nodes as that employed in the basis grid. Using this grid, the model can also replicate analytic solutions for uniform flow over a cylinder to within 1%. For these reasons, this grid has been utilized for all results in this work.

Table 1 highlights data¹ from both unstable and stable injectors tested during F-1 engine development. The Flight Rating Test (FRT) design is essentially the configuration which was used on actual flight units. The most unstable injector tested was the Double Row Cluster (DRC) which exhibited chamber pressure oscillations as high as 400% of the mean value. Using a dimensional form of Eq. 1, column natural frequencies were calculated for each fuel orifice design $\omega_n = \sqrt{6\rho_g\sigma/[(\rho + \rho_g)a^3]}$ using a fuel specific gravity of 0.81 and surface tension of 0.0019 lbf/f. Using this information, the frequency ratio ω_g/ω_n was then computed. Gas density was estimated for nominal combustion conditions (chamber pressure of 1125 psi, mixture ratio of 2.4) using one-dimensional chemical equilibrium calculations. The frequency ratio for the stable injectors was estimated assuming a first tangential mode frequency of 460 Hz for this large chamber.

Modeling Results

To highlight differences between injectors, we decided to model the most unstable (DRC) and stable (FRT) injector designs in our simulations. Using nominal fuel and gas densities, the applicable density ratio for the F-1 simulations is $\epsilon = 0.0064$. Prescribing an acoustic intensity (in terms of a Weber number) is difficult because the exact acoustic environment to which the fuel jets are exposed is largely unknown and not measured in typical testing. For this reason, a baseline Weber number of 0.1 was assumed for most simulations. This value corresponds to peak acoustic velocities in the range from 1-2 f/s; modest perturbations which could be consistent with early stages of instability.

In addition to actual column shapes, we have found that tracking the motion of the top node ($x = 0$) on the interface to provide insight into the nonlinear deformation processes depicted by the model. In addition, the column aspect ratio (AR), defined as the ratio of column height to its width, is one variable which quantifies the level of deformation of the jet. Prolate and oblate shapes are formed when $AR > 1$ and $AR < 1$, respectively.

Using the frequency ratios provided in Table 1, Figures 4 and 5 depict the response of DRC and FRT injector fuel jets in terms of top node radial motion and column aspect ratio. In Fig. 4, we see that both designs exhibit a bounded response even though the acoustic energy input is not bounded. This classic nonlinear behavior is attributed to the downward shift in the column’s natural frequency as the deformation level increases. Under finite deformation, the natural frequency will be lower than the value predicted by the linear theory (Eq. 1); the shift eventually grows large enough that the constant frequency acoustic signal begins to work out of phase with the column’s motion. In the case which was investigated, destructive

interference begins to dominate near $t = 45$ for the DRC injector design. Note that the overall response for the FRT is much more chaotic due to the fact that ω_n is over seven times larger than the acoustic frequency for this design. Rutz⁵ has shown substantial coupling in the motion for frequency ratios in the range $0.5 < \omega_g/\omega_n < 2$. The fact that the DRC design has a frequency ratio of 1.7 is the main factor explaining its increased response to the tangential mode frequencies present in the F-1 engine.

Figure 5 depicts the evolution of column aspect ratios to the assumed acoustic wave for both FRT and DRC designs. The FRT design spends almost all the time in the prolate mode ($AR > 1$). This behavior is due to the fact that the column's natural frequency is so low (relative to the forcing frequency) that it is responding primarily to the mean dynamic pressure generated by the acoustic wave. The DRC design shows a more harmonic response with oscillation between prolate and oblate shapes. The overall amplitude of the AR excursion is greater for the DRC design, thereby indicating more drastic changes in shape than the FRT design.

This factor is also evident in the actual jet cross-sectional shapes, as revealed in Fig. 6. In this figure, jet shapes are drawn to scale; the fact that the DRC elements are smaller diameter is quite evident. Here, dimensional times are presented (in units of milliseconds) as measured with respect to the beginning of the simulation. Times were selected to correspond with peaks in the DRC response on the aspect ratio plot. The large distortions in the DRC cross-section are much more pronounced than those of the FRT design. We might point out that this conclusion is true in general; even times at which the FRT response is a maximum reveal jet shapes with small distortion as compared to the DRC design.

Since the Weber number of 0.1 selected for the previous simulations was arbitrary, a series of simulations were conducted to determine the sensitivity of both designs to changes in this parameter. Results of these simulations are presented in Fig. 6 in terms of the actual peak speed in the acoustic wave (U parameter in We). Here, simulations were run for extended times, and the maximum aspect ratio (in prolate form) was determined for each injector. The results indicate that the DRC design exhibits more deformation than the FRT design at *all* conditions simulated. In fact, the deformations in the DRC design were so large that we were unable to obtain stable solutions for peak acoustic velocities exceeding 0.6 m/s in this case. In addition, the response (as measured in terms of AR) is more sensitive to changes in gas velocity for the DRC design. This heightened sensitivity can be viewed as a higher "gain factor" for pumping instabilities in the DRC design; i.e. small changes in velocity lead to rather substantial changes in jet distortion.

Discussion

There is substantial evidence that the atomization process plays an important role in many liquid rocket combustion instabilities. Here, it is important to note that atomization cannot in itself fully explain an instability since it is only through resonant combustion that energy is made available to enhance a small perturbation. However, basic atomization processes can be responsible for creation of droplet fields which do support resonance. In fact, baffles are typically designed to isolate the atomization region from the combustion regions^{11,12}.

The results obtained in the previous section support the conclusion that the frequency response of the column of fluid emanating from the orifice should be a consideration in the design of large liquid rocket engine injectors. If the column realizes substantial deformation, aerodynamic drag will be enhanced and the impingement dynamics will be effected. Early experimental work¹³ indicated that liquid streams could in fact respond to high-frequency oscillations. More recently, the impingement region¹⁴ has been shown to be very complex and highly dependent on alignment of the impact point. Depending on operating conditions, streams can be reflected, well mixed, or actually transmitted through the desired impact locale. Finally, previous experiments indicate that stability of impinging element injectors could be improved by using contoured orifice inlets¹¹; the implication here is that this technique improved the accuracy of stream impingement and hence spray quality.

Given the sensitivity of the impingement process to jet alignment, the present scenario provides a reasonable explanation for the generation of instabilities. Presumably, droplet sizes and burning times are also effected when the impingement region atomization is varied, thereby providing the periodic energy source required for instability. One could correlate the data in Table 1 on this basis; the frequency ratio ω_g/ω_n is the key parameter in the present scenario. Figure 8 provides results for this simple correlation for the five

injector designs highlighted in Table 1. Here, results indicate stability if the frequency ratio exceeds a value of about 3; beyond this value, the column frequency is too low to generate appreciable response from the imposed external perturbation.

We should note that several attempts were made to include data from other testing¹⁵⁻¹⁷ and smaller engines¹² (such as Space Shuttle and Apollo maneuvering engines) with only limited success. The bulk of these tests utilized subscale designs with smaller injector element diameters than those which would be used in full scale engines. It is possible that these subscale designs do not provide sufficiently intact jet boundaries upstream of the impingement point for the present analysis to be applicable. In addition, it is difficult to predict the amount of acoustic energy available at the injector face itself; specular reflections within the droplet field can provide substantial damping of any presumed tangential wave. Since the damping depends on the size and orientation of the droplet field, the subscale tests will not replicate the full scale test article in this regard. Another factor involves the higher acoustic frequencies associated with the subscale designs. The length of the acoustic waves may be so short that a separation region does not have time to develop on the lee-side of the jets, thereby limiting the deflection due to periodic drag. Herein lies one of the main problems with subscale testing; while jet velocities can be replicated in such tests, the atomization process and resultant drop sizes cannot be matched.

One should not be so naive as to expect a single explanation for phenomena as complex as liquid engine combustion instabilities. Flame straining and periodic atomization theories can in fact provide insight into the overall process, but actual instabilities may occur as a result of several factors. From a practical standpoint, the F-1 data suggest that larger orifices are more stable. This trend is predicted by *all* the present theories, including Hewitt's stability criteria. However, the main effect of increasing orifice size is to move the combustion zone downstream; a design rule which is known to stabilize many different types of injectors. At the present time, we are forced to use the limited theories as guidelines recognizing that they can address very specific aspects of a multifaceted problem.

Conclusions

Impinging element injectors, such as those used on the F-1 engine rely on the injection of propellant in well-defined streams. These columns of fluid have a natural frequency (based on linear analysis) of $\sqrt{6\rho_g\sigma/[(\rho + \rho_g)\alpha^3]}$. Nonlinear, unsteady boundary element simulations of the column distortion indicate strong coupling with the acoustic field if the acoustic frequency lies near this column natural frequency. In the case of the F-1 engine, the degree of instability (as measured by chamber pressure oscillations) correlates well with this frequency ratio (ω_g/ω_n). While the actual F-1 instability mechanism could be multifaceted, this aerodynamic interaction should be considered in the design of future large liquid engines utilizing similar impinging element injectors.

Acknowledgement

The authors gratefully acknowledge the support of this work by the Air Force Office of Scientific Research under contract number F49620-96-1-0239 under the project management of Dr. Mitat Birkan.

References

1. Oefelein, J. C. and Yang, V., "Comprehensive Review of Liquid-Propellant Combustion Instabilities in F-1 Engines," *Journal of Propulsion and Power*, V 9, 1993, pp. 657-677.
2. Anderson, W.E., Ryan, H.M., Santoro, R.J., and Hewitt, R.A., "Combustion Instability Mechanism in Liquid Rocket Engines Using Impinging Jet Injectors", AIAA 95-2357, AIAA Joint Propulsion Conference, July, 1995.
3. Anderson, W.E., and Santoro, R.J., "The Effects of Drop Size Distribution and Atomization Periodicity on Combustion Response", AIAA 96-3027, AIAA Joint Propulsion Conference, July, 1996.
4. Kim, J.S., and Williams, F.A., "Acoustic-Instability Boundaries in Liquid-Propellant Rockets: Theoretical Explanation of Empirical Correlation", *Journal of Propulsion and Power*, V 12, pp. 621-625, 1996.
5. Rutz, M. W., "Effect of Transverse Acoustic Oscillations on Behavior of a Liquid Jet", M.S. Thesis, Purdue University, School of Aeronautics and Astronautics, 1995.
6. Heister, S. D., "Boundary Element Methods for Two-Fluid Free Surface Flows", To Appear, *Engineering Analysis with Boundary Elements*, 1997.
7. Hilbing, J. H., Heister, S. D., and Spangler, C. A., "A Boundary Element Method for Atomization of a Finite Liquid Jet", *Atomization and Sprays*, V 5, No. 6, pp 621-638, 1995.
8. Spangler, C. A., Hilbing, J. H., and Heister, S. D., "Nonlinear Modeling of Jet Atomization in the Wind-Induced Regime", *Physics of Fluids*, V 7, No. 5, pp 964-971, 1995.
9. D. E. Medina, On Droplets and Boundary Elements, Cornell University, FDA-89-12, 1989.
10. Prosperetti, A., "Bubble Phenomena in Sound Fields: Part Two", Part Three of Acoustic Cavitation Series, *Ultrasonics*, pp. 115-124, May, 1984.
11. Harrje, D. T. and Reardon, F. H., ed., *Liquid Propellant Rocket Combustion Instability*, NASA SP-194, 1972.
12. Yang, V. and Anderson, W.E. (eds.), *Liquid Rocket Engine Combustion Instability*, V 169, Progress in Astronautics and Aeronautics, AIAA, Washington, DC, 1995.
13. Buffum, F. G. and Williams, F. A., "The Response of a Turbulent Jet to Transverse Acoustic Fields," *Proceedings of the 1967 Heat Transfer and Fluid Mechanics Institute*, 1967, pp. 247-276.
14. Ashgriz, N., Brocklehurst, W., and Talley, D.G., "On the Mixing Mechanisms in a Pair of Impinging Jets," AIAA 95-2421, AIAA Joint Propulsion Conference, July, 1995.
15. Arbit, H.A., Tuegel, L.M., and Dodd, F.E., *Heavy Hydrocarbon Main Injector Technology Program*, Rockwell International, Rocketdyne Division Technical Report RI/RD-91-118, NASA CR-188082, 1991.
16. Pavli, A.J., "Design and Evaluation of High Performance Rocket Engine Injectors for use with Hydrocarbon Fuels", NASA TM-79319, 1979.
17. Pieper, J.L. and Walker, R.E., "LOX/Hydrocarbon Rocket Engine Analytic Design Methodology Development and Validation, Vol. 1: Executive Summary and Technical Narrative", Aerojet-General Corporation Technical Report AE512725, NASA CR-191058-V-1, 1993.

Figure Captions

1. Schematic of Impinging-Element Injector using a Like Doublet Configuration. Tangential Mode Instabilities Lead to a Periodic Crosswind on Impinging Fuel Jets.
2. Computational Domain and Boundary Conditions for Simulations of Jet Excitation from a Transverse Acoustic Wave
3. Grid Function Convergence Test Results Showing Time History of Column Aspect Ratio for $We = 0.1$, $\epsilon = 0.0064$, $\omega_g/\omega_n = 1.7$. Here, the Coarse and Fine Grids have About 1/2 and Twice the Number of Nodes, Respectively, as in the Basis Grid.
4. Motion of the Top Node ($x = 0$) for Both DRC and FRT Fuel Injector Designs ($\epsilon = 0.0064$, $We = 0.1$).
5. History of Column Aspect Ratio (AR) for Both DRC and FRT Fuel Injector Designs ($\epsilon = 0.0064$, $We = 0.1$).
6. Fuel-Jet Cross-Sections (Plotted to Scale) at Various Times in Excitation Process. Here, Times are Reported in Milliseconds Relative to the Start of the Simulation.
7. Sensitivity of Maximum Jet Deformation to Maximum Speed U_g in Acoustic Wave for Both DRC and FRT Injectors.
8. Correlation of F-1 Engine Response with Frequency Ratio, ω_g/ω_n .

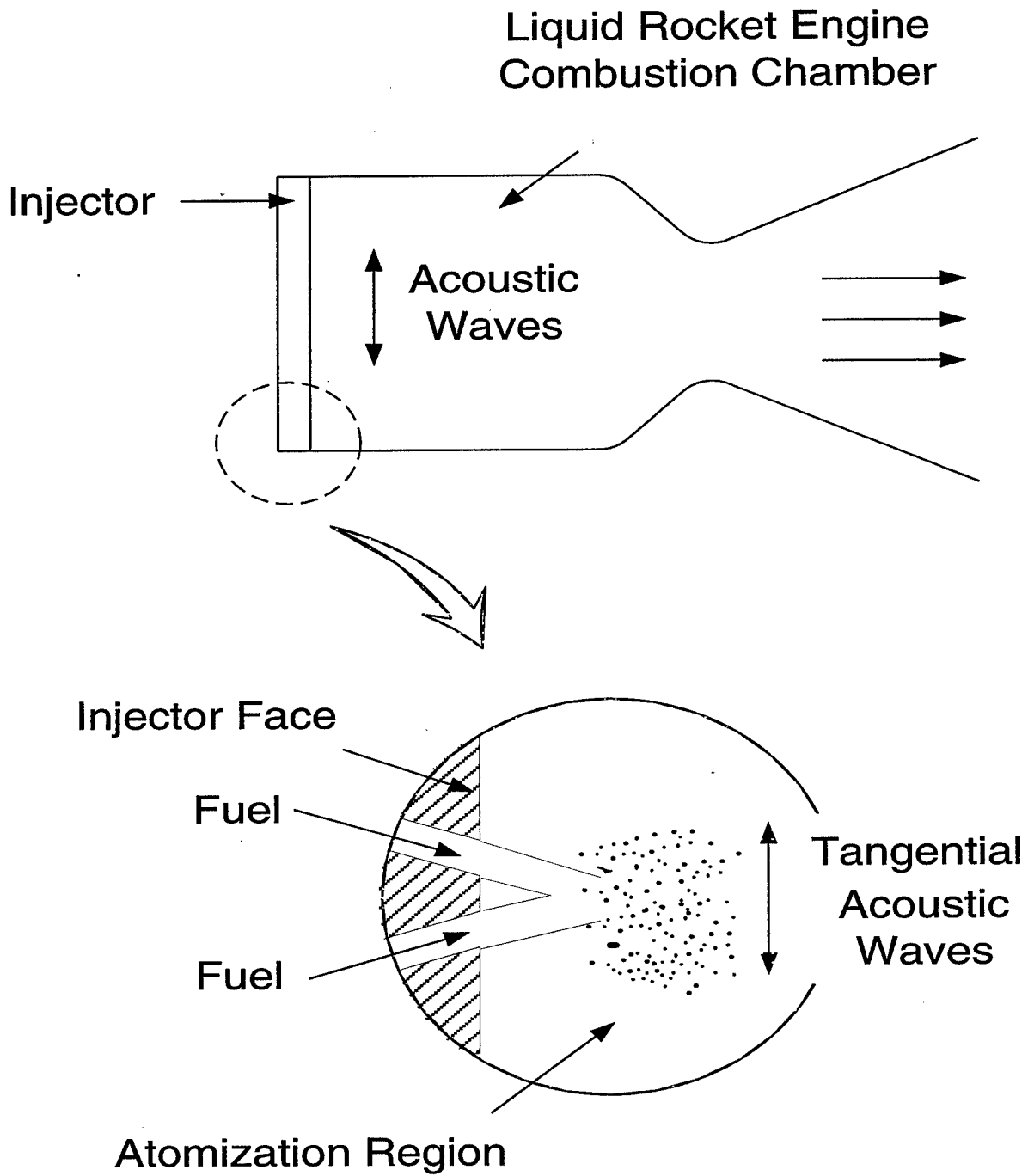


Figure 1: Schematic of Impinging-Element Injector using a Like Doublet Configuration. Tangential Mode Instabilities Lead to a Periodic Crosswind on Impinging Fuel Jets.

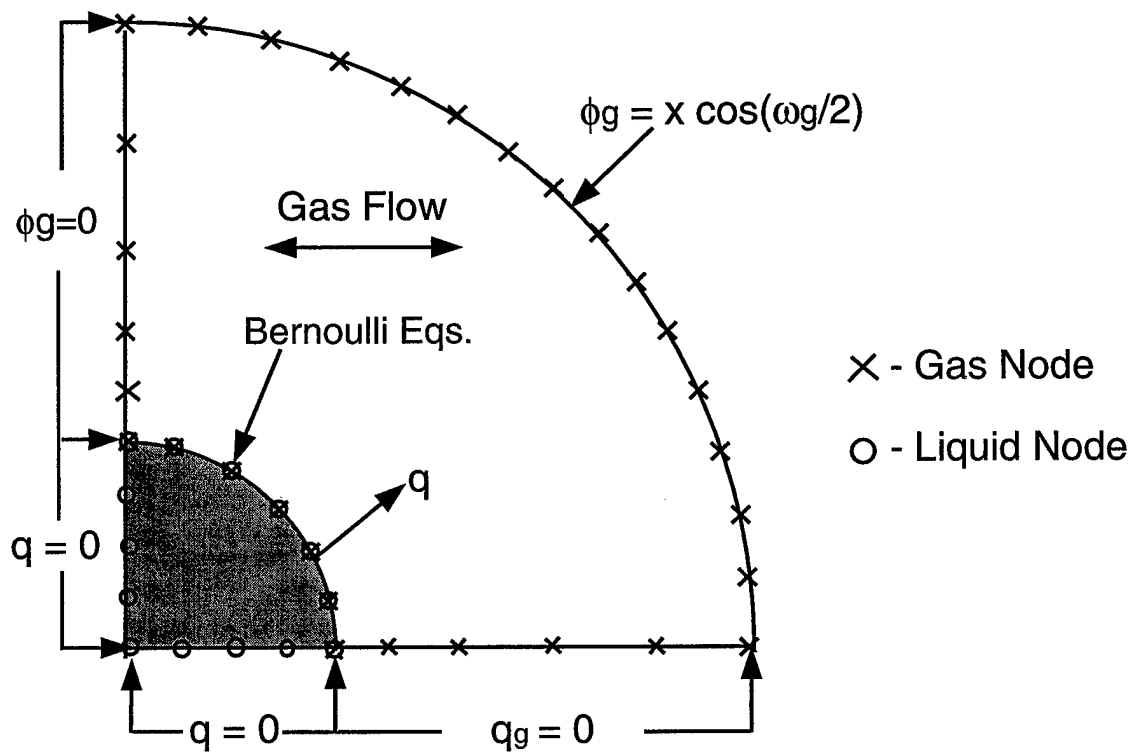


Figure 2: Computational Domain and Boundary Conditions for Simulations of Jet Excitation from a Transverse Acoustic Wave

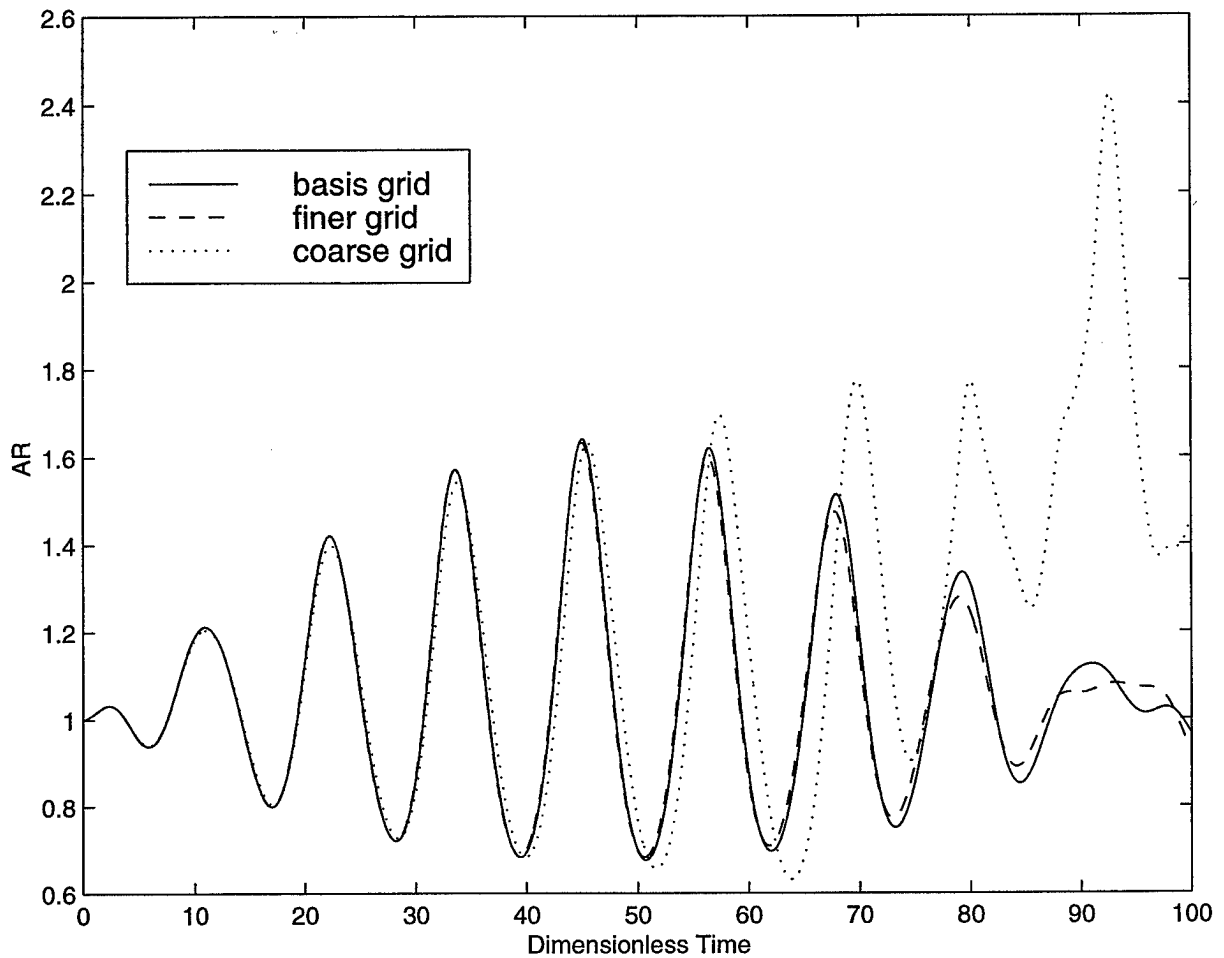


Figure 3: Grid Function Convergence Test Results Showing Time History of Column Aspect Ratio for $We = 0.1$, $\epsilon = 0.0064$, $\omega_g/\omega_n = 1.7$. Here, the Coarse and Fine Grids have About 1/2 and Twice the Number of Nodes, Respectively, as in the Basis Grid.

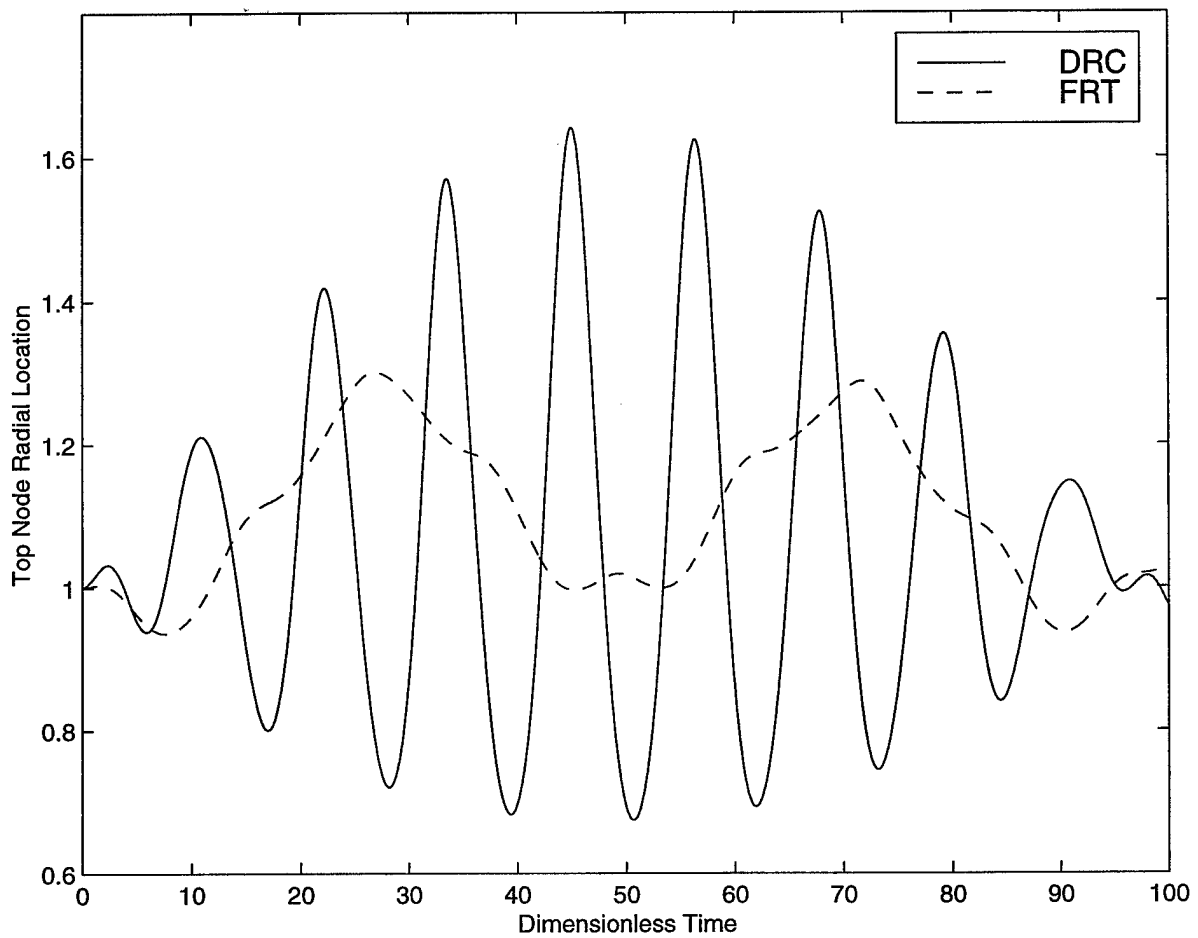


Figure 4: Motion of the Top Node ($x = 0$) for Both DRC and FRT Fuel Injector Designs ($\epsilon = 0.0064$, $We = 0.1$).

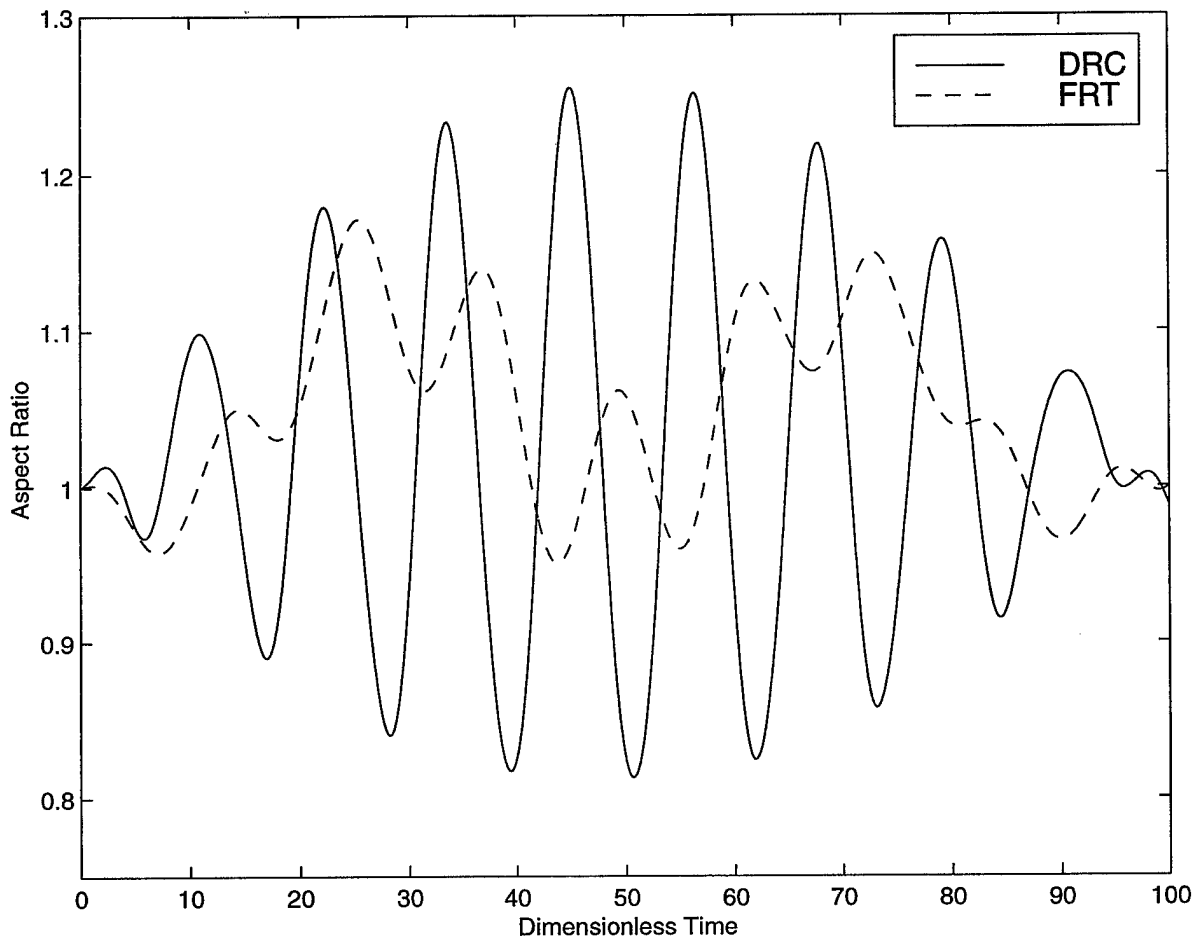


Figure 5: History of Column Aspect Ratio (AR) for Both DRC and FRT Fuel Injector Designs ($\epsilon = 0.0064, We = 0.1$).

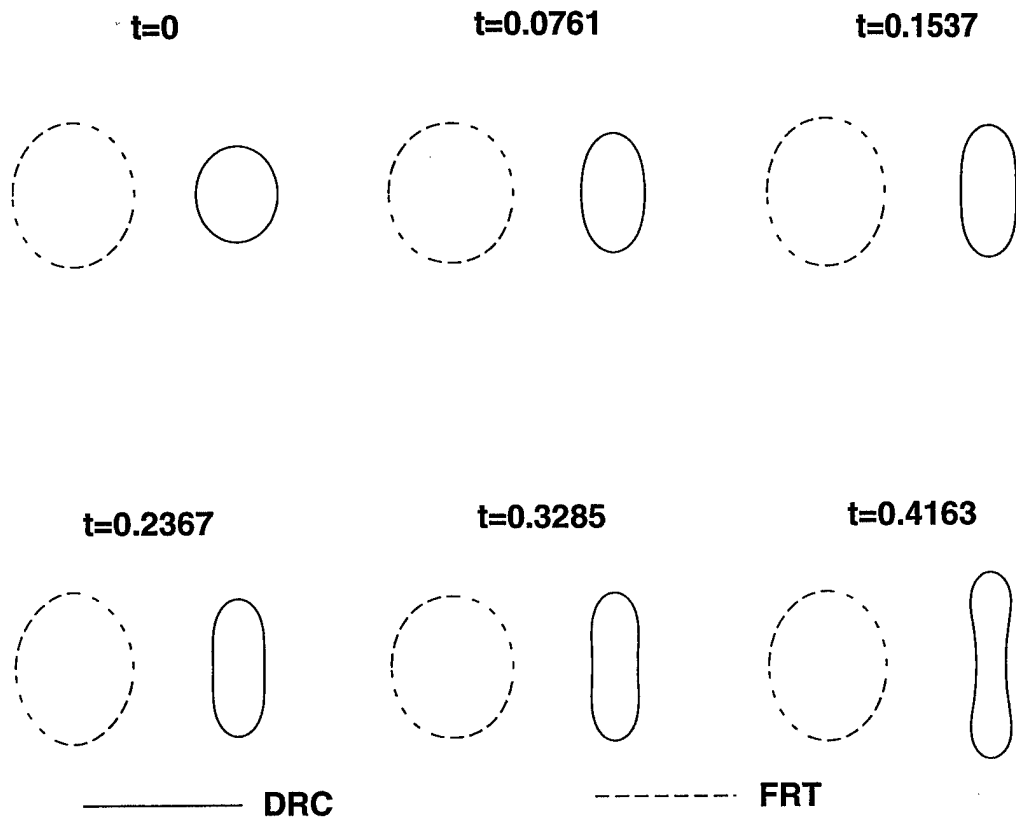


Figure 6: Fuel-Jet Cross-Sections (Plotted to Scale) at Various Times in Excitation Process. Here, Times are Reported in Milliseconds Relative to the Start of the Simulation.

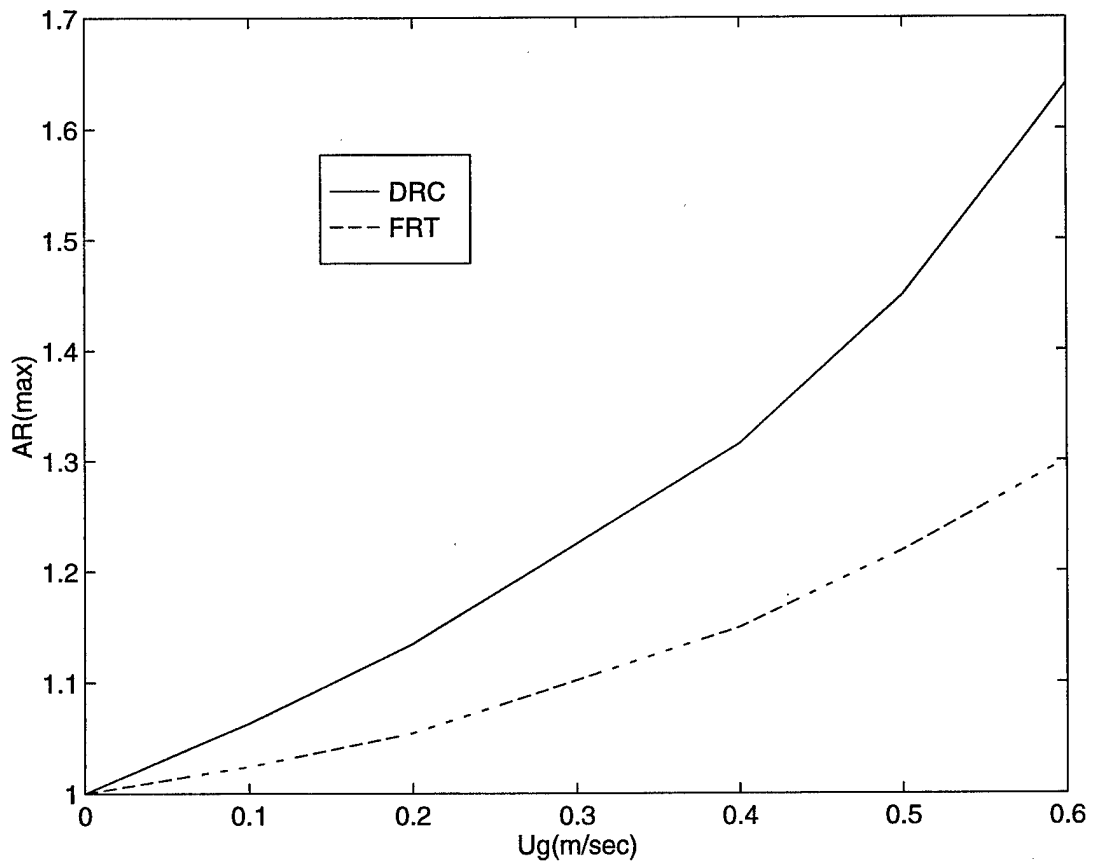


Figure 7: Sensitivity of Maximum Jet Deformation to Maximum Speed U_g in Acoustic Wave for Both DRC and FRT Injectors.

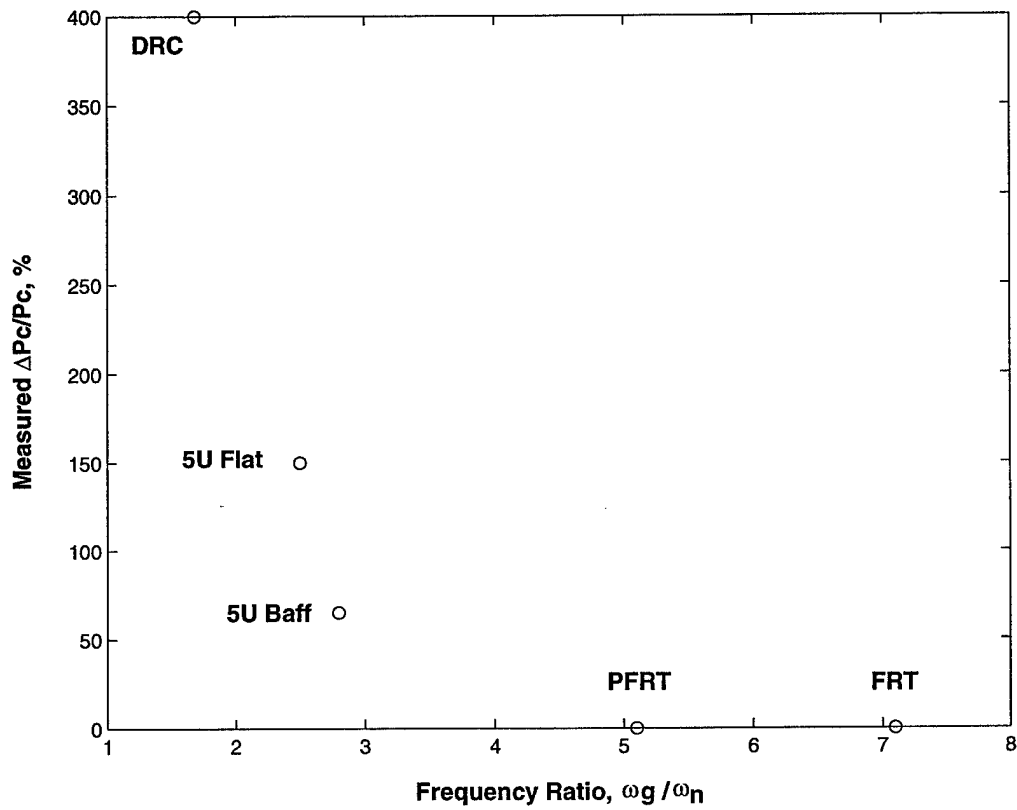


Figure 8: Correlation of F-1 Engine Response with Frequency Ratio, ω_g/ω_n .

7 Appendix C - Hybrid Rocket Injection/Combustion Tests

Wernimont, E.J., and Heister, S.D., "Combustion Experiments in a Hydrogen Peroxide/Polyethylene Hybrid Rocket with Catalytic Ignition", In Review, *Journal of Propulsion and Power*, 1998.

COMBUSTION EXPERIMENTS IN A HYDROGEN PEROXIDE/POLYETHYLENE HYBRID ROCKET WITH CATALYTIC IGNITION

E. J. Wernimont *and S. D. Heister †
Purdue University, West Lafayette, Indiana 47907

January 28, 1999

Abstract

Results from 100 tests of labscale hybrid rocket motors using hydrogen peroxide and polyethylene are presented herein. The bulk of the tests utilized 85% peroxide with low density polyethylene. A new consumable catalytic ignition device has been utilized to provide rapid, reliable ignition using *stabilized* peroxide. Regression measurements indicate that at low chamber pressures (100 psi) a classic diffusion-dominated behavior is noted with massflux exponents very near the theoretical value of 0.8. However, at higher chamber pressures tested (200 and 400 psi), radiative-dominated behavior is noted for average massfluxes varying between 0.1 and 0.3 $\text{lb}_m/(\text{in}^2 \text{ s})$. Through the optimization of aft mixing length, combustion efficiencies in excess of 95% were obtained in these tests. No significant nonacoustic or acoustic instabilities were noted in these tests; chamber pressure fluctuations were less than 3.5% zero-to-peak of mean.

Nomenclature

A_t	Throat area (in^2)
C^*	Characteristic exhaust velocity (ft/s)
dt	Differential time (sec)
D_p	Port Diameter (in)
G	Total mass flux ($\text{lb}_m/(\text{in}^2\text{s})$)
g_c	Gravitational constant ($\frac{\text{lb}_m \text{ft}}{\text{lb}_f \text{ s}^2}$)
L_f	Fuel grain length (in)
L^*	Characteristic chamber dimension (in)
M_f	Fuel mass (lb_m)
M_{ox}	Oxidizer mass (lb_m)
M_{ccb}	CCB mass (lb_m)
M_{inert}	Mass of expended inerts (lb_m)
\dot{m}_{ox}	Oxidizer mass flow rate (lb_m/s)
n	Time level
OF	Mass oxidizer/fuel mixture ratio
P_c	Head-end chamber pressure (psia)
r	Fuel regression rate (in/s)
t	Time (sec)

*Chief Propulsion Engineer, Beal Aerospace, Dallas, TX

†Associate Professor, School of Aeronautics and Astronautics. Associate Fellow, AIAA

Copyright © 1997 by the American Institute of Aeronautics and Astronautics, Inc. All rights reserved.

ρ_f Fuel density (lb_m/in^3)

Super/Subscript

$\bar{(\)}$ Burning-time averaged quantity
f Final
i Initial

Acronyms

CCB Consumable Catalytic Bed
HDPE High Density Polyethylene
HP Hydrogen Peroxide
LDPE Low Density Polyethylene
PMMA Polymethyl Methacrylate
UHMW Ultra High Molecular Weight

Introduction

In the past few years, interest in hybrid rockets has increased due to the potential for these devices to reduce costs and enhance safety in aerospace propulsion devices. A variety of applications, including launch vehicle boosters, upper stage and tactical systems have been identified as areas in which hybrid propulsion concepts are of interest.

We can trace the use of the Hydrogen Peroxide (HP)/ Polyethylene (PE) propellant combination to the mid 1950's¹⁻³. While the early tests of Moore and Berman¹ were quite successful, interest waned (most probably due to the search for higher energy propellants during this era) and essentially no published work exists for a four decade period beginning in the mid 1950's. Current requirements for lower cost, non-toxic propulsion systems have motivated a renewed interest in this storable propellant combination. Recent efforts have been undertaken in our group⁴⁻⁹, at the University of Surrey in the United Kingdom¹⁰ and the U.S. Air Force Academy¹¹.

Recent system studies^{4,5,12} point to potential benefits of HP-oxidized systems which include its high density, ease of handling, non-toxicity, and monopropellant characteristics. For example, both turbopump and pressurization systems can utilize decomposition energy and biproducts to effectively simplify engine power cycles and tank pressurization systems. In addition, the fact that HP hybrid systems tend to optimize at high mixture ratios provides a benefit in reducing the size of the expensive, high-pressure combustion chamber which contains the fuel grain. This benefit also decreases the sensitivity of these propellants to fuel slivering since the fuel provides a smaller fraction of the total propellant mass.

Polyethylene (PE) also represents a unique fuel choice in view of the fact that much of the present work focuses on the use of hydroxyl-terminated polybutadiene (HTPB) as fuel. While HTPB systems enjoy a slightly higher regression rate, which tends to reduce fuel grain complexity somewhat, this fuel is a thermoset compound which can only be produced using batch processing which necessitates substantial tooling capital investment, tooling assembly and disassembly. We suspect that the main impetus for the use of this chemical stems from the fact that most solid rocket manufacturers (many of whom also participate in hybrid rocket programs) commonly use this chemical in solid rocket propellants.

In contrast to HTPB, PE is a thermoplastic which is commonly produced via extrusion from a die in a continuous process. Hence, PE grains could be produced using this approach by simply cooling the extruded product and cutting it to the desired length. Thermoplastics also eliminate waste since the product can be remelted if a part is made incorrectly. In addition, PE has a lower cost than HTPB and is much easier to machine even though the thermochemical combustion performance of the two materials is virtually identical. For these reasons, this material represents an attractive alternative for many missions.

For these reasons, an experimental program was initiated to quantify the combustion behavior of the HP/PE hybrid propellant combination. A unique consumable catalytic ignition system was used to provide

the initiation of combustion in these studies. Factors considered in the tests described in this paper include: massflux, oxidizer/fuel (OF) mixture ratio, chamber pressure, fuel grain length (L^*), and PE formulation. The facility is briefly described in the following section, followed by a description of the ignition system, and experimental results.

Test Apparatus/Methodology

This fluid system was designed to provide reliable combustion measurements with minimal complexity and redundant safety features. To this end, a simple cartridge-loaded combustion chamber is utilized with a simple "nozzle" designed to provide the required throat area without an exit cone (simple throat plug). Figure 1 highlights the 2 inch outside diameter combustion chamber design; the catalytic ignition device is described in detail in the following section. The insulating materials used for these tests are paper phenolic. The nozzle material is a silica phenolic that provided a low erosion rate of less than 2.0 mils/sec for the configurations fired.

A schematic of plumbing and tankage associated with the test apparatus is shown in Fig. 2. This apparatus provides for safe firing of a hydrogen peroxide hybrid rocket motor by remote operation from a concrete enclosed control room. The entire fluid system utilizes materials compatible with high-concentration hydrogen peroxide such as 300-series stainless steels, glass and teflon. The high pressure HP tank is pressurized using a Nitrogen "K-bottle" with manual isolation valve, MV1, depicted in Figure 2. A second K-bottle (manual isolation valve MV4) is used to provide high pressure gas for remote actuation of stainless steel pneumatic valves denoted PV1 and PV2 in Fig. 2. During a test, the system is operated by simply opening the main oxidizer valve (PV1) until all of the HP loaded in the oxidizer tank is consumed. Gaseous nitrogen is then driven into the combustion chamber causing quenching of the remaining fuel.

As can be seen from Fig. 2, this system incorporates many safety features. Actuation of pneumatic valve PV2 provides for dumping and dilution of the HP (PV2) in the event of an emergency. During the entire test program, there were no occasions in which dumping of the HP was required. Other safety features include: a normally-open venting solenoid valve (SV2), a remotely-actuated manual vent valve (MV5), and a relief valve (RV1) on the oxidizer tank. These features were installed to allow venting of the oxidizer system in the event that undesired decomposition of the loaded HP occurs.

Instrumentation for these tests consist of ullage and chamber pressure, oxidizer turbine flow meter information as well as axial thrust measurement. This set of information (plus pre/post-test fuel grain measurements) is sufficient to determine motor operating parameters as well as information on fuel regression rate. Digital data acquisition is achieved through the use of a Pentium-based PC with a Keithley/Metrabyte analog/digital converter. This data acquisition system is used to real time display the conditions of oxidizer tank temperature (T1) and pressure (P3) during HP loading. This provides a means of determining if an emergency dumping procedure must be conducted if the loaded HP is unstable in the tank.

During a firing the data acquisition system is used to sample the motor operation parameters at 250 Hz per instrument. In each test, oxidizer flow rate is held approximately constant using the self-limiting combustion behavior of hybrid rocket motors. i.e., the rate of oxidizer injected into the combustion chamber is a direct function of the ullage-to-chamber pressure differential and the chamber pressure is also dependent on the oxidizer flowrate (for given nozzle and fuel port diameters). Assuming no throat erosion, both chamber pressure and oxidizer flow rate may be held constant by maintaining a constant ullage pressure. Constant ullage pressure is achieved by regulated nitrogen pressurant gas. This technique is used for all the tests presented in this paper.

The test program was formulated to maximize the amount of information available to actually design a HP/PE hybrid. For this reason, many different parameters were studied, none of which were studied in tremendous detail. Most parameters were investigated across a range of total mass port flux levels allowing determination of fuel regression rate influence. The entire test program involved firing eleven different series of motors, with each series dedicated to examination of a specific parameter. A total of 100 firings were conducted in association with these test series which are summarized in Table 1. Acronyms in Table 1 are defined in the nomenclature. The following sections will discuss results obtained from the bulk of these tests. Testing accomplished using a radial-flow geometry (test series C in Table 1) are reported in Ref. 13.

Table 1: Test Series Summary

Series	Purpose	Number of Motors	Test Parameters
A	System Verification	12	$\bar{P}_c \sim 100$ psia \bar{G} 0.25 to 0.35 lb _m /(in ² - s) 85% HP Interlox, HDPE
B	Broader Flux	12	\bar{G} 0.15 to 0.35 lb _m /(in ² - s) Three at 80% HP Interlox
C	Radial Flow Motor	20	Proof of Concept 8 Ignition Tests
D	Polyethylene Types	11	LDPE, UHMW
E	Higher Mass Flux, P_c	8	Flight Weight, LDPE Proof of Combustion
F	New HP Vendor	5	Air Liquide 85% HP
G	Increase P_c	5	$\bar{P}_c \sim 200$ psia
H	Lengthen Aft Combustion	4	Increase by 2, 4 Inches
I	Action Time Study	4	Two at 6, 9 Seconds Each
J	Increase P_c	5	$\bar{P}_c \sim 400$ psia
M	Increase Mass Flux	10	G 0.35 to 1.0 lb _m /(in ² - s)
Y	Ignition Behavior	4	Visual Observations, PMMA Fuel

Consumable Ignition Device

Probably the greatest challenge in creating a workable hybrid propellant combination lies in the development of an ignition concept which provides a rapid and reproducible rise in chamber pressure and thrust. In the past, secondary injection of pyrofluoric fluids, electric ignition sources, torches, and catalytic ignition systems have been used in hybrid rockets. With the exception of the catalytic system, all these concepts require additional hardware and/or fluids to support ignition of the motor. For this reason, the catalytic concept was pursued through the use of a consumable catalytic bed (CCB). While catalytic devices such as silver screens and other materials treated with catalytic material have been used to decompose peroxide in the past¹⁴, the present concept¹⁵ provides several advantages over these techniques:

- The CCB concept supports operation with *stabilized* HP (successful tests with stabilizer levels as high as 50 ppm). Most of the previous systems could not operate with stabilizers (primarily stannate and phosphate compounds) in the fluid because these materials would reduce the catalytic activity of the bed material. Use of stabilized fluid throughout this test program has been viewed as a substantial safety enhancement.
- The CCB provides an energetic ignition system with no inert parts, thereby maximizing the propellant mass fraction of the propulsion system.
- Since the device requires no inert hardware (or other fluids/gases) it also represents a minimum cost ignition system.

The CCB is inserted into a pocket which was machined into the forward end of the fuel grain as noted schematically in Fig. 1. No special ignition sequence was utilized in any of the testing, the engine was literally "slam started" by opening valve PV2 (see Fig. 2) which provides maximum HP flow. As HP passes through passages in the CCB it is decomposed. If the HP is at sufficient concentration, the decomposition products are at a temperature such that autoignition of the PE occurs. As the HP flow continues, the CCB

is consumed. If the CCB is sized properly, there will be enough energy in the combusting fuel grain to support thermal decomposition of the HP injected after CCB consumption; i.e. the device operates for only a small fraction of a firing.

Figure 3 highlights a group of typical ignition transients obtained with the use of 85% HP in the design. This collection shows that the CCB is repeatable and produces rapid ignition transients. The peaks at approximately 30 msec represent a pressure overshoot due to increased oxidizer mass flow when the oxidizer valve is first opened. Because there is no cavitating venturi in the fluid system, the oxidizer mass flow is governed strictly by pressure differential. Consequently, initial fluid flow is greatest for the first 20 msec before the chamber pressure has a chance to climb to its steady state value. As can be seen from the figure, steady-state combustion has been achieved in 50 msec.

To aid in the understanding of the rate of consumption of the device, a series of four motors (Y-series described in following section) were fired using transparent acrylic, (PMMA) fuel grains. A typical chamber pressure history from one of these firings (test Y1) is shown in Fig. 4. The time window in the figure captures the interval from ignition to the beginning of tailoff such that the ignition event occurs at roughly 3.3 sec on this time scale. There is a noticeable decrease in chamber pressure at roughly 5.5 sec (2.1 sec after ignition) which is observed in most firings in our test program. This behavior was attributed to the complete combustion of the CCB. A similar behavior was noted on other PMMA firings and rapid decreases in chamber pressure were well correlated with consumption of the CCB.

To investigate this assertion, still photographs were taken during this firing. The photos were taken with the auto-iris set on the camera so intensity levels are not necessarily representative of flame temperature. A sequence of four photos is summarized in Fig. 5. In this figure, the CCB is on the right and flow is from right to left. At ignition ($t=3.3$ sec), the fuel port is already luminous indicating reaction within the CCB. The second image, taken just prior to the chamber pressure decrease, shows complete consumption of a small portion of the CCB at one circumferential location. In the next frame available from the camera ($t=5.5$ sec) the entire aft portion of the CCB has been consumed or expelled from the motor. This event correlates well with the decrease in chamber pressure noted in Fig. 4. The final image, taken just prior to total oxidizer consumption ($t=11.5$ sec) shows a small dark region at the head-end of the grain. Since postfire inspection revealed that the entire CCB had been consumed (or expelled), this dark region corresponds to the zone in which HP decomposition occurs. Postfire fuel samples are in agreement with this theory; negligible regression is observed in this region.

One can also note an asymmetric fuel regression pattern on the last image ($t=11.5$ sec); maximum fuel regression occurs at the top of the CCB pocket in a region which was the last area to be exposed a result of local CCB consumption. This asymmetric behavior was noted in all four PMMA firings and was attributed to nonuniformities in the spray pattern emanating from the injector¹⁶. The higher flow which caused local CCB consumption at $t=5.45$ sec. could provide local quenching (or decreased combustion), thereby explaining the observed behavior. While some asymmetries were noted in firings using PE grains, they were generally restricted to the region which housed the CCB.

Test Results

As indicated in Table 1, a broad range of tests were conducted over the twelve test series. Unfortunately, we were unable to maintain a consistent HP vendor over the three year study. While some differences in fluid were noted¹⁶, they were generally minor. In addition, we experimented with several different throat materials before arriving at a suitable option, which was used throughout test series D-Y. Early efforts were aimed at optimizing fuel grain length so as to obtain OF ratios near the 7.5 value which tends to maximize specific impulse for these propellants. Many of the later tests actually achieved fairly low mixture ratios (in the 5-6 range) due to the fact that fuel regression rates exceeded our estimates. A complete tabulated list of all test conditions can be found in Ref. 16; we will not include all these data here in the interest of brevity.

Substantial efforts were expended in quantifying combustion behavior for various PE formulations including Low Density PE (LDPE), High Density PE (HDPE), and ultra-high molecular weight (UHMW) materials¹⁶. Discussion of this area is planned for a future work; the bulk of the efforts to be described herein relate to the effects of chamber pressure, fuel grain internal diameter and length, aft combustion length and OF ratio on combustion performance.

Because the CCB device contributed a non-negligible amount of mass and energy during our test burns,

which typically varied between 5 and 20 seconds, we were forced to improve upon the data reduction methodology which had typically been used by hybrid rocket experimentalists. Average regression rates and port total flux levels from a given test firing are obtained from an integral reconstruction of the entire chamber pressure history with the CCB and inerts flows taken into account. The approach begins with the determination of average characteristic velocity (\bar{C}^*) and oxidizer/fuel mass ratio ($\bar{O}F$) for a given test:

$$\bar{C}^* = \frac{\int_{t_i}^{t_f} P_c(t) A_t(t) g_c dt}{M_{ox} + M_f + M_{ccb} + M_{inert}} \quad (1)$$

and

$$\bar{O}F = \frac{M_{ox}}{M_{fuel} + M_{ccb} + M_{inert}} \quad (2)$$

The expended masses (see Nomenclature for definitions) can all be measured directly with the use of pre- and postfire measurements. Instantaneous values (time level n) of total mass flux (from its definition) and fuel regression rate (assuming a steady-state balance of incoming and exiting mass flows) may then be calculated as:

$$G_n(t) = \frac{\dot{m}_{ox_n} + \bar{m}_{ccb_n} + r_{n-1} L_f \pi (2r_{n-1} dt + D_{p_{n-1}}) \rho_f}{\pi (2r_{n-1} dt + D_{p_{n-1}})^2 / 4} \quad (3)$$

$$r_n(t) = \frac{P_{c_n} A_{t_n} g_c / \bar{C}^* - \dot{m}_{ox_n} - \bar{m}_{ccb_n} - \bar{m}_{inert_n}}{L_f \pi (2r_{n-1} dt + D_{p_{n-1}}) \rho_f} \quad (4)$$

Using this process, the entire regression rate and mass flux histories may be reconstructed from the measured time-dependent data. Action time averages are computed via direct integration:

$$\bar{r} = \int_{t_i}^{t_f} r_n(t) dt / \int_{t_i}^{t_f} dt \quad (5)$$

$$\bar{G} = \int_{t_i}^{t_f} G_n(t) dt / \int_{t_i}^{t_f} dt \quad (6)$$

Error analyses indicate that for our apparatus, this approach is superior to more classical "end-point" based techniques¹⁷ which compute average regression rate and port total mass flux using just pre- and postfire port diameters. For the tests presented herein, the bias errors in regression rate and flux are estimated to be 1.9 and 1.1% respectively. A complete description of the methodology, which will be used throughout this work, is provided in Ref. 17.

Reliable ignition and combustion was demonstrated over a range of initial oxidizer fluxes $0.1 < G_{ox} < 1.2 \text{ lb}_m/(\text{in}^2 \text{ s})$ and chamber pressures $100 < P_c < 400 \text{ psia}$ during the testing with 85% HP. A few tests were conducted with 80% HP, but reliable ignition and combustion could not be achieved using the injector and CCB design implemented in these tests. We believe that one could design a device to operate at these lower concentrations with an improved injector (with smaller droplet sizes) and CCB designs. Our injector produced droplets which were quite large, a 350 micron volumetric mean diameter is reported by the manufacturer. Limited information¹⁶ suggests that ignition and combustion at concentrations lower than 80% would be very difficult for PE; at these concentrations most of the decomposition energy goes into vaporizing the water in the aqueous HP. Here we should note that concentrations below 67% have insufficient decomposition energy to vaporize water within the mixture.

Typical chamber pressure histories obtained during the test program are shown in Fig. 6. Overall, the combustion obtained was very smooth as evidenced by the low amount of noise in the pressure signals. Typical unsteadiness in the pressure signals was of the order of 1-2% (zero-to-peak) of the mean pressure in this test program. Sharp tailoffs were always observed in the testing; action times were determined using a bisector technique¹⁷ commonly used in solid rocket data reduction. The spike in the motor F4 and H3 traces in the interval $1 < t < 2$ seconds is attributed to ejection of small portions of the CCB through the nozzle. In the M1 pressure trace, a slight increase in P_c is observed after the main ignition event. This behavior may be attributed to increased oxidizer flow rate due to a change in injector discharge coefficient¹⁶.

Table 2: Summary of LDPE/85% HP Fuel Regression Flux Correlations

Correlation	\bar{P}_c	\bar{G}
$0.040G^{0.78}$ ips	100 psia	0.1 - 0.3 $\text{lb}_m/(\text{in}^2 - \text{s})$
$0.035G^{0.52}$ ips	200 psia	0.1 - 0.3 $\text{lb}_m/(\text{in}^2 - \text{s})$
$0.041G^{0.49}$ ips	400 psia	0.2 - 0.7 $\text{lb}_m/(\text{in}^2 - \text{s})$

Regression Rate Behavior

While there were test series dedicated to assessing the influence of PE type on fuel regression and combustion, the bulk of the measurements were obtained using Low Density PE (LDPE) fuel. A compilation of these measurements is provided in Fig. 7 which highlights dependence of regression rate on *both* flux level and chamber pressure. While the low pressure (100 psi) data appear to behave a classical regression law ($r \propto G^n$) consistent with diffusion-dominated behavior, the higher pressure results show a distinct insensitivity to port total mass flux (G) in the range $0.1 < G < 0.3 \text{ lb}_m/(\text{in}^2 \text{ s})$. In this lower flux region, regression rates at the higher pressures tested (200 and 400 psia) are as much as 75% greater than those at low pressures. The data are consistent with a radiation-based regression law which has been theorized, but infrequently observed for low massflux conditions.

In fact, this behavior is ideal since regression rates would no longer be influenced by changes in port geometry (either shape or size). For the booster application, design studies⁵ indicate an optimal massflux level of about $0.4 \text{ lb}_m/(\text{in}^2 \text{ s})$ assuming a classical regression law, $r \propto G^{0.8}$. Presumably, designers could make use of this desirable behavior (flux insensitivity) for other applications as well.

To compare the data from this test program with that of previous researchers, we performed correlations assuming a classical, massflux-dominated regression behavior. While this approach is not warranted for the higher pressure results, it does permit gross comparisons with results of other researchers who made similar assumptions. The resulting correlations are presented in Table 2. Note that for the low pressure data the exponent of 0.78 is in close agreement with theory assuming a diffusion-dominated behavior. The exponent is reduced at the higher pressures due to the radiative-dominated behavior.

The correlations from Table 2 are compared with those obtained by other researchers in Fig. 8. Previous researchers using hydrogen peroxide^{1-3,18,19} had also noted a

Figure 9 shows combustion efficiency versus the length of the aft combustion chamber. As can be seen from the figure, there appears to be significant efficiency gains from even minor length increases. There are only two motors fired with a 6 inch length since it is thought sufficient gains are made firing with a 4 inch long aft combustion chamber. Note that efficiency values of above 95% are routinely attained in this device with minor changes in combustor geometry.

Figure 10 shows the combustion efficiency versus the characteristic chamber length, L^* , for the motors tested. For our purposes L^* is calculated as the combustor volume aft of the fuel grain and forward of the throat divided by the throat area. This parameter is often used in the liquids industry to design a motor for acceptable (>95%) combustion efficiency. This parameter is specific to propellant combination, but for comparison to liquid oxygen and ethyl alcohol L^* values are between 40 and 120 inches²¹. This figure shows that efficiency gains are derived from increased L^* as is generally the case. This figure suggests that L^* values as low as 40 inches may provide sufficient aft combustion volume for efficiencies above 90%.

Figure 11 shows the effect of measured average chamber pressure on combustion efficiency. This figure also tends to suggest that combustion efficiency gains are obtained as a result of increases in chamber pressure and that values of at least 200 psi are required to obtain acceptable efficiencies (at least for the aft combustion lengths tested). One could speculate that the 100 psi firings may have required a larger mixing region to obtain a higher efficiency; this theory was not explored in our testing. Since most applications demand chamber pressures in excess of 100 psi, this issue should not adversely effect a given design.

Combustion Stability Behavior

As noted in the discussion of Fig. 6, there were no notable combustion instabilities in this test program. Recent theoretical efforts²² suggest that thermal lags in the fuel can account for the low-frequency (1-100 Hz) oscillations which have been observed in numerous tests which have used either liquid or gaseous oxygen as the oxidizer. In contrast to liquid oxygen systems which tend to optimize at OF values near 2.5, the HP/PE system optimizes at much higher OF ratio (typically around 7.5). In this case, the mass and energy addition from the fuel is much less than in oxygen oxidized systems, thereby reducing the overall amplitude achievable. This factor may explain our distinct lack of instabilities. However, we should note that all testing was performed on a fairly small scale apparatus (2 inch diameter fuel grain) and additional larger scale work will be required to confirm this suspicion.

Overall, the level of combustion oscillations was observed to be below 3.5% zero-to-peak of mean throughout the testing program. Figure 12 shows a typical waterfall plot from motor F4. A slight tendency for non-acoustic combustion oscillations up to a frequency of approximately 70 Hz is noted. Comparison with behavior in other motors suggests that the higher frequency (acoustic) portion may account for roughly 1.5% zero-to-peak chamber pressure response. Although the motor F4 waterfall plot shows no preferred waveform for this propellant combination, later motors do have preferred oscillatory waveforms. As an example Figure 13 shows the waterfall plot for motor G3 which has a preferred waveform at roughly 20 to 35 Hz with an amplitude of around 0.75 psid zero-to-peak. Three other motors (G4, I4 and M3) exhibited similar responses to that of motor G3. Other motors (J3, G5, and J5) exhibited a preferred waveform at roughly 65 to 80 Hz with an amplitude of around 0.5 psid zero-to-peak.

Conclusions

This paper summarizes combustion measurements from testing of the hydrogen peroxide (HP)/polyethylene (PE) hybrid rocket propellant combination. The bulk of the tests utilized 85% HP with low density PE (LDPE), but some data are reported for other types of PE. A new consumable catalytic bed (CCB) design has been used to provide rapid, reproducible ignition using *stabilized* HP. Once the CCB is consumed, the HP undergoes thermal decomposition as a result of exposure to combustion gases emanating from the ignited fuel grain. The device provides a simple, low cost (and weight) alternative for ignition of hybrid rockets.

Measured regression rates indicate a classic diffusion-dominated behavior at chamber pressures of 100 psi, with flux exponents very near the theoretical value of 0.8. However, at higher pressures, radiation-dominated behavior in which regression appears to be insensitive to changes in flux, is noted for massflux levels between 0.1 and 0.3 $\text{lb}_m/(\text{in}^2 \text{ s})$. This behavior can lead to pressure-related amplifications of regression rate as high as 75% when compared to the low pressure (100 psi) behavior. Results are shown to be comparable to those obtained from other researchers using HP as oxidizer with various other fuels.

High combustion efficiencies (> 95%) were obtained at the higher chamber pressure (200 and 400 psi) conditions by using aft mixing lengths equivalent to about two fuel grain diameters (4 inches). These lengths are consistent with L^* values (based on the chamber volume aft of the fuel grain) of about 60 inches. Smooth combustion was observed in all testing, with typical chamber pressure fluctuations in the range of 1-2% (zero-to-peak) of the mean. We speculate that the high mixture ratio (5-8) operation of this propellant combination plays a role in reducing the amount of energy available to drive nonacoustic instabilities. Some minor activity is noted in the range of 20-80 Hz for some of the 100 motors which were tested in these efforts.

References

- [1] Moore, George E., Berman, Kurt, "Solid-Liquid Rocket Propellant System", *Jet Propulsion*, Nov. 1965, pp 965-968.
- [2] Moore, G. E., Driscoll, D. H., and Berman, K., "A Hybrid Rocket Propellant System: 90-Percent Hydrogen Peroxide/Solid Fuel; Part II," General Electric, Schenectady, N. Y., Technical Report R53A0509, July 1954.

- [3] Moore, G. E., Driscoll, D. H., and Berman, K., "A Hybrid Rocket Propellant System: 90-Percent Hydrogen Peroxide/Solid Fuel; Part I, General Considerations," General Electric, Schenectady, N. Y., Technical Report R52A0516, July 1954.
- [4] Ventura, M. and Heister, S. D., "Hydrogen Peroxide as an Alternative Oxidizer for a Hybrid Rocket Strap-on Booster", *Journal of Propulsion and Power*, V. 11, No. 3, pp. 562-565, 1995.
- [5] Vonderwell, D. J., Murray, I. F., and Heister, S. D., "Optimization of Hybrid Rocket Engine Fuel Grain Design", *Journal of Spacecraft and Rockets*, V 32, No. 6, pp 964-969, 1995.
- [6] Wernimont E. J., Meyer S. E., "Hydrogen Peroxide Hybrid Rocket Engine Performance Investigation", AIAA 94-3147, 30th Joint AIAA Propulsion Conference, Indianapolis, IN, June 27-29, 1994.
- [7] Wernimont, E. J. and Heister, S. D., "Performance Characterization of Hybrid Rockets Using Hydrogen Peroxide Oxidizer," AIAA Paper 95-3084, 31st AIAA/ASME/SAE/ASEE Joint Propulsion Conference, San Diego, CA, July, 1995.
- [8] Wernimont, E. J. and Heister, S. D., "Progress in Hydrogen Peroxide Oxidized Hybrid Rocket Experiments," AIAA Paper 96-2696, 32nd AIAA/ASME/SAE/ASEE Joint Propulsion Conference, Lake Buena Vista, FL, July, 1996.
- [9] Wernimont, E. J., and Heister, S. D., "Experimental Study of Chamber Pressure Effects in a Hydrogen Peroxide-Oxidized Hybrid Rocket", AIAA 97-2801, 33rd AIAA Joint Propulsion Conference, 1997.
- [10] Sellers, J. J., "Investigations into Hybrid Rockets and Other Cost Effective Propulsion Options for Small Satellites", Ph.D. Dissertation, University of Surrey, 1996.
- [11] Humble, R. and Sandfry, R., "HYSTAR Hybrid Rocket Program at the United States Air Force Academy", AIAA 97-2797, 33rd AIAA Joint Propulsion Conference, 1997.
- [12] Clapp, M.B. and Hunter, M.W., "A Single Stage to Orbit Rocket with Non-Cryogenic Propellants", AIAA 93-2285, 29th AIAA Joint Propulsion Conference, 1993.
- [13] Caravella, J. R., Heister, S. D., and Wernimont, E. J., "Characterization of Fuel Regression in a Radial Flow Hybrid Rocket", *Journal of Propulsion and Power*, V14, 1, pp 51-56, 1998.
- [14] Rusek, J. J., "New Decomposition Catalysts and Characterization Techniques for Rocket-Grade Hydrogen Peroxide", *Journal of Propulsion and Power*, V 12, No. 3, 1996.
- [15] Wernimont, E. J., and Meyer, S. E. and Ventura, M. C., "A Hybrid Motor System with a Consumable Catalytic Bed, A Composition of the Catalytic Bed and A Method of Use", U.S. Patent Application No. 08/623,937, Filed March 28, 1996.
- [16] Wernimont, E.J., "Experimental Study of Combustion in Hydrogen Peroxide Hybrid Rockets", Ph.D. Thesis, Purdue University, 1997.
- [17] Wernimont, E.J., and Heister, S.D., "A Reconstruction Technique for Reducing Hybrid Rocket Combustion Test Data", *Journal of Propulsion and Power*, In Review, 1997.
- [18] Pugibet, M. and Moutet, H., "On the Use of Hydrogen Peroxide as Oxidizer in Hybrid Systems," *La Recherche Aérospatiale*, No. 132, No. 132, 1969, pp. 15-31. Translated From French by NASA as TTF-13034, May, 1970.
- [19] Osmon, R. V., "An Experimental Investigation of a Lithium Aluminum Hydride-Hydrogen Peroxide Hybrid Rocket," *Aerospace Chemical Engineering*, Vol. 62, No. 61, No. 61, 1966, pp. 92-102.
- [20] Gordon, S. and McBride, B. J., "Computer Program for Calculation of Complex Chemical Equilibrium Compositions, Rocket Performance, Incident and Reflected Shocks; and Chapman-Jouguet Detonations," NASA SP-273, NASA Lewis Research Center, 1971.

[21] Sutton, G. P., *Rocket Propulsion Elements, 6th Edition*, John Wiley and Sons, 1992.

[22] Karabeyoglu, M. and Altman, D., "The Transient Behavior of Hybrid Rockets", AIAA 97-2937, 33rd AIAA Propulsion Conference, 1997.

Figure Captions

1. Cross Sectional View of the Combustion Chamber
2. Test Facility Schematic
3. Typical Motor Ignition Traces (from D-Series Testing)
4. Motor Y1 Chamber Pressure History
5. Still Photographs of Motor Y1 showing CCB consumption. Here, the CCB is located on the right hand side of the image and flow is from right to left. From top to bottom, images are for $t = 3.3, 5.45, 5.5,$ and 11.5 sec
6. Measured Chamber Pressure Histories for Motors F4, H3, and M1 at Average Pressures of Roughly 100, 200, and 400 psi, Respectively
7. LDPE Fuel Regression Data Showing Effect of Pressure
8. Comparison of Previous HP Investigators Regression Rate Measurements to Present Study
9. Effect of Aft Combustion Length on C^* Efficiency with Inerts
10. Effect of L^* on C^* Efficiency with Inerts
11. Effect of Chamber Pressure on C^* Efficiency with Inerts
12. Waterfall Plot of Chamber Pressure from Motor F4
13. Waterfall Plot of Chamber Pressure from Motor G3

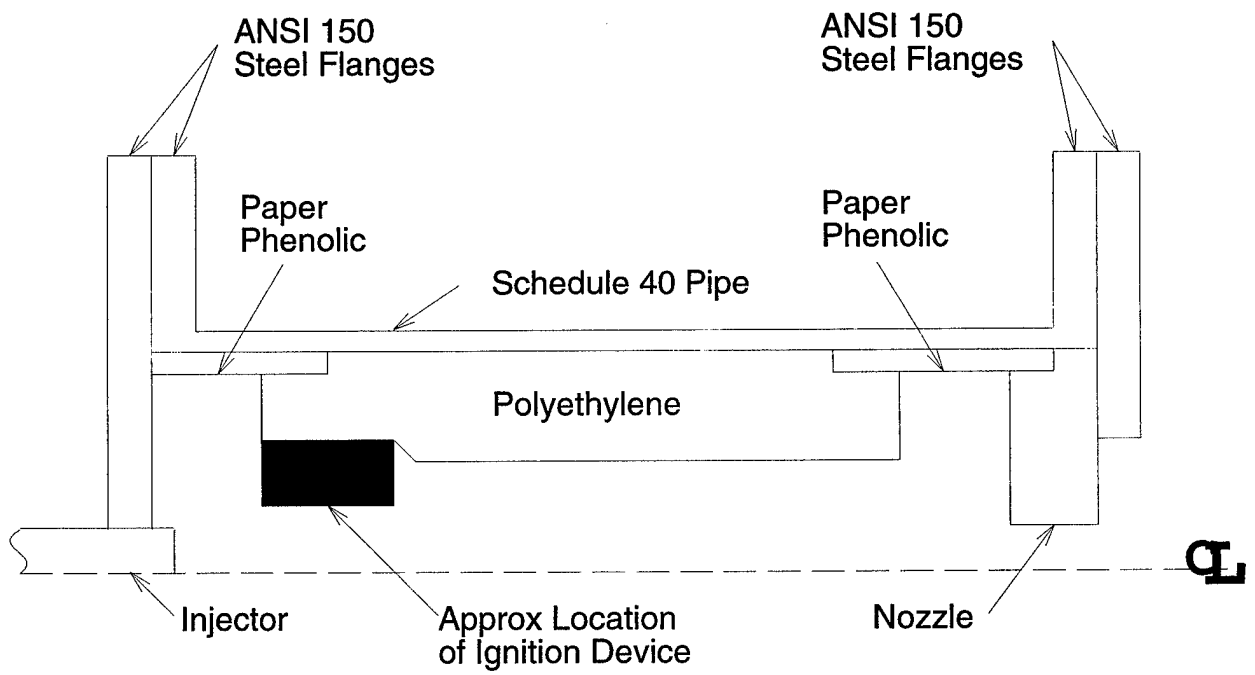


Figure 1: Cross Sectional View of the Combustion Chamber

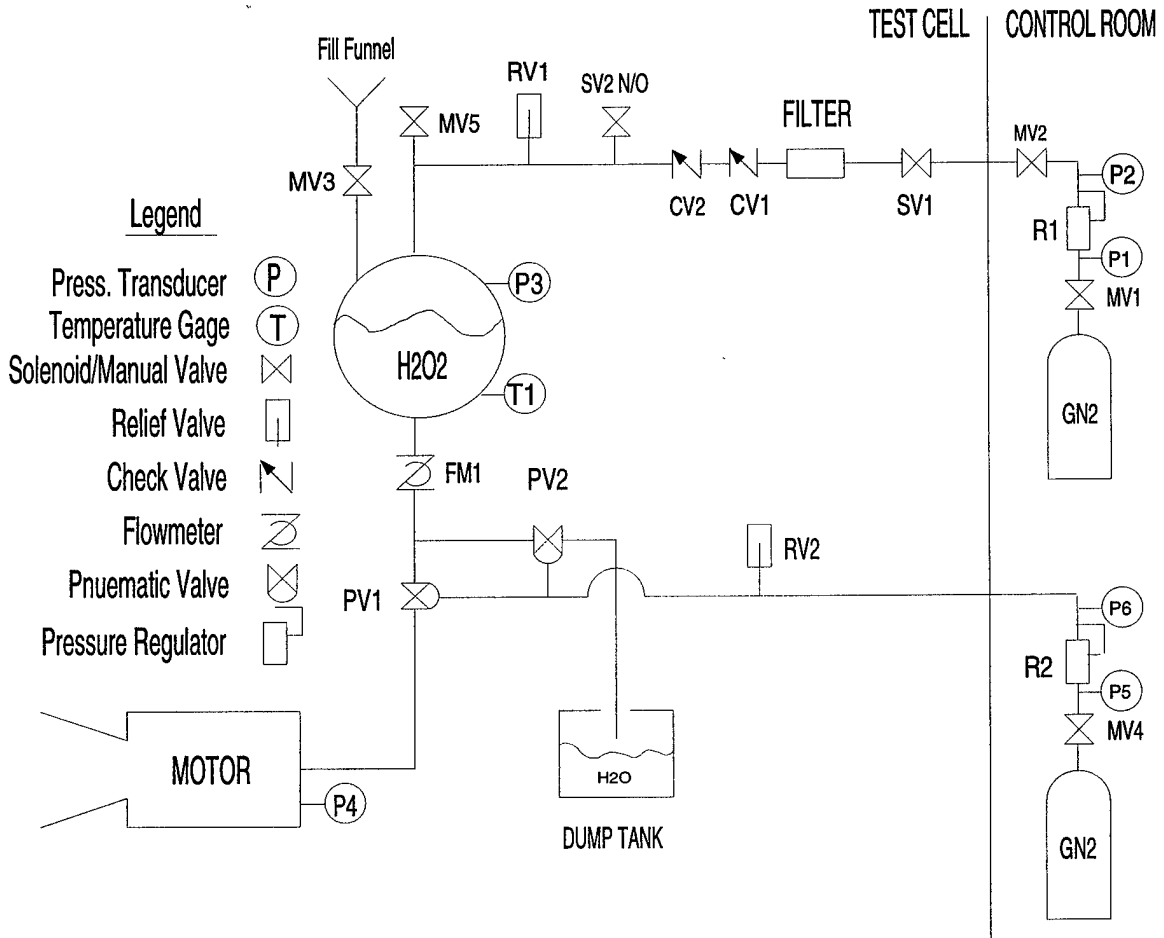


Figure 2: Test Facility Schematic

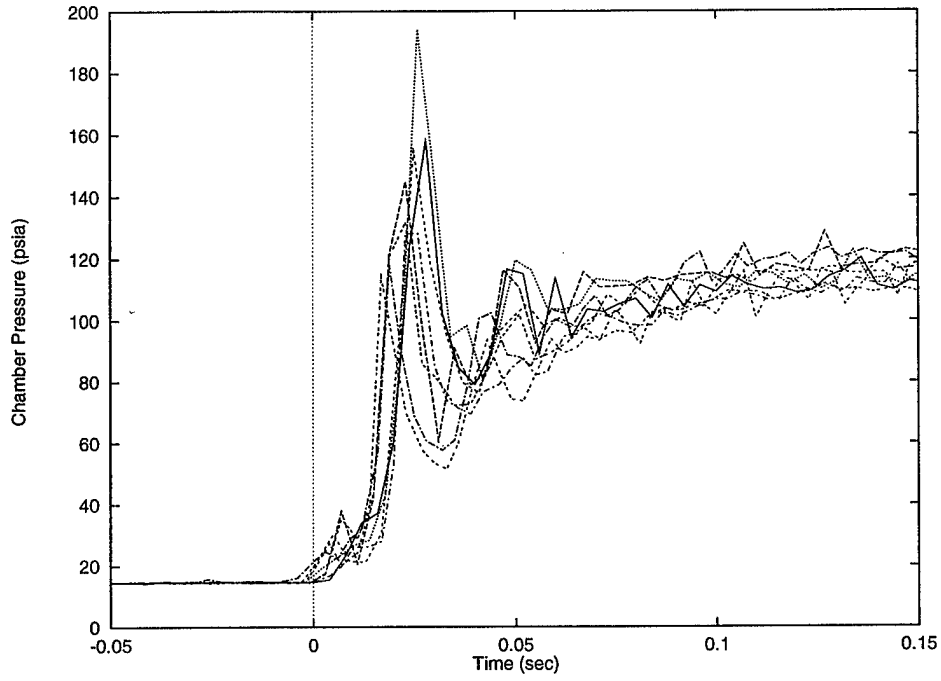


Figure 3: Typical Motor Ignition Traces (from D-Series Testing)

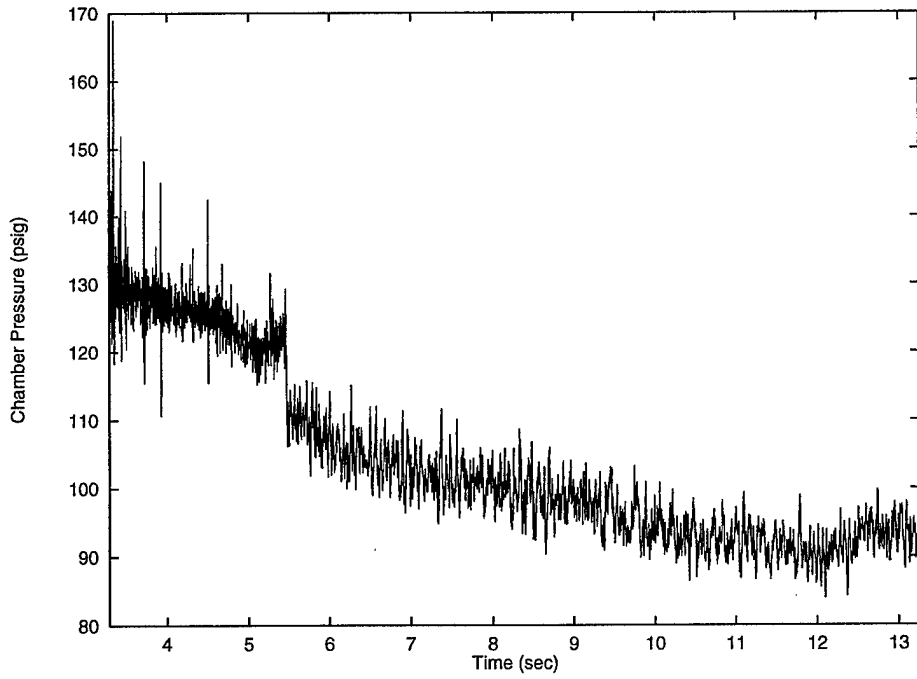


Figure 4: Motor Y1 Chamber Pressure History

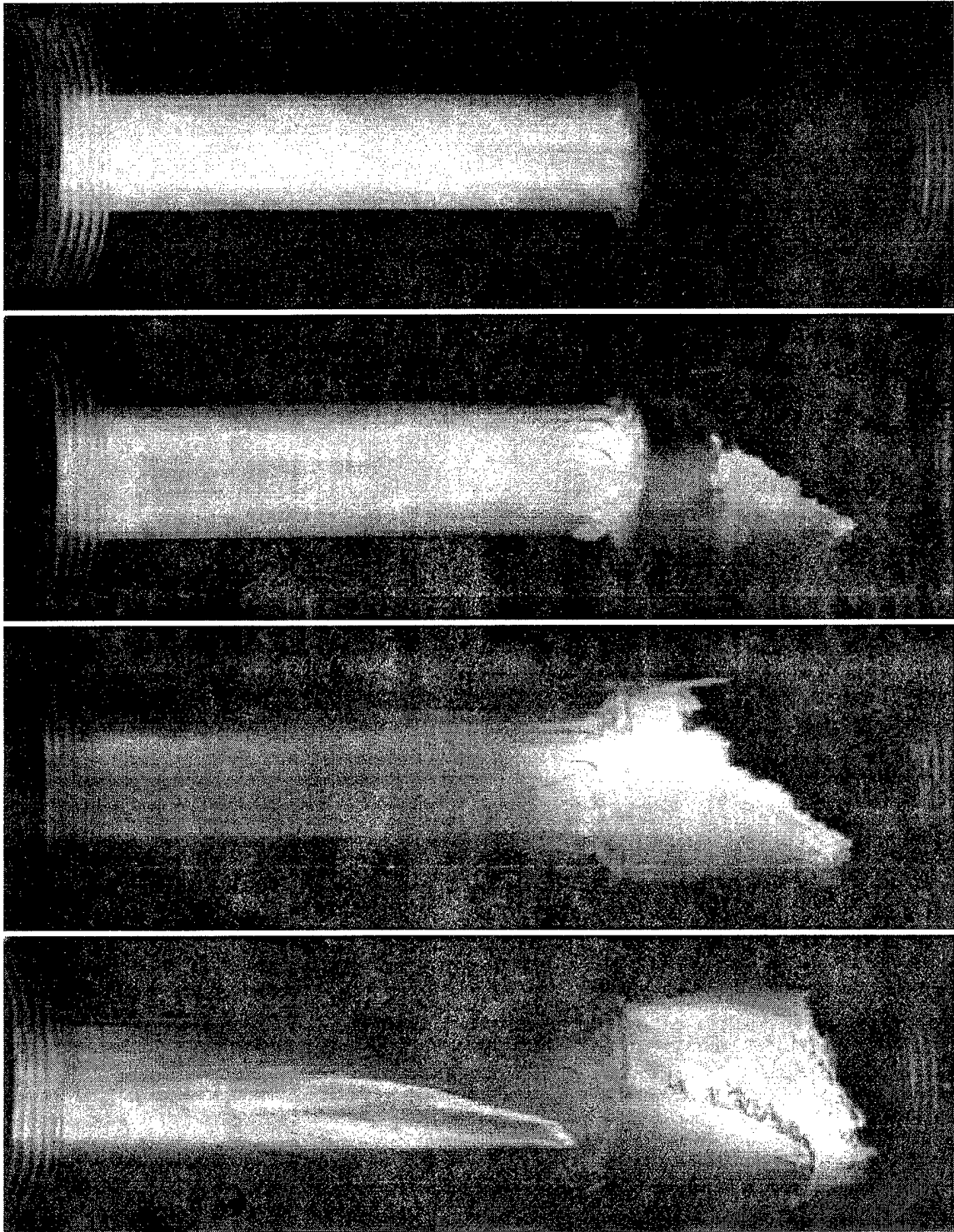


Figure 5: Still Photographs of Motor Y1 showing CCB consumption. Here, the CCB is located on the right hand side of the image and flow is from right to left. From top to bottom, images are for $t = 3.3, 5.45, 5.5,$ and 11.5 sec

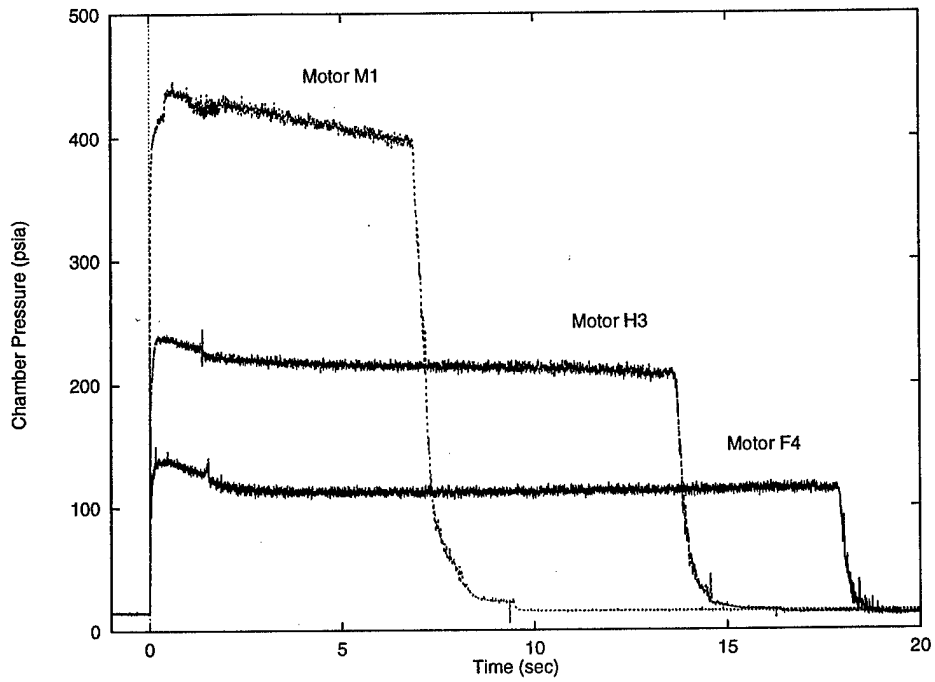


Figure 6: Measured Chamber Pressure Histories for Motors F4, H3, and M1 at Average Pressures of Roughly 100, 200, and 400 psi, Respectively

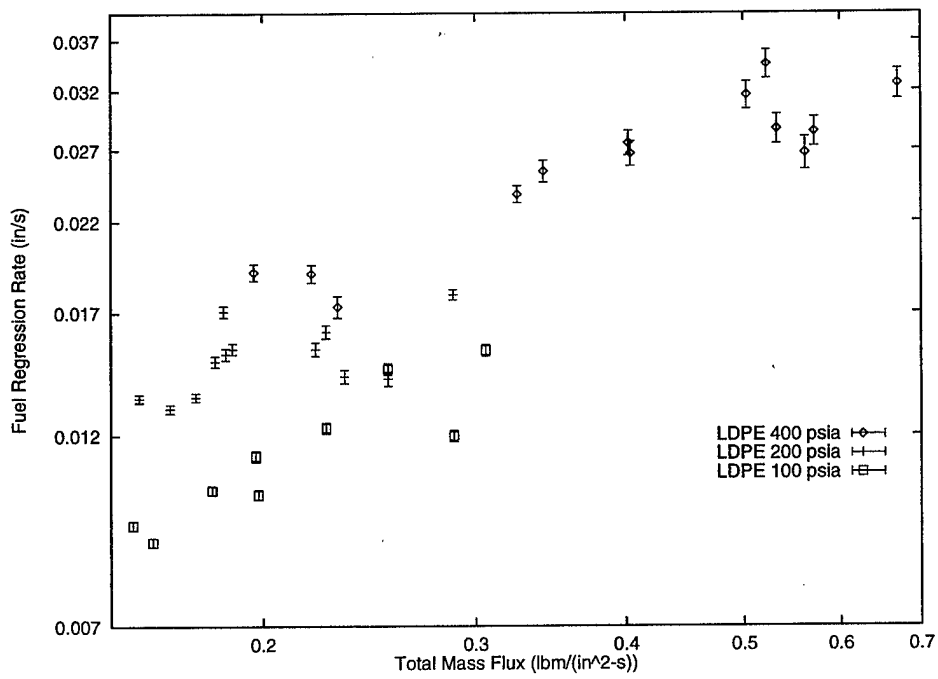


Figure 7: LDPE Fuel Regression Data Showing Effect of Pressure

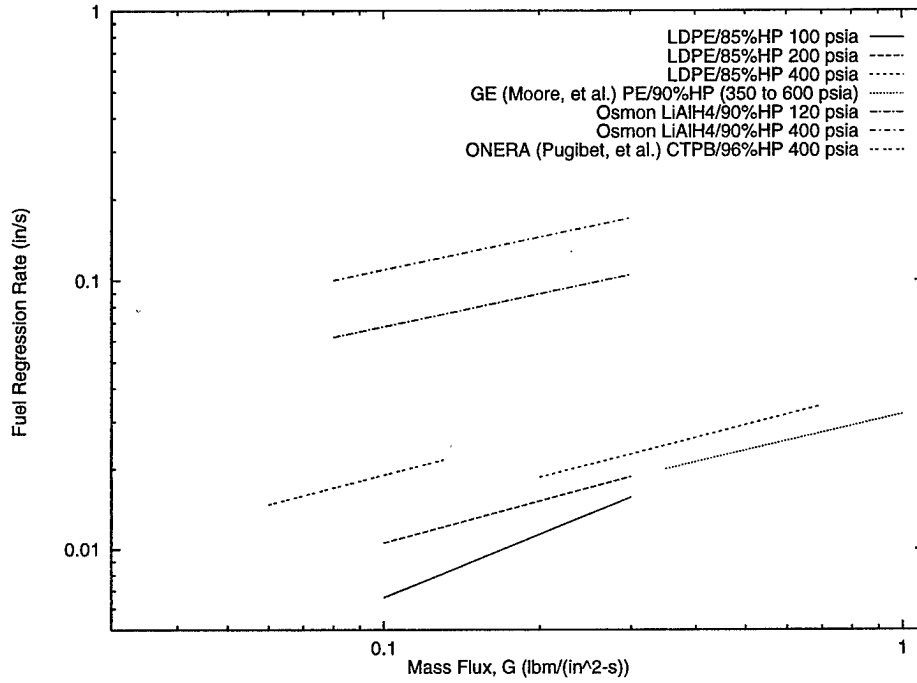


Figure 8: Comparison of Previous HP Investigators Regression Rate Measurements to Present Study

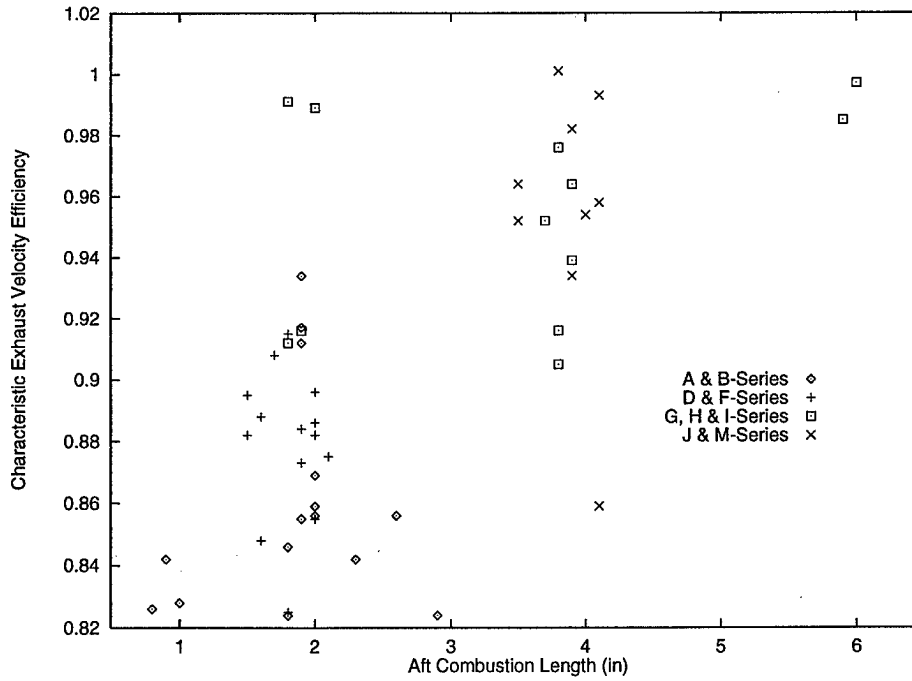


Figure 9: Effect of Aft Combustion Length on C^* Efficiency with Inerts

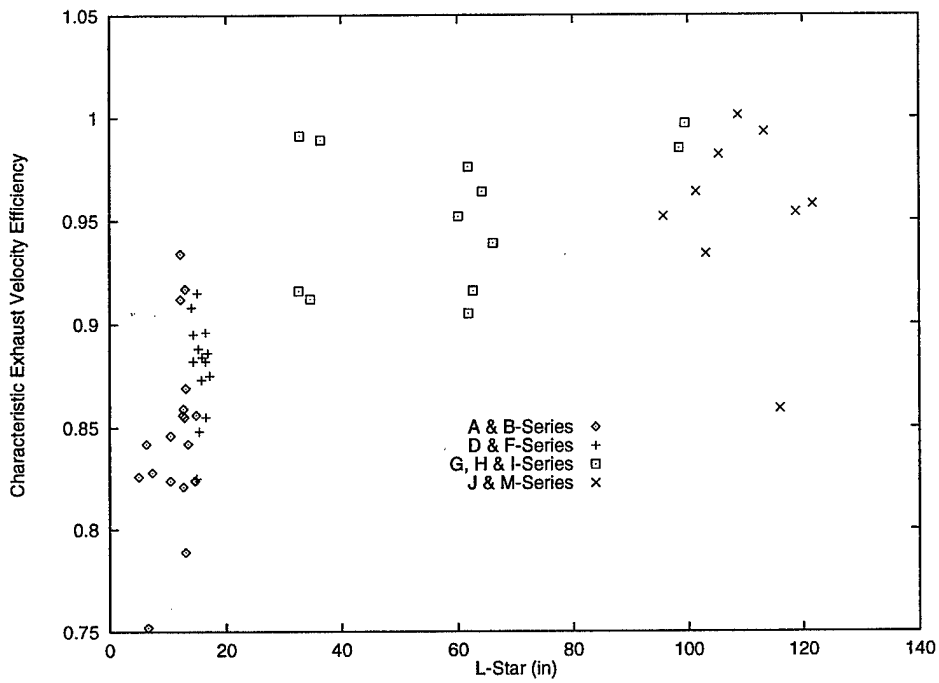


Figure 10: Effect of L^* on C^* Efficiency with Inerts

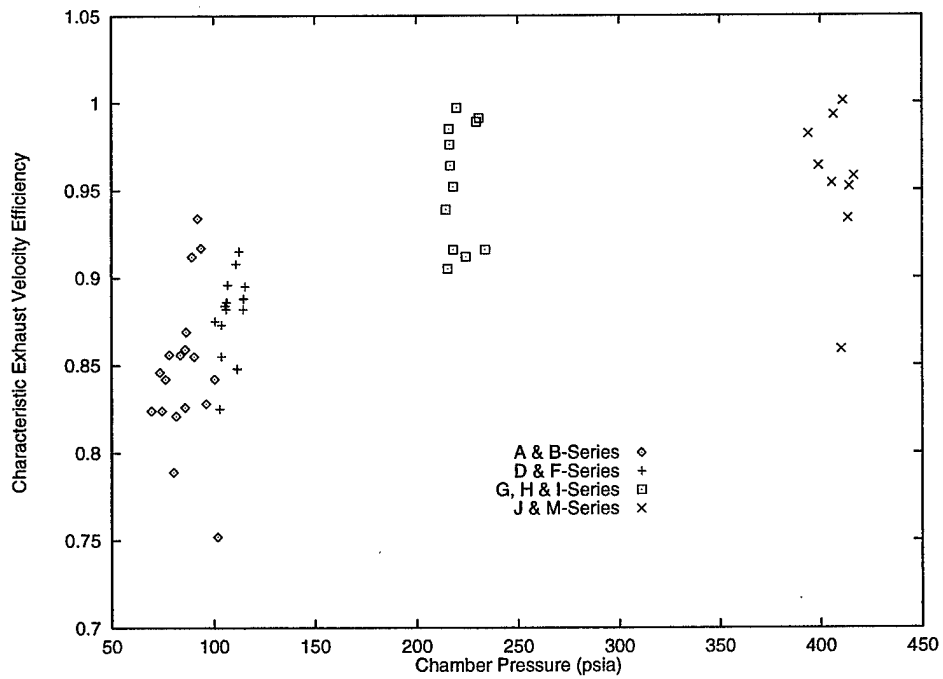


Figure 11: Effect of Chamber Pressure on C^* Efficiency with Inerts

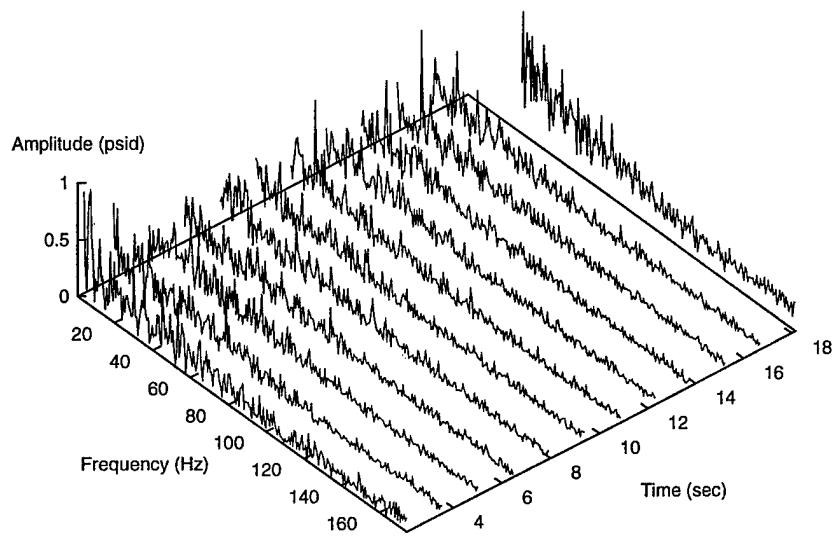


Figure 12: Waterfall Plot of Chamber Pressure from Motor F4

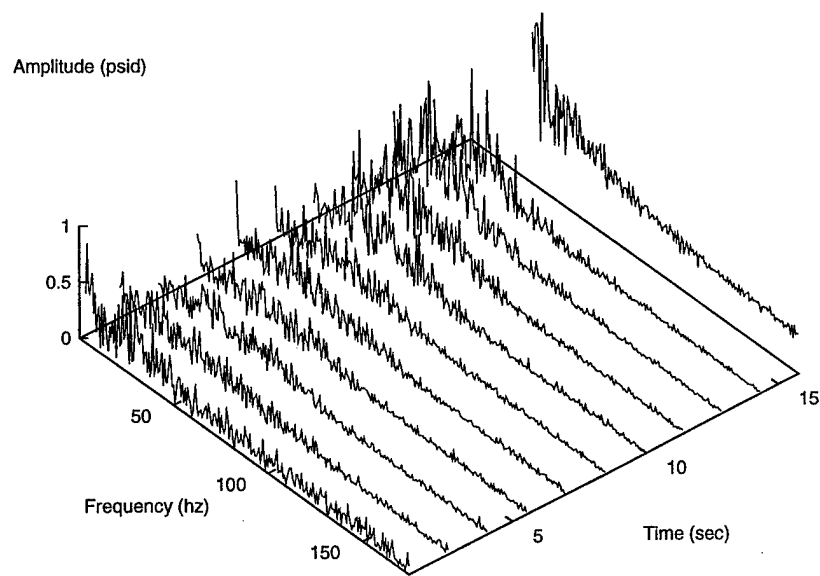


Figure 13: Waterfall Plot of Chamber Pressure from Motor G3

8 Appendix D - 3-D Boundary Element Model Development

Excerpts from Chao, C., Ph.D. Thesis, "Three-Dimensional Nonlinear Jet Atomization Model," Purdue University, December, 1998.

4. THREE DIMENSIONAL BOUNDARY ELEMENT METHOD FOR NONLINEAR DROPLET SIMULATION

4.1 Introduction

A three dimensional Laplace's solver has been developed in the previous chapter. The implementation of this 3-D solver for a nonlinear droplet simulation will be described in this chapter. Several auxiliary modules had to be built to support these simulations.

First, a grid generation module had to be developed for the droplet geometry. Grid generation will define the physical domain for the case we will study. It also specifies the proper initial conditions for the each node on the grid. Note that a given value of velocity potential (ϕ) or of the normal derivative of velocity potential (q) is required for each node in order to form a well posed boundary value problem. The grid generation process is described in Section 4.2.

Secondly, a procedure to calculate the normal vector, surface curvature and tangential velocity at each node is required. At every node, there exists an unique normal vector while an infinite number of tangential vectors exist at every node location. The normal vector serves as a fundamental factor for calculating other surface properties such as surface curvature and tangential velocity. Surface curvature is defined as the rate of change of normal vector, and it was introduced into the dynamic boundary condition as defined in Equation ?? by the relationship with the surface tension force. The experience gained from 2-D case shows that accurate methods have to be developed for calculating normal vector and curvature, especially for curvature which involves the computation of the second derivative of surface properties. Once the normal vectors are known, the tangential velocity can be calculated. The combination of the tangential velocity and the normal velocity forms the total velocity. The total velocity will facilitate the movement of a node to a new location. The procedure to calculate normal vectors, curvatures and tangential velocities for each node are explained in Section 4.3.1.

The chapter is concluded with a grid function convergence test (Section 4.4) and sample simulations (Section 4.5)

4.2 Grid Generation for a Sphere

The best way to construct grids for a sphere is to use a polyhedra with high degree of symmetry and order as a basic model. There are five polyhedra which can be selected as the basic model: tetrahedron, octahedron, cube, icosahedron, and dodecahedron [1]. These objects are all convex polyhedrons and have faces which are nonintersecting regular, plane, convex polygons with straight edges. An equal number of congruent faces meet at each vertex of a particular polygon, and each has a circumsphere which touches all of its vertices. Also, each polygon has the same size as an equilateral triangular face. The

octahedron has been chosen as basic model due to the ability to easily find the positions of its six vertices which simply lie on the x , y , and z axis with the length of radius in both positive and negative direction of each axis.

Based on this polygon, we are able to construct finer grids by subdivision and projection. Subdivision is used to break down an existing polygon in an orderly manner with a series of lines. The new points produced by the intersection of these lines will become the new vertices. Figure 4.1 depicts the process of subdivision on one face of an octahedron. The next step, projection, is to imagine that the subdivided polyhedron is surrounded by its circumscribing sphere, with its vertices touching that sphere. Each edge of the circumscribed polyhedron, together with each of the lines which subdivides its faces, should be projected from the center of the polyhedron onto the surface of the circumscribing sphere, as in Figure 4.2. When the subdivided polyhedron is projected onto the circumscribing sphere, each of its edges and each line drawn across a face becomes longer. Some of those lines are projected further outwards and become longer than the others, so the edges of the polyhedron are not all the same length and many triangular faces are not equilateral. Figure 4.3 shows four sets of spherical grid setups.

4.3 Free Surface Module

There are two methods to calculate the free surface properties. One involves in pre-determining a given fitting function for free surface and apply the least square fitting scheme to calculate the surface properties. Another is based on the equation derived by [2] and a suitable weighting functions. The following two subsections are devoted to these two methods. The method uses in 3D model is the first one due to its simplicity.

4.3.1 Calculate Surface Properties by a Given Function

The surface module will provide the calculation of normal vectors, surface curvatures, and tangential velocities. We can calculate those quantities using a fitting scheme. The calculation of the normal vector, the local curvature, and the local tangential velocity can be obtained by fitting the surface locally to a given function. The least square surface fitting will be used as the fitting scheme. The following method is following the procedure by Chahine [3] and Pozrikidis [2].

Supposed the surface can be represented locally around a given node by a function $F(x, y, z)$ which obeys $F(x, y, z) = 0$. The second degree polynomial fit function is chosen for the function $F(x, y, z)$ which has a general form as:

$$F(x, y, z) = ax^2 + by^2 + cz^2 + fxy + gxz + hyz + px + qy + rz + d \quad [4.1]$$

The function $F(x, y, z)$ is selected to be the best description the shape of domain we are interested. For example, for a sphere the coefficient d can be set to -1 and f , g , and h can set to be zero. The coefficients p , q , and r remain for the case of distorted sphere. Thus, the fit function for a sphere can be rewritten as:

$$F(x, y, z) = a_1x^2 + a_2y^2 + a_3z^2 + a_4x + a_5y + a_6z - 1 \quad [4.2]$$

The coefficients a_1 to a_6 can be obtained by direct fit method or least square method. For the direct fit method, the coefficients a_1 to a_6 are determined by choosing six points

which surround a given node. Numerical experiments show that this method produced less accurate results. Thus, the direct fit method was not used in the simulations. For the least square method, the errors to fit the function can be reduced to some level by using more surrounding nodes to calculate the coefficients a_1 to a_6 . Depending on the grid, the surrounding nodes can be used up to the third loop around a given node. For example, for the grid of 258 nodes, total surrounding nodes of a given node which includes the three loop nodes around it will have about 30 nodes. The coefficients a_1 to a_6 are then determined by a least square fit to the surface for these 30 nodes. Once the fitting function, $F(x, y, z)$, is obtained, the local normal vector can be calculated by :

$$\hat{n} = \pm \frac{\nabla F}{|\nabla F|} \quad [4.3]$$

The appropriate sign is chosen to insure the normal is pointed outward. Writing the normal vector by:

$$\hat{n} = n_1 \hat{i} + n_2 \hat{j} + n_3 \hat{k} \quad [4.4]$$

then:

$$n_1 = \frac{F_x}{|\nabla F|}, \quad n_2 = \frac{F_y}{|\nabla F|}, \quad n_3 = \frac{F_z}{|\nabla F|} \quad [4.5]$$

where F_x , F_y and F_z are the first derivative of function $F(x, y, z)$ with respect to x , y , and z , respectively. $|\nabla F|$ is the norm of gradient of function $F(x, y, z)$ which is defined as $\sqrt{n_1^2 + n_2^2 + n_3^2}$. And n_1 , n_2 and n_3 are three components of normal vector \hat{n} in \hat{i} , \hat{j} , and \hat{k} direction, respectively. The local surface curvature is obtained by:

$$\kappa = \nabla \cdot \hat{n} \quad [4.6]$$

Introducing Equation 4.2, curvature is given by:

$$\kappa = \frac{F_{xx}(F_y^2 + F_z^2)}{|\nabla F|^3} + \frac{F_{yy}(F_x^2 + F_z^2)}{|\nabla F|^3} + \frac{F_{zz}(F_x^2 + F_y^2)}{|\nabla F|^3} \quad [4.7]$$

where F_{xx} , F_{yy} , and F_{zz} are the second derivative of function $F(x, y, z)$ with respect to x , y , and z , respectively. In order to calculate the tangential velocity, the fitting process is performed on the velocity potential in a similar manner as for the normal vector. Since the velocity potentials are given on each vertex, the process of the surface fitting on ϕ is analogous to our approach for κ . The polynomial function has the similar form as for function $F(x, y, z)$ and we denote as $G(x, y, z)$ and is given by:

$$\phi(x, y, z) \approx G(x, y, z) = b_1 x^2 + b_2 y^2 + b_3 z^2 + b_4 x + b_5 y + b_6 z \quad [4.8]$$

The coefficients b_1 to b_6 are determined by least square method. Once the function $\phi(x, y, z)$ is determined locally, the tangential velocity can be calculated by:

$$\vec{v}_t = \hat{n} \times (\nabla \phi \times \hat{n}) \quad [4.9]$$

After introduction Equation 4.2 and Equation 4.8, tangential velocity can be obtained by:

$$\vec{v}_t = v_{t1} \hat{i} + v_{t2} \hat{j} + v_{t3} \hat{k} \quad [4.10]$$

with:

$$v_{t1} = n_2 G_{n3} - n_3 G_{n2} \quad [4.11]$$

$$v_{t2} = n_3 G_{n2} - n_1 G_{n3} \quad [4.12]$$

$$v_{t3} = n_1 G_{n2} - n_2 G_{n1} \quad [4.13]$$

where

$$G_{n1} = G_y n_3 - G_z n_2 \quad [4.14]$$

$$G_{n2} = G_z n_1 - G_x n_3 \quad [4.15]$$

$$G_{n3} = G_x n_2 - G_y n_1 \quad [4.16]$$

G_x , G_y , and G_z are the first derivative of the function $G(x, y, z)$ with respect to x , y , and z , respectively. Thus, by combining the tangential velocity and the normal velocity, the total velocity can be determined and is given by:

$$\vec{v} = \vec{v}_t + q\hat{n} \quad [4.17]$$

where q is the normal derivative of velocity potential.

4.3.2 Calculating Surface Properties Using Weighting Functions

A more general method to calculate surface properties not based on a predetermined function is described by Pozrikidis [2]. The basic idea involves using the weighting average methods to calculate surface properties. Normal vectors for each element are calculated first. Since normal vectors of each triangular element can be calculated easily by the information given by the three vertices' position. The normal vectors for each node are taking a weighting average over the surrounding elements about each node which is given by:

$$n_x^i = \sum_{i=1}^e n_x^i \Omega^i \quad [4.18]$$

$$n_y^i = \sum_{i=1}^e n_y^i \Omega^i \quad [4.19]$$

$$n_z^i = \sum_{i=1}^e n_z^i \Omega^i \quad [4.20]$$

where n_x^i , n_y^i , and n_z^i are the three components of normal vector a node i and Ω^i is the weighting function. Here, e denotes the total number of element surrounding node i . The success of this method relies on the selection of a suitable weighting function. The first try for selection of the weighting function is to use the arithmetic averaging. The implementation of arithmetic averaging will result in twice averaging the normal vectors which could introduce too much damping. The numerical results proved this speculation by reducing droplet movement when compared to the technique described in Section 4.3.1. Thus, a more advanced weighting method was desired.

The curvature can be calculated by the method described by Pozrikidis [2]. The mean curvature (k_m) at a given point is given by:

$$k_m = \frac{1}{2}(k(0) + k(\infty)) \quad [4.21]$$

with

$$k(0) = \frac{1}{a_{\eta\eta}} \frac{\partial \vec{n}}{\partial \eta} \frac{\partial \vec{x}}{\partial \eta} \quad [4.22]$$

and

$$k(\infty) = \frac{1}{a_{\eta\eta}} \frac{\partial \vec{n}}{\partial \eta} \frac{\partial \vec{x}}{\partial \eta} \quad [4.23]$$

where the metric tensor \vec{a} is given by:

$$a_{\eta\eta} = \frac{\partial \vec{x}}{\partial \eta} \frac{\partial \vec{x}}{\partial \eta} \quad [4.24]$$

$$a_{\eta\xi} = a_{\xi\eta} = \frac{\partial \vec{x}}{\partial \eta} \frac{\partial \vec{x}}{\partial \xi} \quad [4.25]$$

$$a_{\xi\xi} = \frac{\partial \vec{x}}{\partial \xi} \frac{\partial \vec{x}}{\partial \xi} \quad [4.26]$$

And, by using linear triangular element, the surface properties are given by:

$$P(\eta, \xi) = (1 - \eta - \xi)P_1 + \eta P_2 + \xi P_3 \quad [4.27]$$

Thus, the metric tensor is given by:

$$a_{\eta\eta} = x_\eta^2 + y_\eta^2 + z_\eta^2 \quad [4.28]$$

$$a_{\eta\xi} = x_\eta x_\xi + y_\eta y_\xi + z_\eta z_\xi \quad [4.29]$$

$$a_{\xi\xi} = x_\xi^2 + y_\xi^2 + z_\xi^2 \quad [4.30]$$

Substituting the above three equations into Equation 4.22 and Equation 4.23, we obtain;

$$k(0) = \frac{1}{a_{\eta\eta}(n_{x,\eta}x_\xi) + n_{y,\eta}y_\eta + n_{z,\eta}z_\eta} \quad [4.31]$$

$$k(\infty) = \frac{1}{a_{\xi\xi}(n_{x,\xi}x_\xi) + n_{y,\xi}y_\xi + n_{z,\xi}z_\xi} \quad [4.32]$$

The mean curvature is calculated by Equation 4.21.

The velocity potential is given at each node and its distribution over an element is given by:

$$\phi(\eta, \xi) = (1 - \eta - \xi)\phi_1 + \eta\phi_2 + \xi\phi_3 \quad [4.33]$$

Thus, the components of the gradient potential velocity for a given element are given by:

$$\frac{\partial \phi}{\partial x} = \frac{\partial \phi}{\partial \eta} \frac{\partial \eta}{\partial x} + \frac{\partial \phi}{\partial \xi} \frac{\partial \xi}{\partial x} \quad [4.34]$$

$$\frac{\partial \phi}{\partial y} = \frac{\partial \phi}{\partial \eta} \frac{\partial \eta}{\partial y} + \frac{\partial \phi}{\partial \xi} \frac{\partial \xi}{\partial y} \quad [4.35]$$

$$\frac{\partial \phi}{\partial z} = \frac{\partial \phi}{\partial \eta} \frac{\partial \eta}{\partial z} + \frac{\partial \phi}{\partial \xi} \frac{\partial \xi}{\partial z} \quad [4.36]$$

with

$$\phi_\eta = \phi_2 - \phi_1 ; \phi_\xi = \phi_3 - \phi_1 \quad [4.37]$$

In order to obtain those components of the gradient potential velocity at each node, an averaging scheme needed to be implemented. Once the gradient potential at each node is calculated, the the tangential velocity and total velocity can be calculated by Equation 4.17 and Equation 4.9, respectively.

Table 4.1 Grid Setup for the Test of Grid Convergence

Grid Set	No. of Nodes	No. of Elements
No. 1	6	8
No. 2	18	32
No. 3	66	128
No. 4	258	512

4.4 Grid Convergence Test

Since the 3-D model is developed to solve the Laplace equation, there exists an analytical solution for a simple domain like a sphere by specifying the boundary conditions on the surface of the sphere of either Dirichlet or Neumann type. For the testing given below, the boundary condition of the Dirichlet type has been used.

The boundary condition is given by specifying a function, say $\Phi(x, y, z)$, which will satisfy the Laplace equation. Then, the normal derivatives of $\Phi(x, y, z)$ can be calculated analytically by $q_{ana} = \partial\Phi/\partial n$ and the results will be used to compare the results from 3-D BEM model. The subscript of q_{ana} denotes the analytical solution for q . The function for $\Phi(x, y, z)$ has been chosen to be:

$$\Phi(x, y, z) = \exp(x)\cos(y) + \exp(z)\sin(x) \quad [4.38]$$

And, for a sphere, the surface can be represented by:

$$F(x, y, z) = x^2 + y^2 + z^2 - 1 \quad [4.39]$$

which provides the q_{ana} can be calculated by:

$$q_{ana}(x, y, z) = \frac{\partial\Phi}{\partial n} = \hat{n} \cdot \nabla\Phi \quad [4.40]$$

The \hat{n} values are calculated by $\nabla F/|\nabla F|$ described in Section 4.3.1. Four sets of grids have been used for the test of grid convergence. Table 4.1 is highlights the number of nodes and elements used for the grid convergence test.

Figures 4.4, 4.5, 4.6, and 4.7 show the error in q between numerical and analytical solutions for these four different grids. For the grid with only six nodes on the spherical surface, the difference between the analytical and numerical results shows a large discrepancy in Figure 4.4. However, the error will reduce about one order when a finer grid setup with 18 nodes on the spherical surface is used. The trend of reducing error is held for using the even more finer grid setup as 66 nodes and 258 nodes are used. Figure 4.8 is a error plot for these four different grid setups.

Another way to look at the grid convergence phenomenon is by showing the error reducing trend for choosing the same grid points which appear on the these four grid setups. Table 4.2 indicates that there are six points which appear in all the four grids.

These six points will be remained when the subdivision and projection process be applied to construct a finer grid for a sphere. Table 4.3 shows the error decreases as the finer grids

Table 4.2 Six Common Grid Points for the our Different Grid Setups

Node Location	x	y	z
No.1	0.0	1.0	0.0
No.2	0.0	0.0	1.0
No.3	1.0	0.0	0.0
No.4	-1.0	0.0	0.0
No.5	0.0	-1.0	0.0
No.6	0.0	0.0	-1.0

Table 4.3 Results of Test of Grid Convergence:Part I

qerr	Node Location No.1	Node Location No.2	Node Location No.3
6 nodes	0.266241	-0.032797	-0.864719
18 nodes	-0.032538	-0.021071	-0.037991
66 nodes	-0.005458	-0.002019	0.055933
258 nodes	-0.003276	-0.000160	0.024899
qerr	Node Location No.4	Node Location No.5	Node Location No.6
6 nodes	-0.269631	0.266241	-0.032797
18 nodes	0.050957	-0.032528	-0.021071
66 nodes	0.018494	-0.005458	-0.002019
258 nodes	0.005620	-0.003276	-0.000160

are applied for all of the six common points. While the scheme is formally second order, the convergence rates are not as rapid as one would expect. Here, the largest error result be attributed to the changes in surface shape with changing number of nodes. In this case, convergence is also measuring the rate at which the grid converges to a perfect sphere. Based on the evidence in these calculations (and in Chapter ??) the code was presumed to be valid for use in time-dependent simulations.

4.5 Sample Calculation - Droplet

In order to verify the time-dependent capabilities of the 3-D code developed in the previous sections, the model was used to simulate the distortion of a droplet. The driving force for the distortion of a droplet is due to surface tension. Different modes oscillation are investigated for the droplet simulation. In order to show the different modes movement of droplet, the initial values of velocity potential are specified by Legendre function. The Legendre function is the solution of Laplace equation in spherical polar coordinate system and symmetry about the z axis, ie. the dependent variable of Laplace equation is independent of θ where $\theta \in [0, 2\pi]$. Thus, the Legendre functions are the solution of the following equation:

$$\nabla^2 u = \frac{\partial^2 u}{\partial r^2} + \frac{2}{r} \frac{\partial u}{\partial r} + \frac{1}{r^2} \frac{\partial^2 u}{\partial \phi'^2} + \frac{\cot \phi'}{r^2} \frac{\partial u}{\partial \phi'} \quad [4.41]$$

where $\phi' \in [0, 2\pi)$ and the prime added to distinguish the variable used for the velocity potential ϕ . The dependent variable is velocity potential in this case. Therefore, the initial value for velocity potentials are specified by:

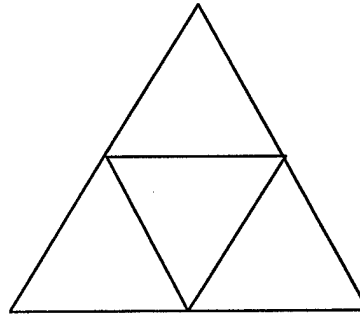
$$\phi(r, \theta, \phi') = \epsilon P_n(\cos \theta) \quad [4.42]$$

with,

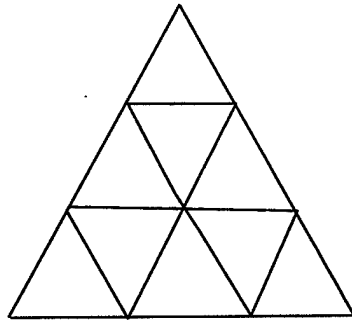
$$0 \leq \phi < \pi \quad 0 \leq \theta < 2\pi \quad [4.43]$$

where $P_n(\cos \theta)$ is the Legendre function of order n . The order will refer to the mode number for the following simulation.

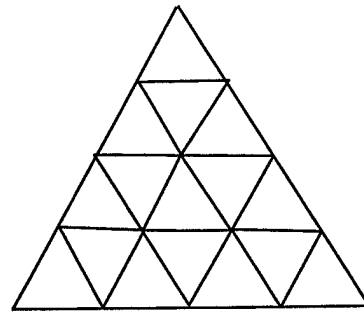
Figure 4.9 shows the half period of third mode oscillation for $\epsilon = 0.001$ with 66 nodes and 128 elements on the spherical surface. The characteristic of the third mode oscillation is the three lobe shape on the spherical surface. Figure 4.10 shows the half period of the fourth mode oscillation with the same conditions as the third mode oscillation. The four lobe shape is developed for the fourth mode oscillation. Since no regridding process has been applied in these cases, the simulations were restricted to a small perturbations.



Subdivided by two

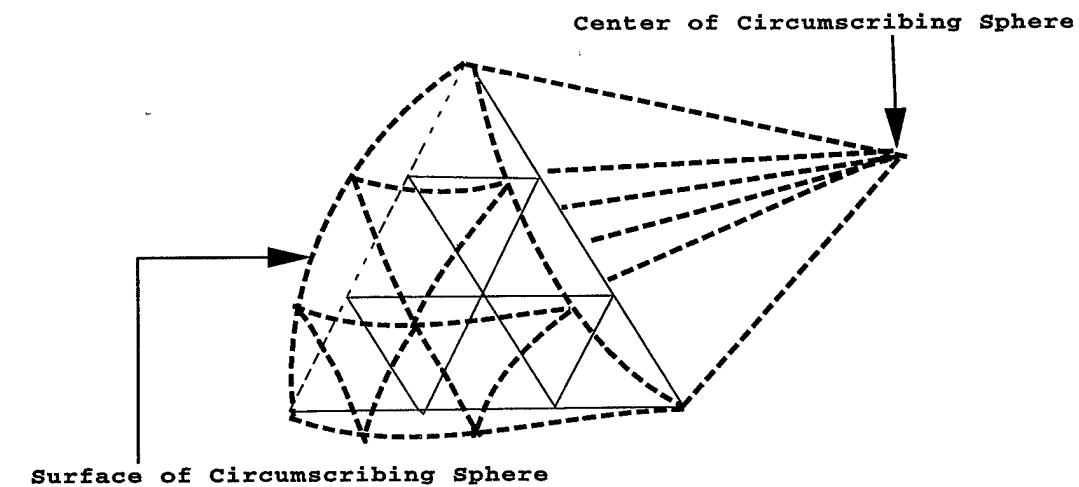


Subdivided by three



Subdivided by four

Figure 4.1 Subdivision of a Face of an Octahedron



Each Vertices Lie on the
Circumscribing Sphere

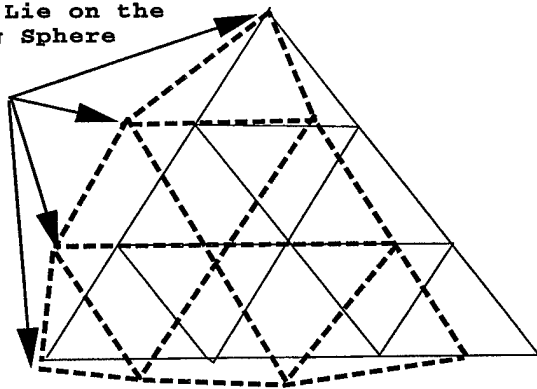


Figure 4.2 Projection of Subdivided Nodes on the Surface of a Sphere

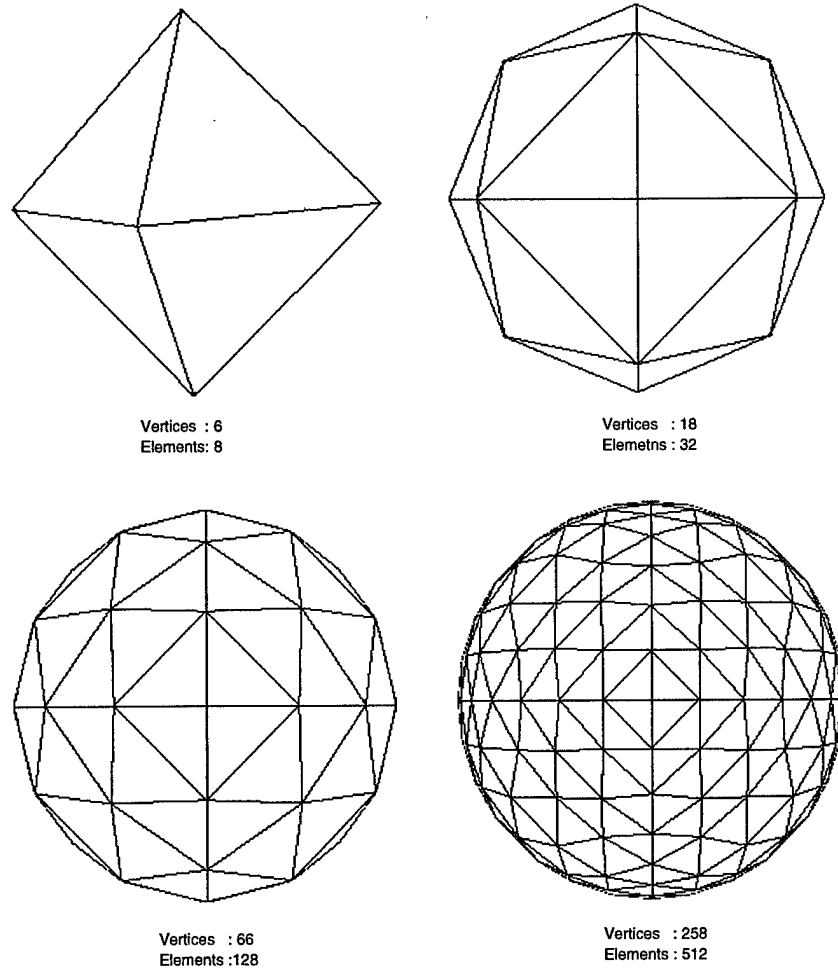


Figure 4.3 Four Sets of Grids for a Sphere

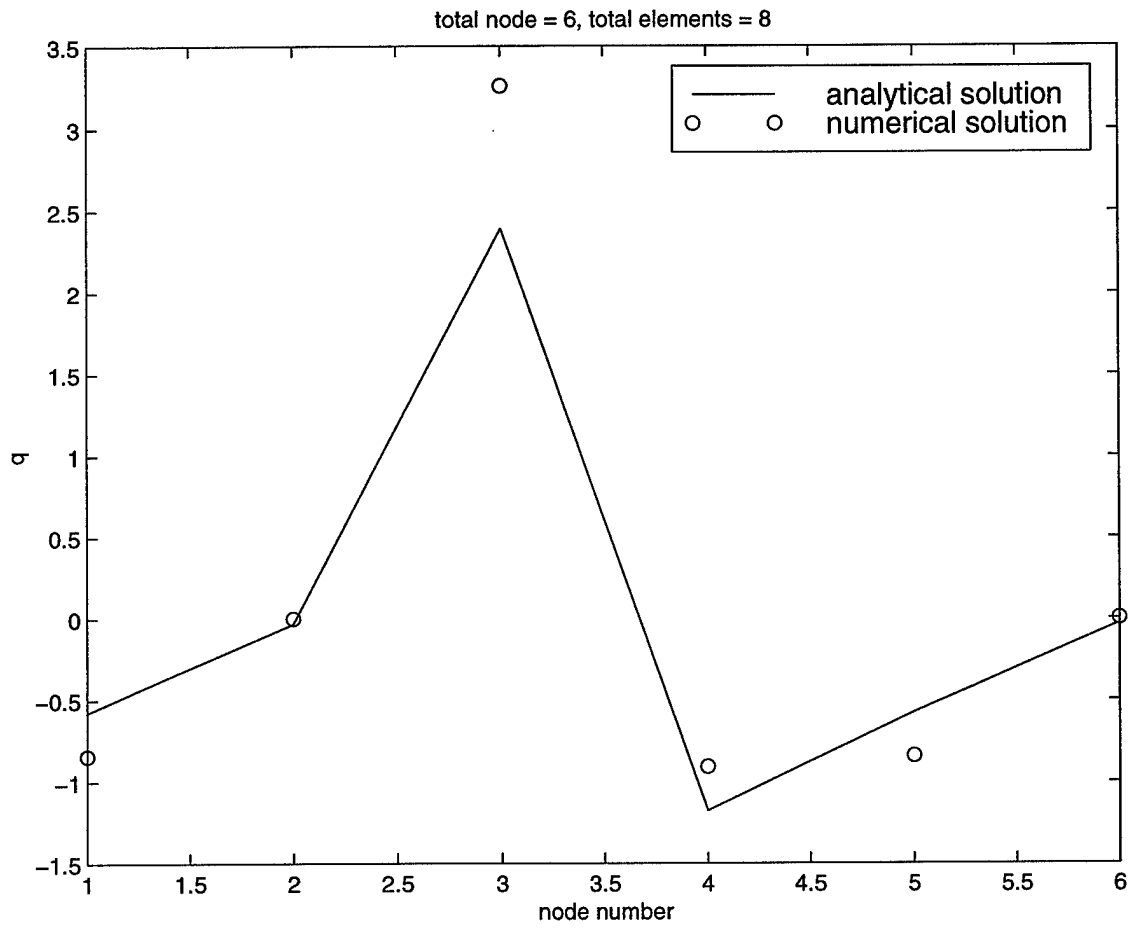


Figure 4.4 Comparison of Analytic and Numerical Surface Velocities for a Six Node Grid

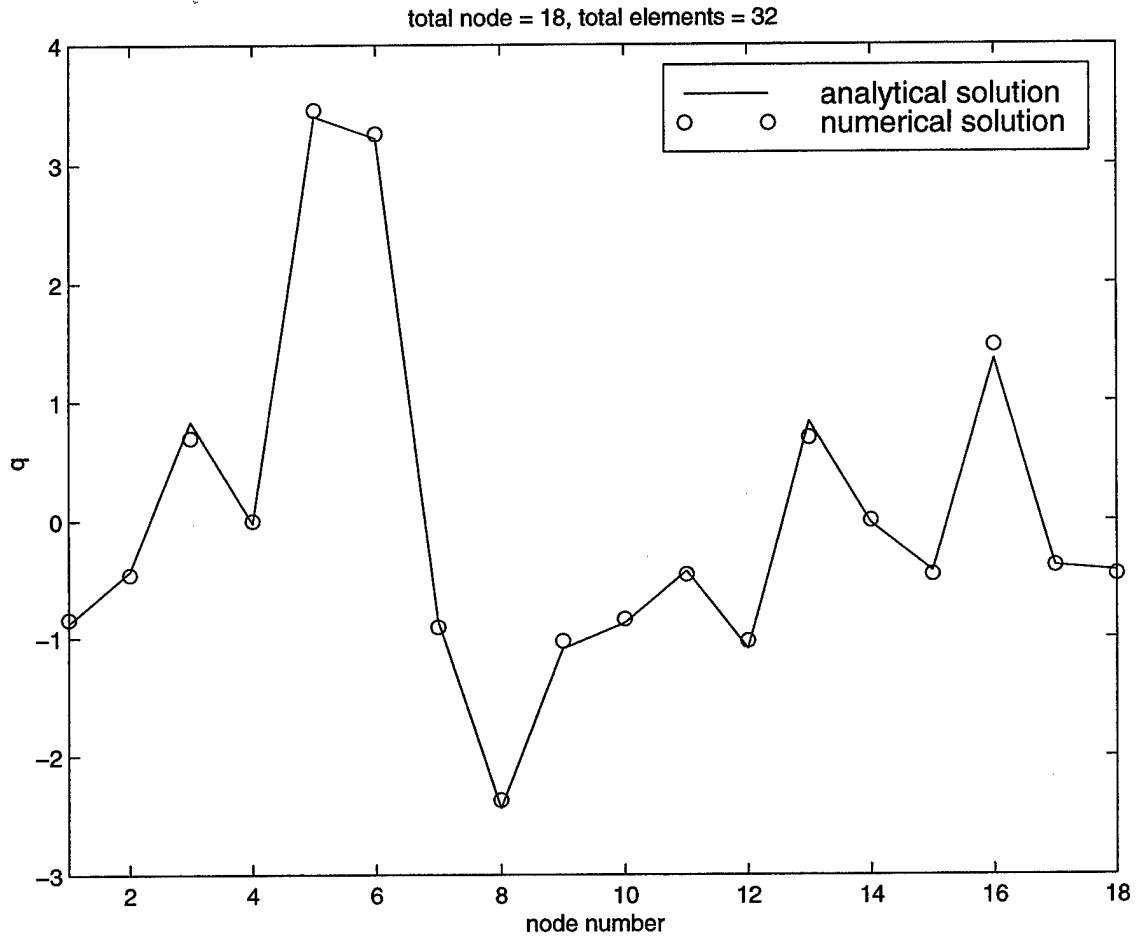


Figure 4.5 Comparison of Analytic and Numerical Surface Velocities for a 18 Node Grid

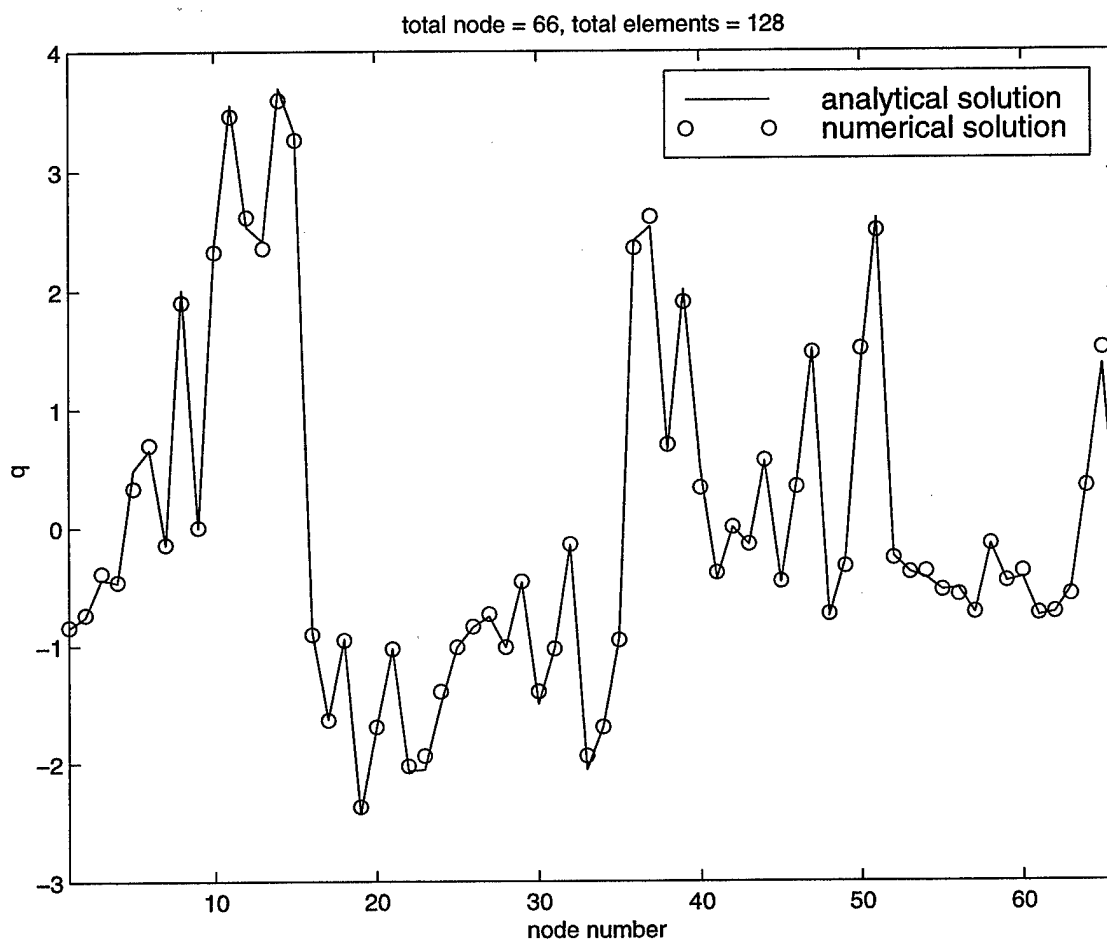


Figure 4.6 Comparison of Analytic and Numerical Surface Velocities for a 66 Node Grid

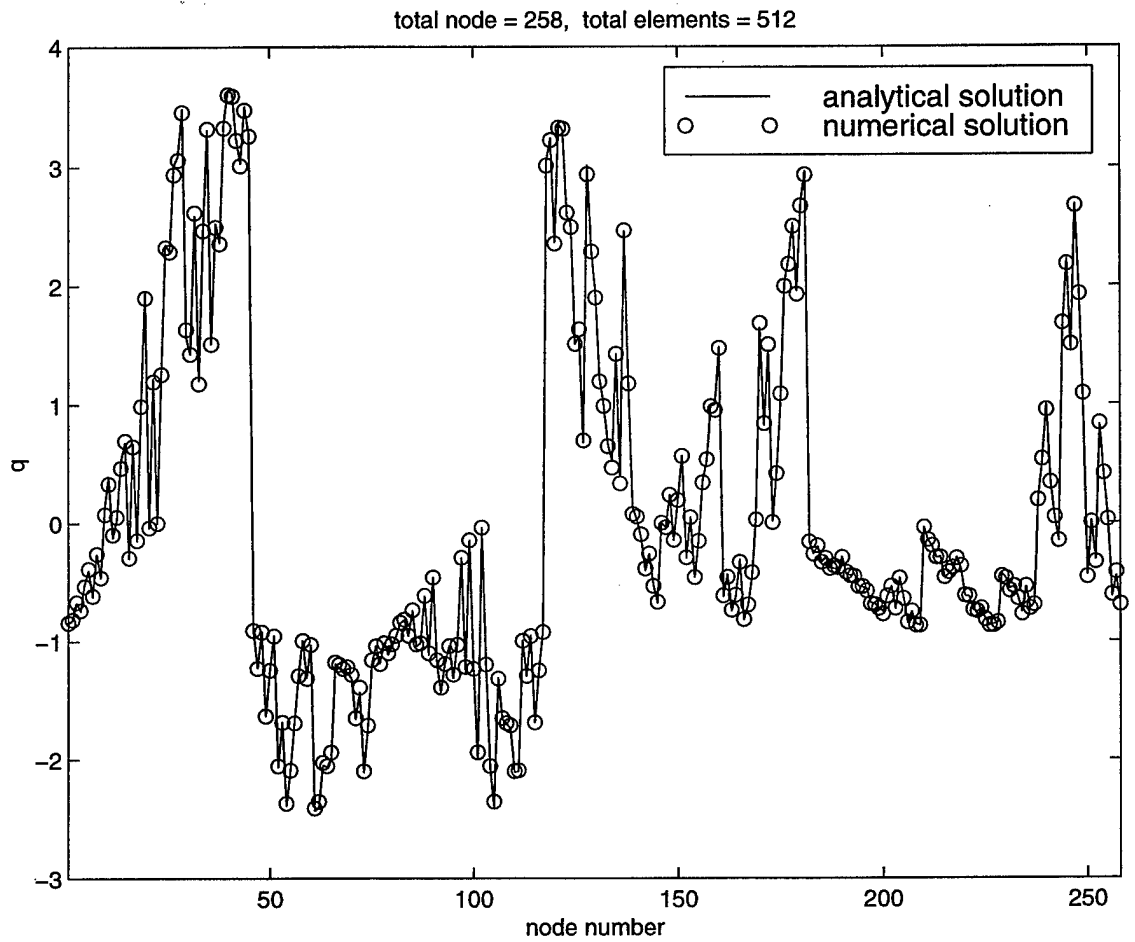


Figure 4.7 Comparison of Analytic and Numerical Surface Velocities for a 258 Node Grid

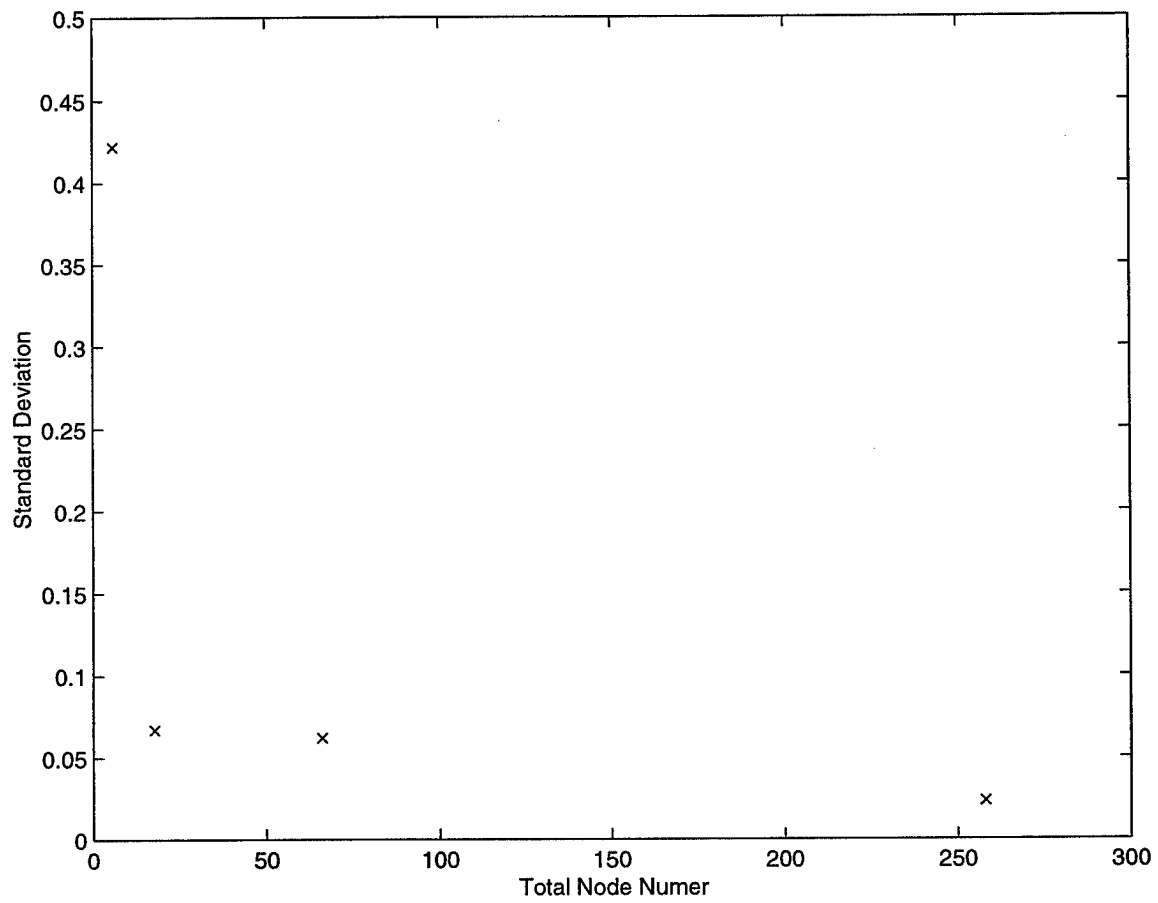


Figure 4.8 Standard Deviation in q vs. Four Different Grid Setups: 6, 18, 66, and 258

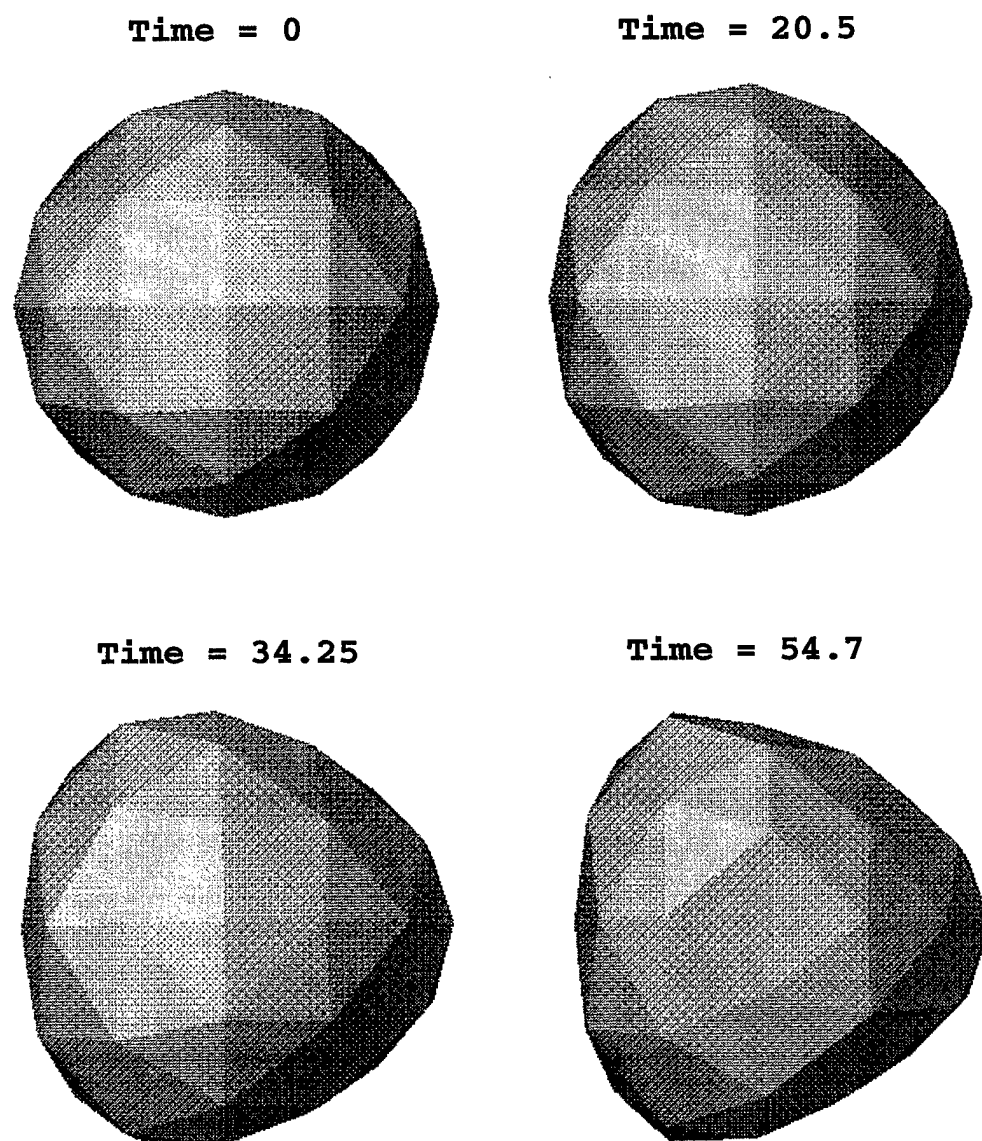


Figure 4.9 Third Mode Oscillation of Droplet

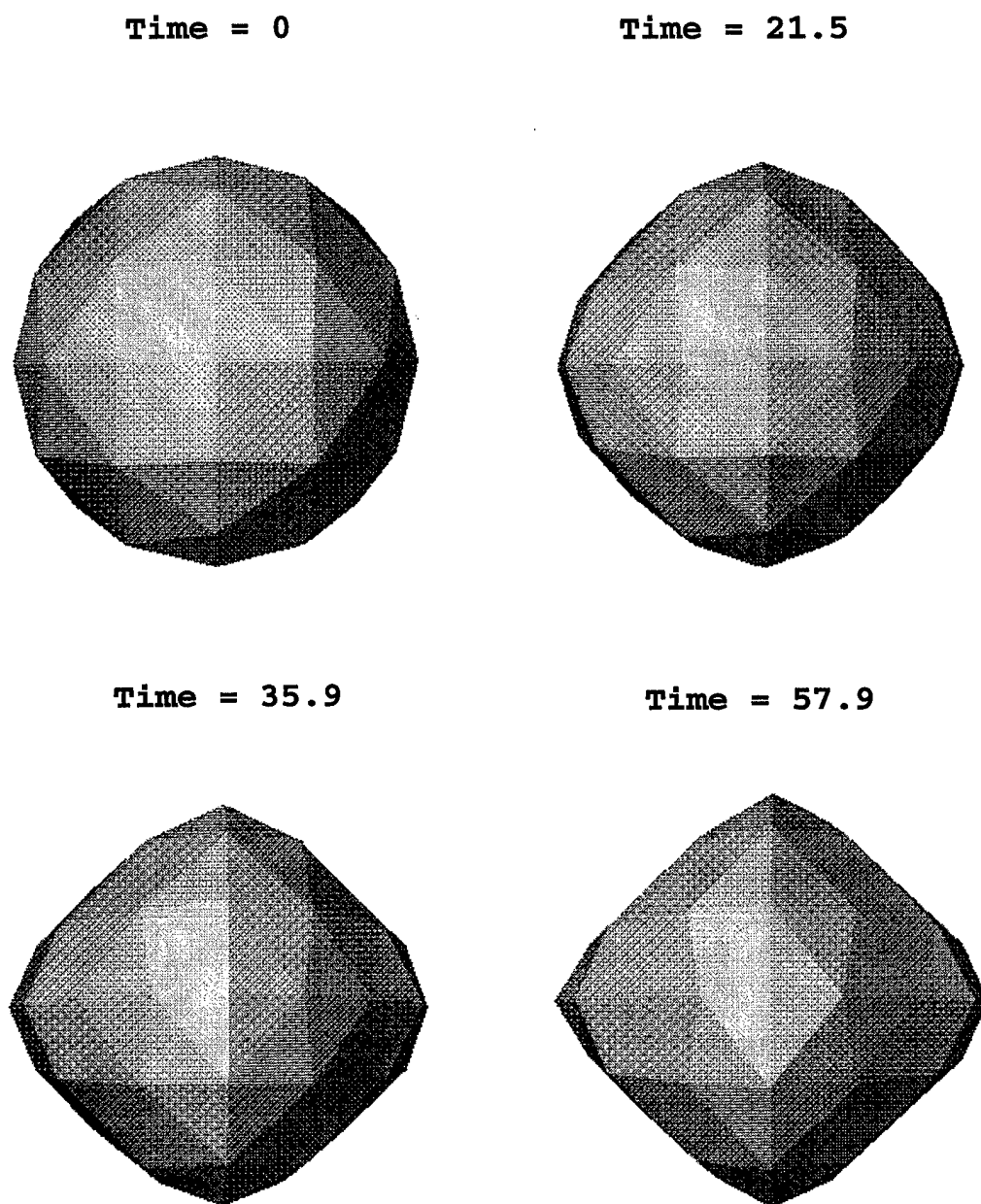


Figure 4.10 Fourth Mode Oscillation of Droplet

5. THREE DIMENSIONAL BOUNDARY ELEMENT METHOD FOR NONLINEAR INFINITE LIQUID JET SIMULATION

5.1 Introduction

A process to solve the problem of nonlinear deformation of an infinite jet subjected to both axial and circumferential disturbances by using 3-D BEM model developed in Chapter ?? is described in this chapter. This process begins with a description of an analytic temporal instability analysis by Yang [4](as described in Section 5.2). The resulting dispersion equation has been simplified to fit our assumptions and serves as an analytic solution to compare to the numerical results from 3-D BEM model. Section 5.3 describes a grid generation process for the liquid column. The liquid column serves as a portion of an infinite liquid jet. The initial shape of jet can be arbitrary specified by manipulated the longitudinal (streamwise) wave number and transverse (circumferential) wave numbers.

As in the previous chapter, a free surface module is developed specifically for the jet geometry in Section 5.4. Different fit functions are chosen for the jet due to the different geometric shape. The process of dealing with the corner problem is described in this section. A view of nonaxisymmetric wave on the liquid jet is described in Section 5.5. Section 5.6 presents the results of the comparison is made between the analytic linear stability analysis(Section 5.2) numerical model.

5.2 Dispersion Equation

The mathematical model used for the temporal instability analysis is based on linear analysis conducted by Yang [4].The resulting dispersion equation has been simplified to fit our assumptions of inviscid flow with negligible gas-phase effects. Surface tension is a dominant force for the instability of the low speed jet which is also called the capillary jet. Rayleigh [5] showed that only unstable mechanism to cause the breakup of a low speed jet is the growth of axisymmetric waves which are also referred to as dilation waves. For the high speed jet, the transverse modes are introduced by viscous and turbulent effects at the nozzle exit. Asymmetric waves are also called sinuous waves. In order to understand the behavior of the sinuous wave, the theory has to include the transverse mode oscillation.

Yang's theory begins with a two stream flow, liquid jet and gas stream, which are assumed to be incompressible and inviscid fluid. Liquid jet with density ρ_1 and issued at a uniform speed U_1 , while a coaxial gas with density ρ_2 flowed with a uniform speed U_2 . the interface between liquid and gas phase has been perturbed by:

$$\eta = \eta_1 = \eta_2 = \eta_0 e^{i(kz+m\theta)+\alpha t} \quad [5.1]$$

where η_0 is perturbation magnitude, k and m are the wave number in streamwise or longitudinal and azimuthal or transversal direction, respectively. Here, α is a complex variable,

$\alpha = \alpha_r + i\alpha_i$. The real part of α , α_r , is the growth rate. The positive value of α_r indicates the wave growth, while the negative value indicates the wave is stable and will eventually damp out. The imaginary part of α , α_i , is connected to the wave propagation speed. The resulting characteristic equation, i.e., dispersion equation is given by:

$$(\alpha_r^*)_m^2 = \frac{\gamma_m \beta_m Q (ka)^2}{(\gamma_m + \beta_m Q)^2} + \frac{ka}{We} \frac{1 - m^2 - (ka)^2}{\gamma_m + \beta_m Q} \quad [5.2]$$

where:

$$(\alpha_r^*)_m^2 = \frac{(\alpha_r)_m^2}{(U_1 - U_2)^2/a^2} \quad [5.3]$$

$$We = \frac{a(U_1 - U_2)^2 \rho_1}{\sigma} \quad [5.4]$$

$$Q = \frac{\rho_2}{\rho_1} \quad [5.5]$$

$$\gamma_m = \frac{kI_m(ka)}{I'_m(ka)} \quad [5.6]$$

$$\beta_m = \frac{-kK_m(ka)}{K'_m(ka)} \quad [5.7]$$

And, a is the radius of nozzle. I_m is the modified Bessel function of the first kind and order m . K_m is the modified Bessel function of the second kind and order m . The prime on I_m and K_m denotes the first derivative with respect to their parameters. For an axisymmetric wave oscillation, the azimuthal wave number m is simply equal to zero. Thus, the asymmetric instability is introduced by providing nonzero value of m .

In order to fit in our previous assumptions, we let Q and U_2 be equal to zero for the absence of gas phase which also provides $We = 1$. Thus, we have

$$(\alpha_r^*)_m^2 = (ka)[1 - m^2 - (ka)^2] \frac{I'_m(ka)}{kI_m(ka)} \quad [5.8]$$

Figure 5.3 shows the plot of growth rate, $(\alpha_r^*)_m^2$ vs ka at different values of m . It indicates that the only unstable wave for a quiescent, incompressible, and inviscid liquid jet is axisymmetric wave. All of non-axisymmetric modes ($m > 0$) are stable due to the negative values of growth rate over all of dimensionless streamwise wave number ka .

Thus, the dispersion equation is used for the temporal instability analysis later in this chapter is given by:

$$(\alpha_r^*)_0^2 = (ka)[1 - (ka)^2] \frac{I'_0(ka)}{kI_0(ka)} \quad [5.9]$$

which is identical to the result of Rayleigh's analysis.

5.3 Grid Generation of a Liquid Column

The first step in the numerical analysis is to set up the grid points for a liquid jet. A cylinder with a small perturbation on the surface is used to represent the initial shape of the liquid jet. Figure 5.1 depicts the small perturbation on the surface of the liquid jet in

Table 5.1 Three Different Grid Setups for a Liquid Column

	int_z	int_theta	int_r	total nodes	total elements
Set 1	5	5	2	42	80
Set 2	20	6	3	222	440
Set 3	30	10	3	452	900

the $r - z$ plane and $r - \theta$ plane. Since the liquid jet is assumed to be of infinite length, the computational domain is chosen to be one wavelength (λ) of the perturbation.

A grid generation scheme has been applied on a portion of an infinite liquid jet which is described by a cylindrical column. This cylindrical column is constituted by a side surface and two end faces. Each surface requires a different method to construct grid points and elements. The result of grid generation is to provide information about the location of each grid points on the surface and what three nodes to make up each triangular element.

The number of intervals in the r , θ , and z directions (int_r, int_z, and int_theta, respectively) must be input in order to generate the grid. The value of int_z will show int_z + 1 nodes on the wave along the longitudinal direction, while int_theta + 1 nodes along the transversal direction. The total length of a liquid column is given by $n \cdot \lambda$ where n is the number of wavelengths and λ denotes wavelength, note that λ is given by $\lambda = 2\pi/k$ where k is the wave number in the streamwise or longitudinal direction. The initial shape of the liquid column is given by:

$$r = 1 + \delta \cos(kz + m\theta) \quad [5.10]$$

where δ is the perturbation magnitude. For an undisturbed column, δ is given by zero, and an axisymmetric column is given by $m = 0$. Table 5.3 highlights three grid setups, and the geometrical perspective of these three grid setups are shown on Figure 5.4.

5.4 Free Surface Modules

The process to calculate the surface normal vector, surface curvature, and tangential velocity is the same as the methods used in the droplet case as discussed in Chapter 4. There are three major differences between the droplet case and the jet case. First is the usage of a different fit function for the surface fitting due to the different geometrical domain in the liquid jet case. The least square method is also applied for the fitting scheme in the liquid jet case, but here the fit function is chosen to be:

$$F(x, y, z) = a_1x^2 + a_2y^2 + a_3x + a_4y + a_5z - 1 \quad [5.11]$$

And, the fit function for the velocity potential fitting in the liquid jet case is chosen to be:

$$\phi(x, y, z) = G(x, y, z) = b_1x^2 + b_2y^2 + b_3x + b_4y + b_5z \quad [5.12]$$

The accuracy of the fitting function can be determined by observing the results of surface curvature for an undisturbed jet. For an undisturbed jet which is a smooth cylindrical

column, the surface curvature is equal to one at every node on the surface side which does not include the nodes on the two end faces.

The second difference between droplet case and jet case is the appearance of the corner nodes in the jet case. The corner nodes are referred to the nodes that lie on the intersection portion between the surface side and two end faces. Those nodes have multiple value of q which is $q = \partial\phi/\partial n$. Since these two end faces are the cross sections of an infinite jet which serve as symmetry planes. By the definition, the values of q are set to be zero for the nodes on these symmetry planes. Thus, the elements lying on one of the two end faces will have no contribution to the multiple value problem of q since q is zero on these elements. However, for the elements on the surface side, an assumption is made to deal with the multiple value of q . Since the multiple value problem is arisen due to the different normal vectors associated with those surrounding elements, these differences in the normal vectors can be assumed to be small when a finer grid is used. Therefore, multiple value of q for those elements becomes a single value of q .

An example is given to further explain how to deal with the multiple value of q on the corner nodes. For grid setup number 1 mentioned in Table 5.3, the corner node and their surrounding elements are shown on the Figure 5.5. The zoom-in picture in Figure 5.5 shows the node numbers and element numbers surrounding node 6. The dark portion of this zoom-in picture indicates the end face while the white portion of this picture refers to the surface side of column. The summation process in Equation ?? gives the following equation around node 6:

$$\begin{aligned} \dots = & \dots + [q_{10.3}^6 S_{3,6.10} + q_{49.3}^6 S_{3,6.49} + q_{50.2}^6 S_{2,6.50} \\ & + q_{67.1}^6 S_{1,6.67} - q_{67.1}^6 S_{2,6.67} - q_{67.1}^6 S_{3,6.67} \\ & + q_{68.1}^6 S_{1,6.68} - q_{68.1}^6 S_{2,6.68} - q_{68.1}^6 S_{3,6.68} \\ & + q_{80.2}^6 S_{2,6.80} + \dots] \end{aligned} \quad [5.13]$$

The notation of $q_{j,k}^i$ is that i refers to node number, j indicates the element number and k is the node order in the j element. For example, $q_{68.1}^6$ indicates the q value at node 6 which lies on the first node of element 68. And, $S_{i,m,n}$ is the value of kernel function S_i which the integration is performed on the base point m over element n . Thus, $S_{3,6.10}$ is the value of kernel function S_3 which is based on the base point 6 and integrating over element 10. In this example as shown on Figure 5.5, we have:

- node 12, 6, and 30 are corner nodes.
- node 5 and 29 are the nodes on the surface side of the jet.
- node 39 and 38 are the nodes on the end face of the jet.
- element 10, 49, and 50 lies on the surface side of the jet.
- element 68, 67 and 80 lie on the end face of the jet

According to our discussion and assumption, we have: By assumption:

$$q_{10.3}^6 = q_{50.2}^6 = q_{49.3}^6 = q^6 \quad [5.14]$$

By definition:

$$q_{67.1}^6 = q_{68.1}^6 = q_{80.1}^6 = 0 \quad [5.15]$$

Thus, Equation 5.13 becomes:

$$\dots = \dots + q^6 [S_{3,6.10} + S_{3,6.49} + S_{2,6.50}] + \dots \quad [5.16]$$

The last difference between the droplet case and jet case is that special attention is warranted on the corner nodes for the fitting process. The adjacent nodes around a corner node, which are used for the least square method, can not be used if they lie on the end face of the jet due to the dramatic change on the geometrical properties such as normal vector and curvature. In this case, the image points associated with the nodes on the surface side of the jet which are around a corner node are used. The result shown for the curvature for an undisturbed jet, the value of one are given on every corner nodes by using the image point method.

5.5 Nonaxisymmetric Modes

The initial shape of a liquid column is given by Equation 5.10. By varying the value of longitudinal wave number (k), transverse wave number (m), and perturbation magnitude (δ), one can see some asymmetric shapes due to the presence of the nonaxisymmetric mode.

Figure 5.6 shows the column shape for different m values at a given $k = 1$. The total column length is three wavelengths and $\delta = 0.2$. An axisymmetric shape is shown on the first picture of Figure 5.6 which $m = 0$. The radius of circular shape of cross section varies along with the longitudinal direction. This type of axisymmetric variation shape is called dilation or varicose mode. For the next picture of Figure 5.6, $m = 1$, the cross section of column is nearly circle and the size of cross section is constant along with the longitudinal direction. This shape is called sinuous or snake mode. It shows that the asymmetric mode is taking its effect on the formation of column shape. The cross section becomes elliptic for $m = 2$ mode on the third picture of Figure 5.6. And the m lobes shape will appears on the cross section when different values of m been applied.

For the $m = 1$ mode on the Figure 5.6, there is an interesting shape variation when the perturbation magnitude varies. Figure 5.7 shows four cross section pictures for four different perturbation magnitudes. The original nearly circular shape at $\delta = 0.2$ becomes to squeeze at the bottom of nearly circular shape when δ increases. This clearly shows an example of non-axisymmetric deformation.

Figure 5.8 shows the cross section and column shape for $m = 2$ mode when perturbation magnitude is increased. The development of two lobe shapes from the cross section becomes clearer when δ is increased. At large δ , the column shape just like a two cylindrical columns twisted together.

Figure 5.9 show the cross section and column shape for $m = 3$ mode at increasing perturbation magnitude. The three lobe shape shown on the cross Section as the characteristic of the third transverse mode oscillation. At large δ , the column shape looks like three cylindrical columns twisted together.

5.6 Results of Linear Analysis

The mathematical model developed by Yang and described in section 5.2, is used for the temporal instability analysis on a liquid jet which is assumed as incompressible, inviscid, and quiescent fluid. The dispersion Equation 5.9 serves as the analytical solution for the growth rate. The analytical solution is used to compare to the results from 3D BEM model. The calculation of growth rate for the numerical result is based on the derivation by Mansour [6] which he utilized the prediction of Rayleigh's analysis. The extension of derivation by Mansour for 3D jet is described as follow.

The development of jet is assumed to be in the form of:

$$r = 1 + \delta \cos(kz + m\theta) \cosh(\alpha_r t) \quad [5.17]$$

where α_r is the growth rate which is the real part of α which is defined previously. And, the velocity in radius direction (V_r) is calculated by:

$$V_r = \frac{dr}{dt} = \delta \cos(kz + m\theta) \sinh(\alpha_r t) \alpha_r \quad [5.18]$$

Thus the growth rate α_r is given by:

$$\alpha_r^2 = \frac{V_r^2}{(r-1)^2 - \delta^2 \cos^2(kz + m\theta)} \quad [5.19]$$

Since the only unstable wave in the incompressible, inviscid, and quiescent fluid is the axisymmetric wave, m is set to be zero. Along the longitudinal direction, the nodes lying on the trough of wave are chosen to be the location which the temporal analysis is conducted (thus $kz = \pi$). Therefore, the preceding equation is simplified to the equation which was used in the Mansour's analysis which is given by:

$$\alpha_r^2 = \frac{V_r^2}{(r-1)^2 - \delta^2} \quad [5.20]$$

In this case, only the axisymmetric wave develops, the nodes on the surface side of jet will move only in the radial direction and V_r is given by q which is calculated by 3D BEM model. Thus, the temporal instability analysis for axisymmetric oscillation can be conducted based on Equation 5.2 for analytical solution and Equation 5.20 for numerical solution.

The temporal instability analysis is performed by picking several longitudinal wave numbers (k) and letting transverse wave number (m) to be zero for axisymmetric case. The total wavelength is set to be one. A single grid setup is not appropriate to run this analysis due to the aspect ratio of grid element varying for different values of k . Figure 5.10 shows the grid setup with $int_z = 40$, $int_{\theta} = 10$, and $int_r = 3$ for three different k values: $k = 0.3$, $k = 0.7$ and $k = 0.9$. The aspect ratio $\Delta\theta/\Delta z$ will increase when Δz decreases due to increasing k values. Note that $\lambda = 2\pi/k$ and $\Delta z = \lambda/int_z$. The total length of jet is chosen to be one which results in a large aspect ratio for higher k value. The shape of jet will look bigger for those higher k values due to the higher aspect ratio. A grid setup with nonuniform aspect ratio for element will affect the accuracy of results. In order to get better results, the optimized grid needs to be used for each k value.

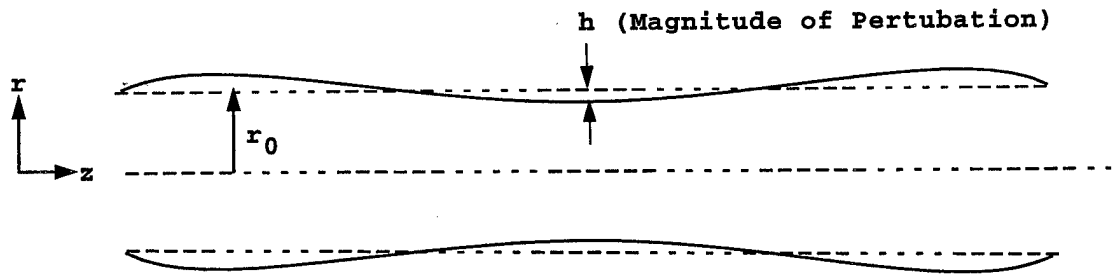
Figure 5.11 shows that the growth rate calculated by 3D BEM model reaches the growth rate predicted by Equation 5.9 when grid setup approaches the optimized grid for $k = 0.7$.

The growth rate converges quickly to a constant. The same behavior will show for different k values. The convergent constant will be the desired value of growth rate.

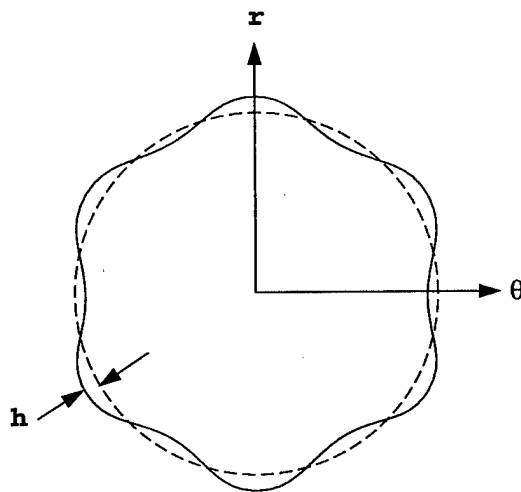
Figure 5.12 shows the same plot for $k = 0.9$. We see that the track of growth rate vs. time comes down to the predicted value when a finer grid is used. The finest grid been tested ($int_z = 70, int_{the} = 10, int_r = 3$) results in 752 nodes and 1500 elements on the surface. The even finer grid can not be used in our computer facility due to the shortage of memory. However, the convergence behavior is shown on Figure 5.12 when the fine grid is implemented. We may expect that the computed results will finally agree with the predicted values when the very fine grid is used. Figure 5.13 shows the growth rate vs. time for three different k values at their optimized grid setup. These curves all converge to their corresponding constant value.

Figure 5.14 shows the comparison of computational results and predicted values for linear analysis. It shows a very good agreement for $k = 0.3, 0.5$ and 0.7 . The reason for error for $k = 0.9$ may due to the desire of even fine grid for the computational domain.

The linear analysis shows that the predicted growth rate for a liquid column without the presence of gas phase are matched very well with the computational results from 3D BEM model. Thus, the validation of 3D BEM model is completed.



Perturbation in r - z plane



Perturbation in r - θ plane

Figure 5.1 Perturbation on r - z and r - θ plane of an Infinite Liquid Jet

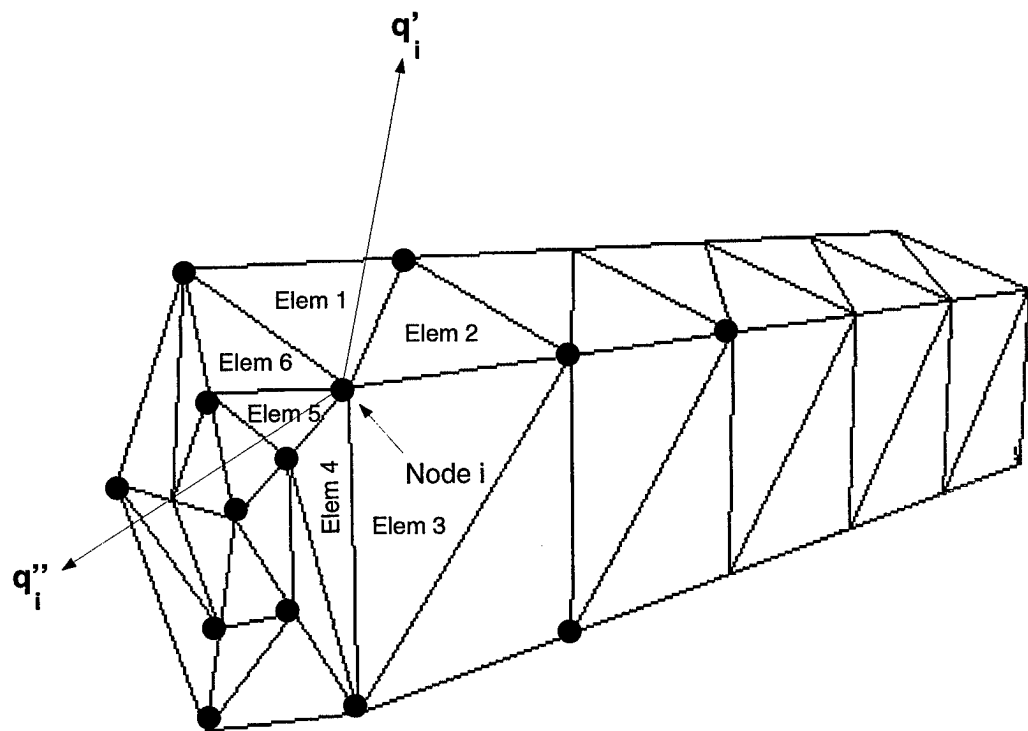


Figure 5.2 Multiple Values of Normal Velocities at a Corner Node

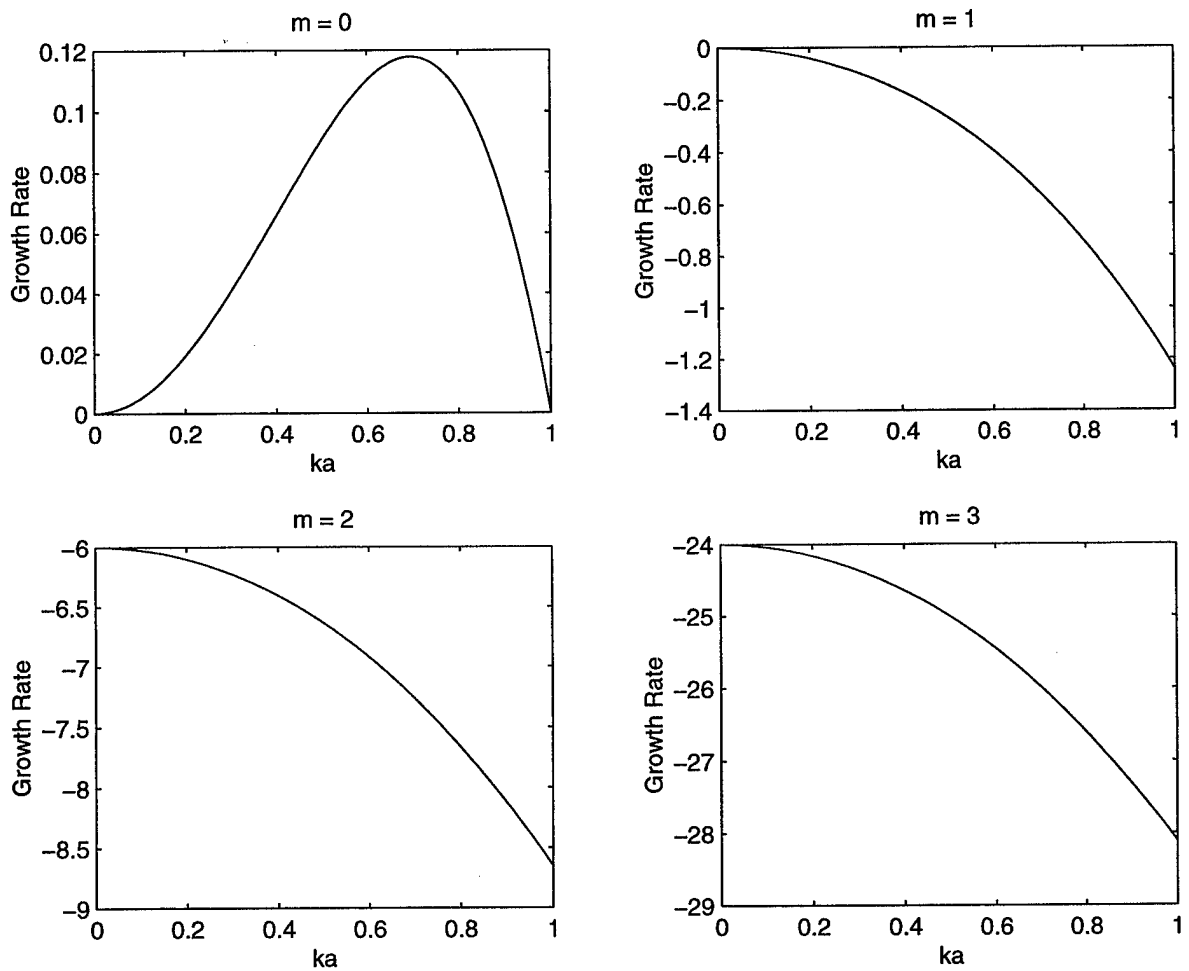


Figure 5.3 Growth Rate ($(\alpha_r^*)_m^2$) vs Dimensionless Streamwise Wave Number (ka) at Different Azimuthal Wave Number (m)

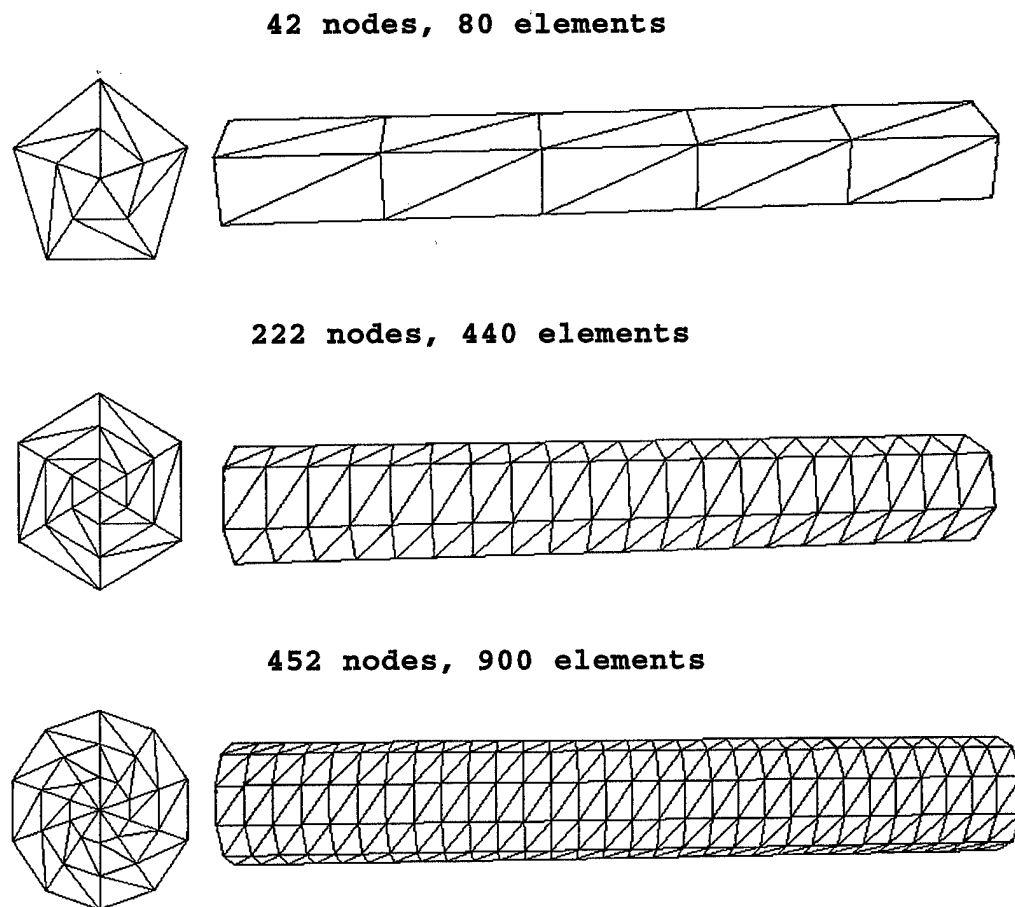


Figure 5.4 Three Different Grid Setups for a Liquid Jet

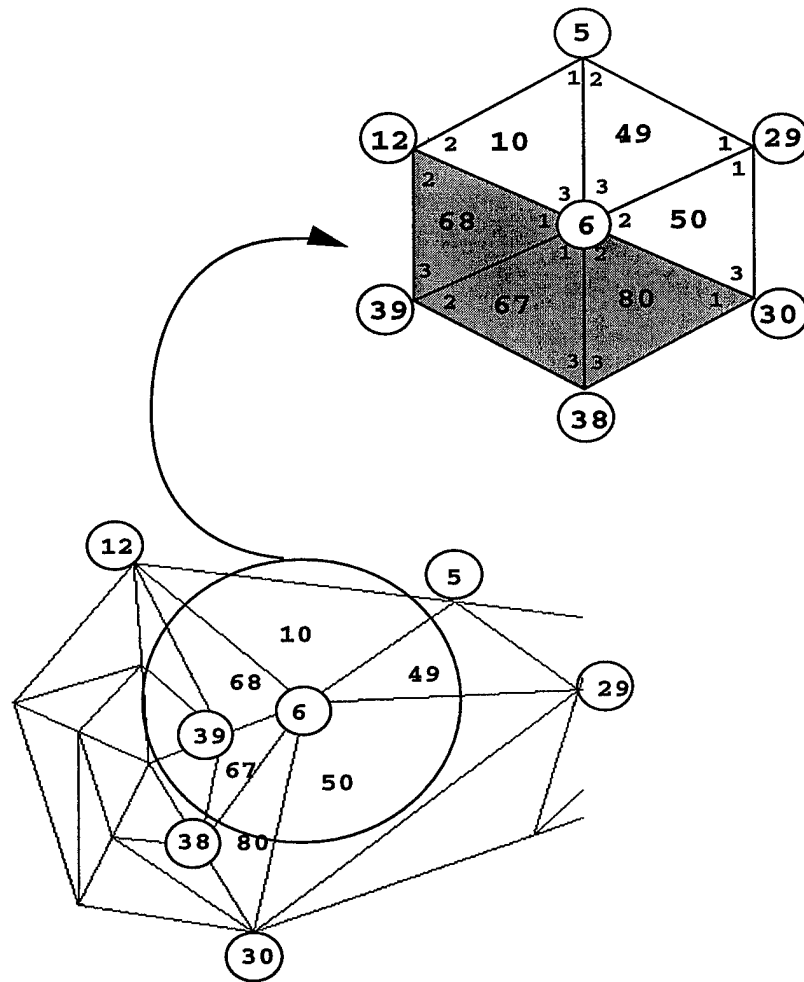


Figure 5.5 Schematic Description of Surrounding Grids and Elements Around a Corner Node

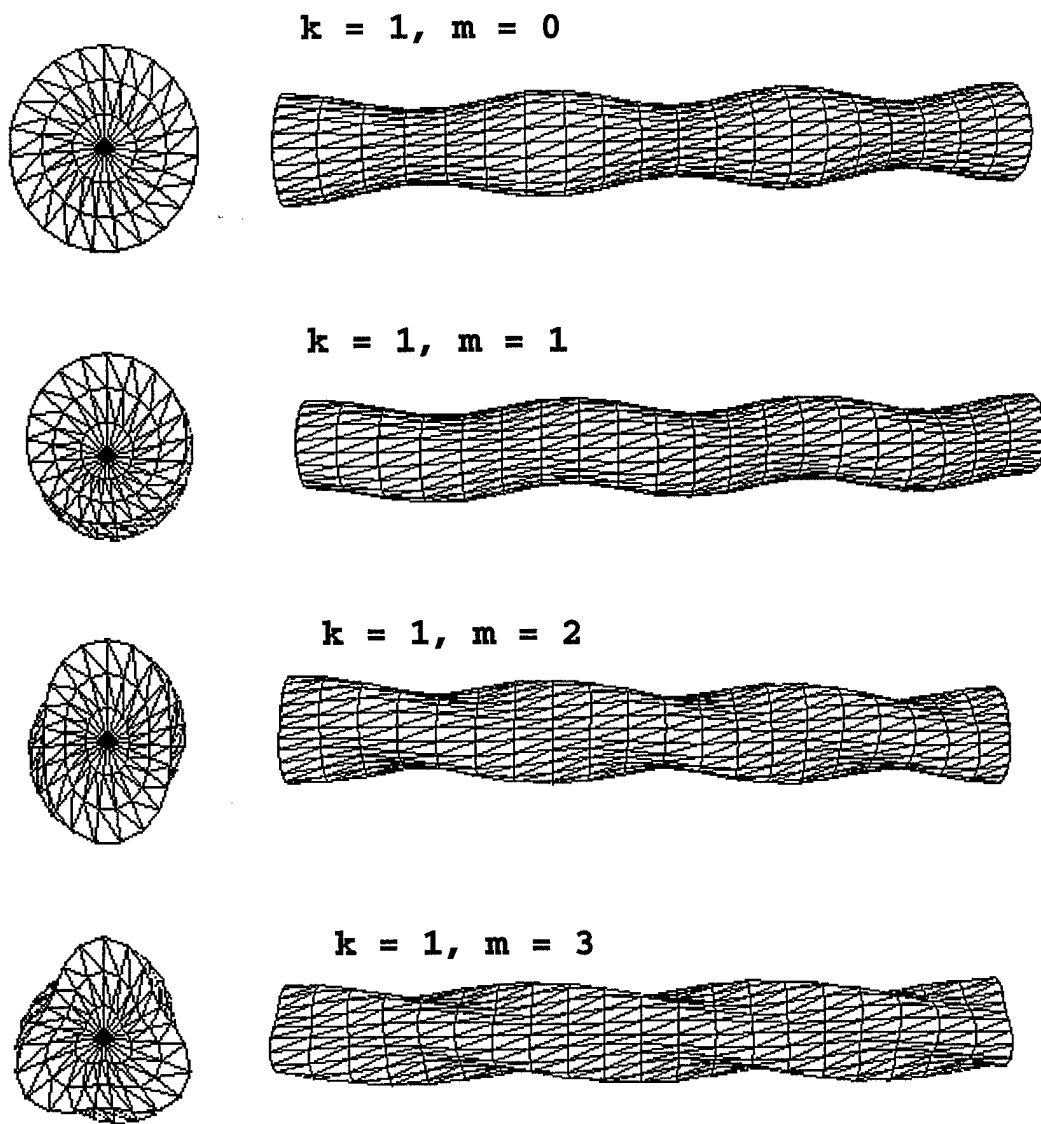


Figure 5.6 Effect of Transverse Modes 2: $\delta = 0.2$, Total Length = 3λ

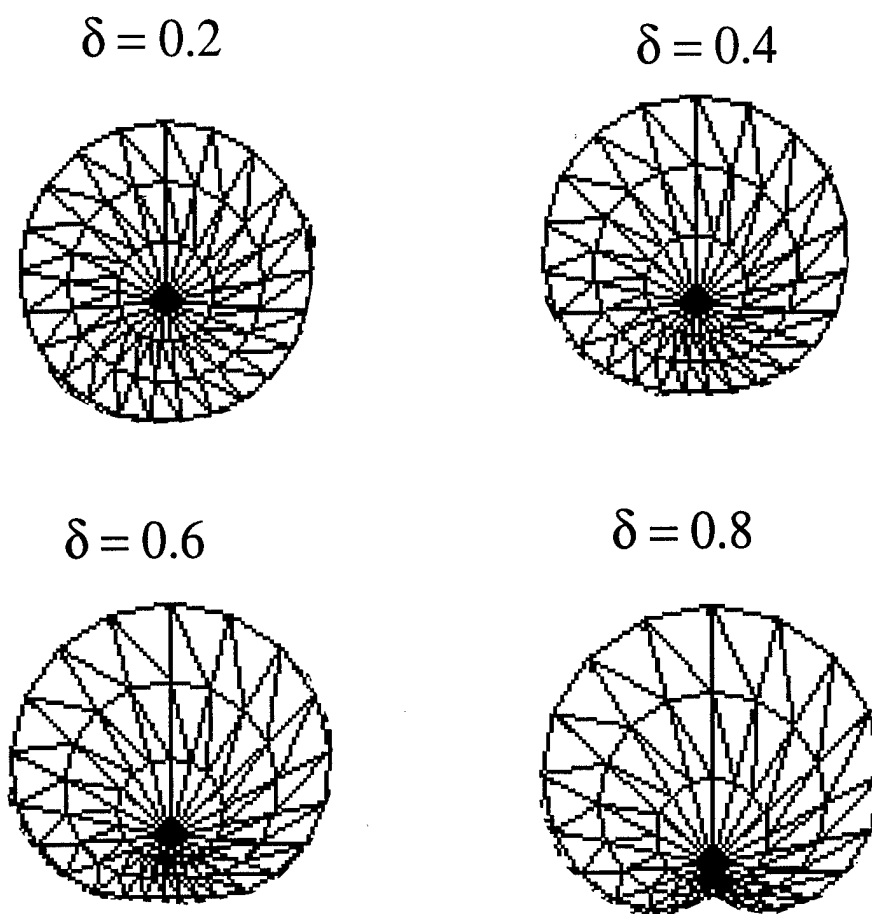


Figure 5.7 Effect of Perturbation Magnitude on Transverse Modes $m = 1$ Mode: $k = 1$,
Total Length = 3λ

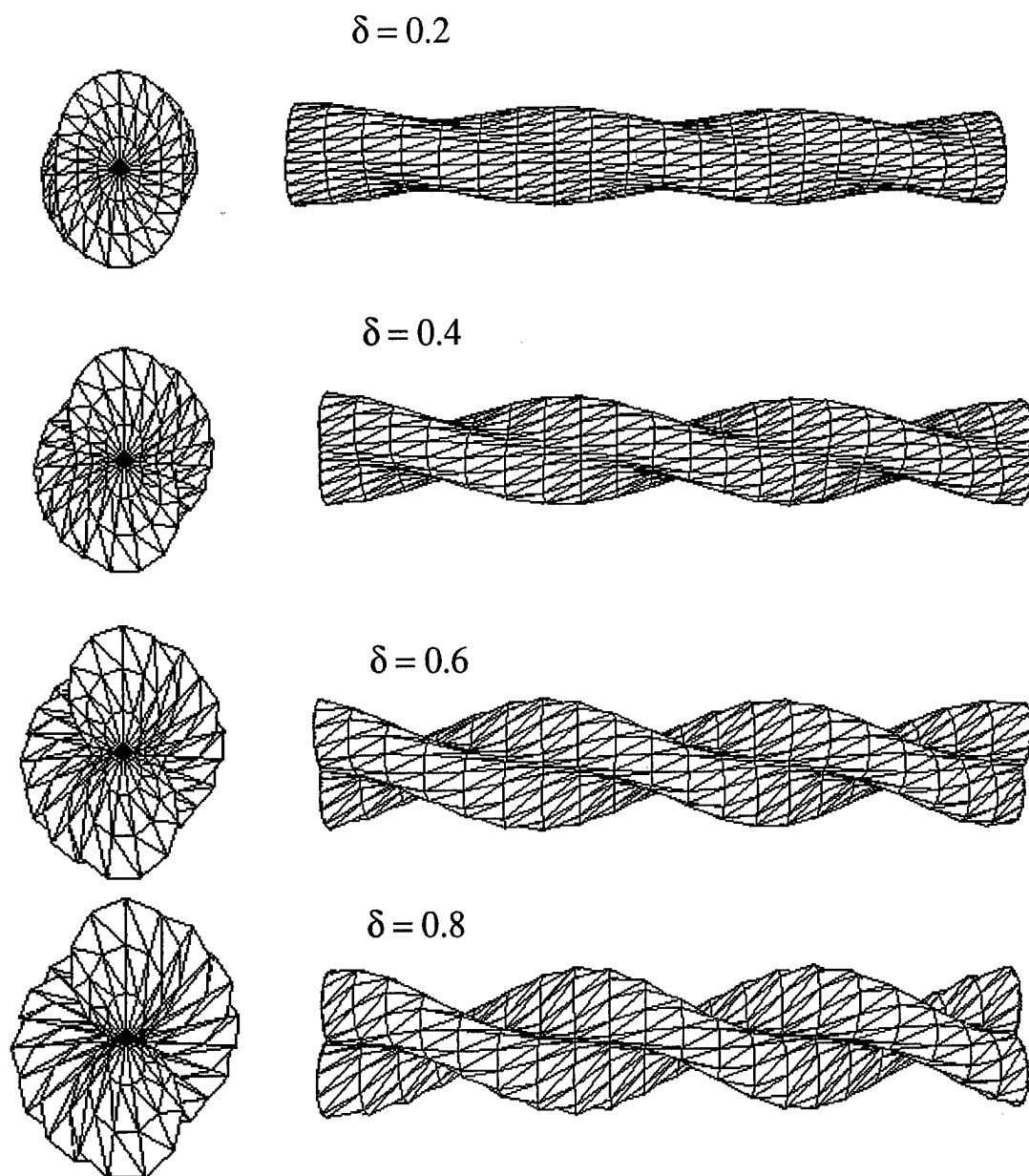


Figure 5.8 Effect of Perturbation Magnitude on Transverse Modes $m = 2$ Mode: $k = 1$,
Total Length = 3λ

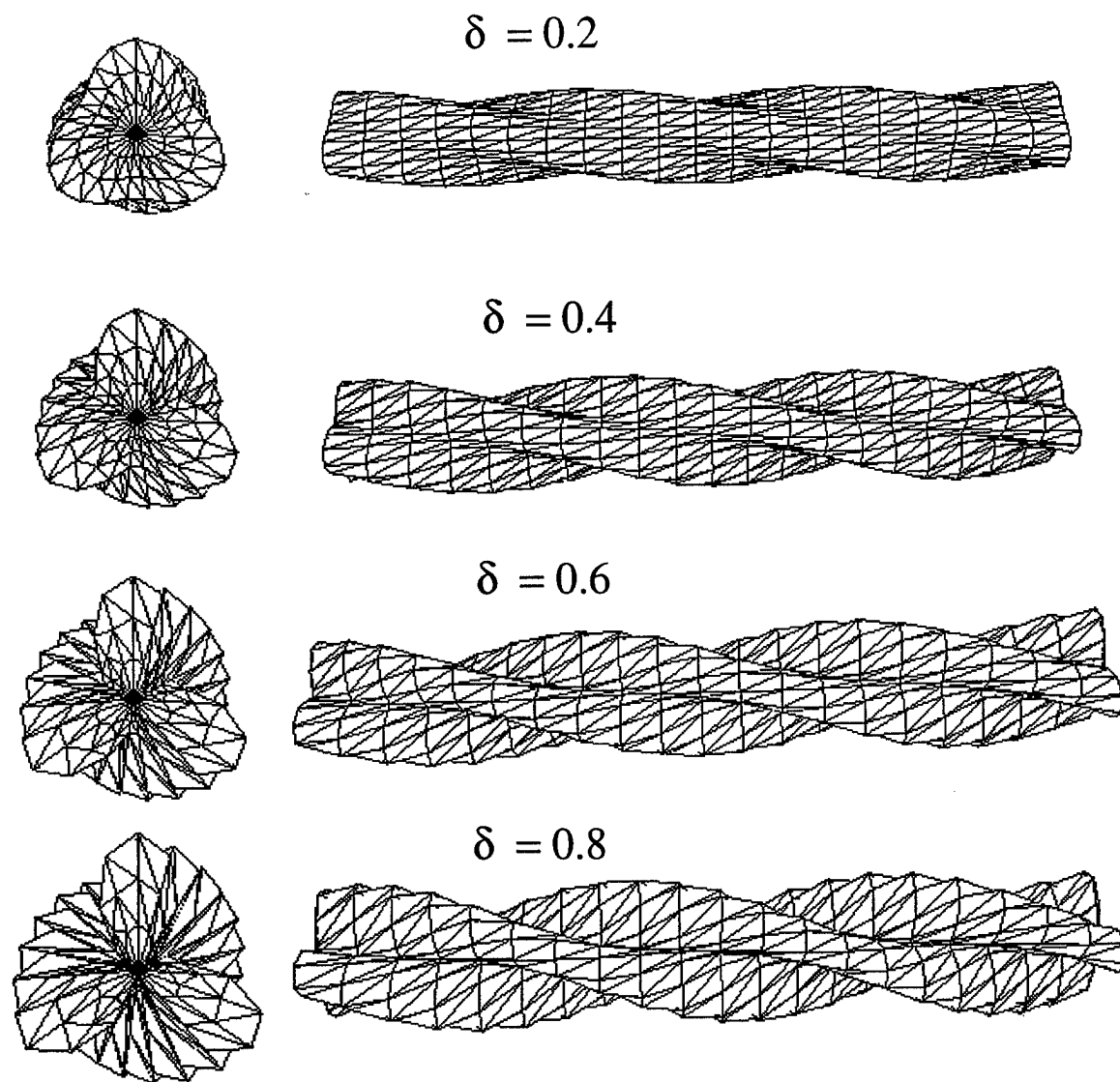


Figure 5.9 Effect of Perturbation Magnitude on Transverse Modes $m = 3$ Mode: $k = 1$,
Total Length = 3λ

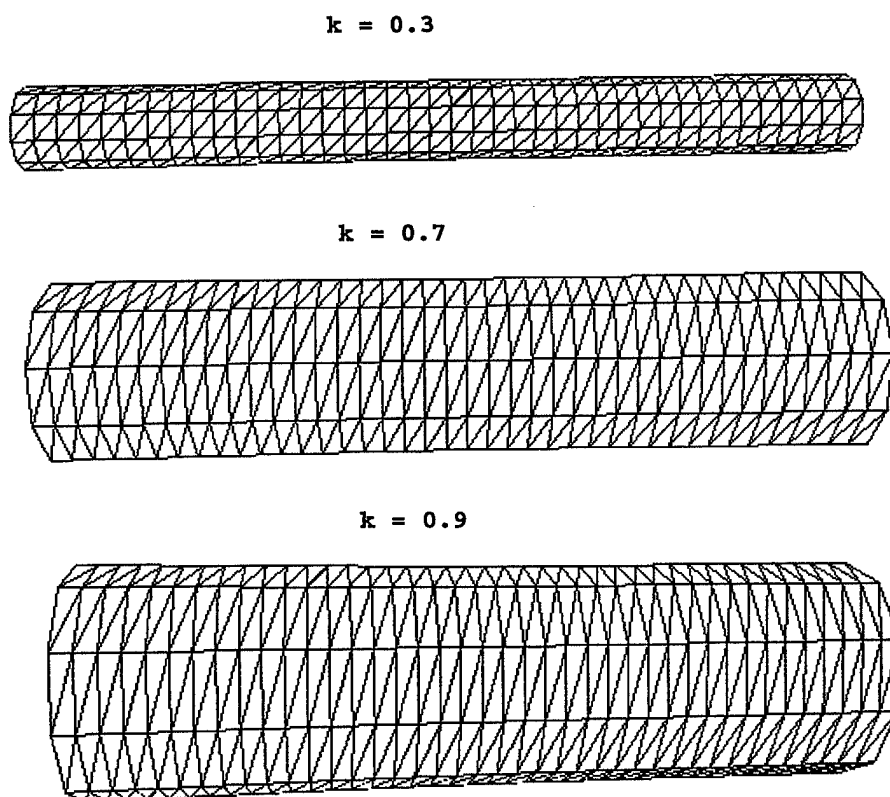


Figure 5.10 Same Grid Set-Up ($int_Z = 10$, $int_The = 10$, and $int_R = 3$) for $k = 0.3, 0.7$, and 0.9 . Perturbation Magnitude is 0.01 for $m = 0$.

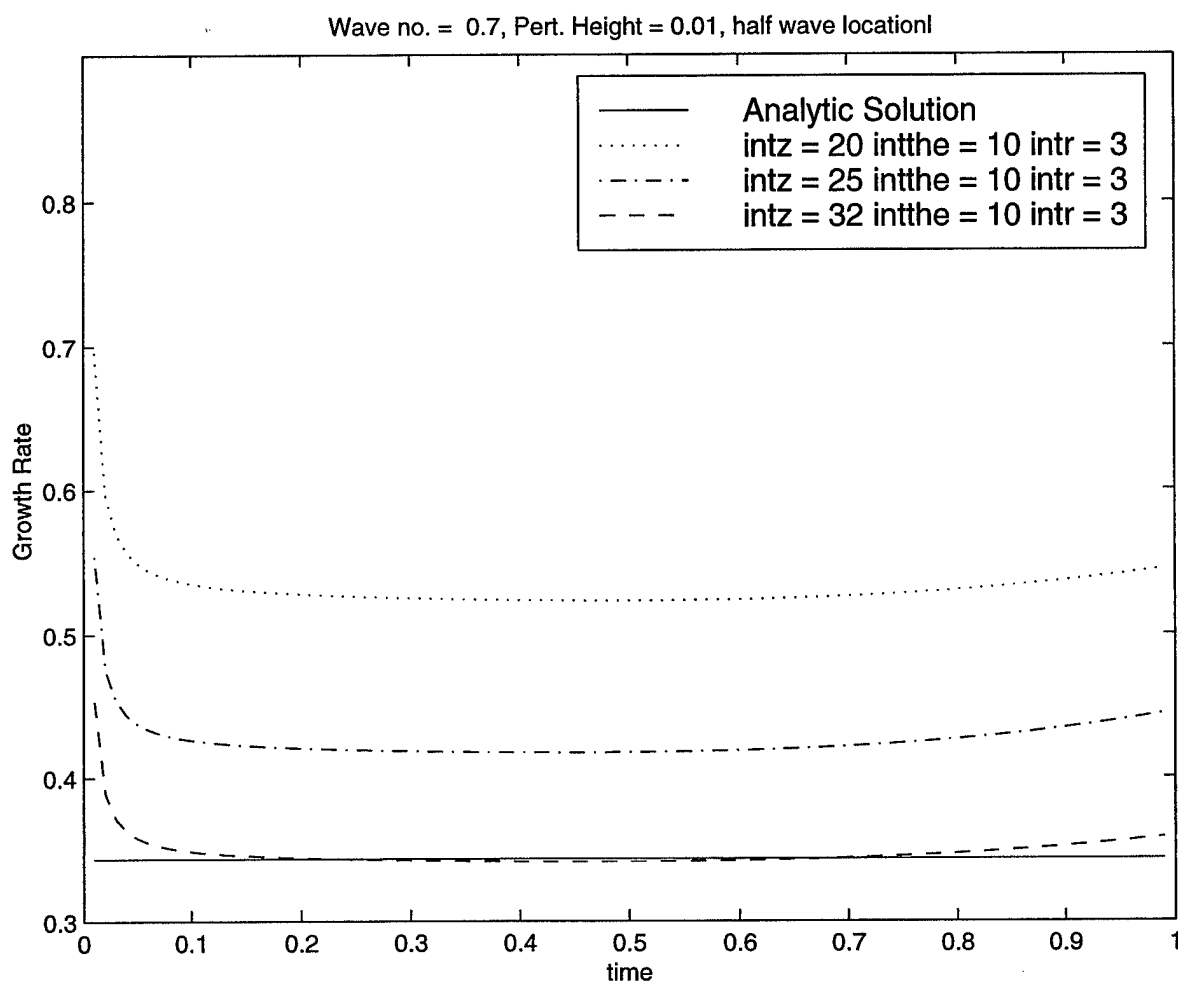


Figure 5.11 Track of Growth Rate with Time for $k = 0.7$, Perturbation Magnitude = 0.01

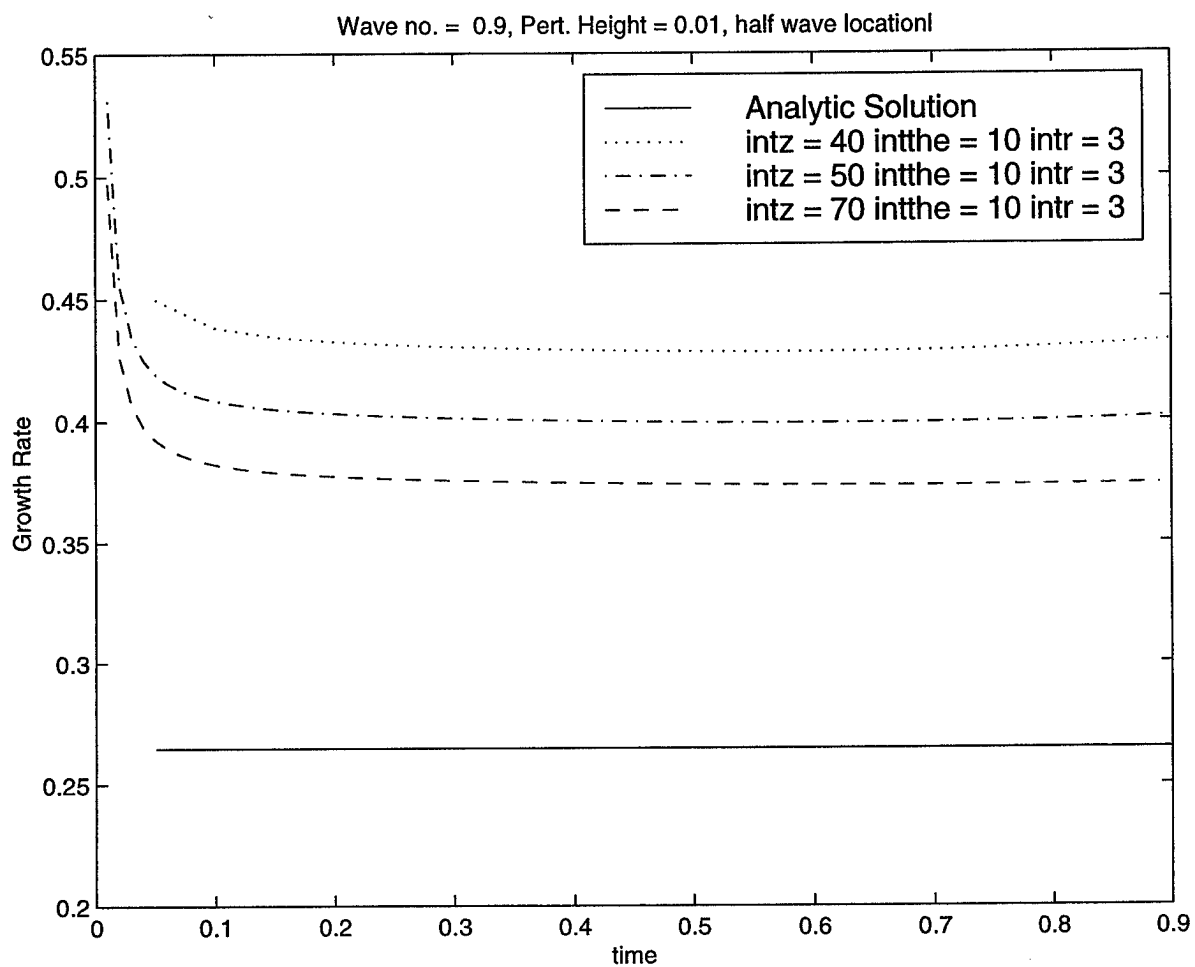


Figure 5.12 Track of Growth Rate with Time for $k = 0.9$, Perturbation Magnitude = 0.01

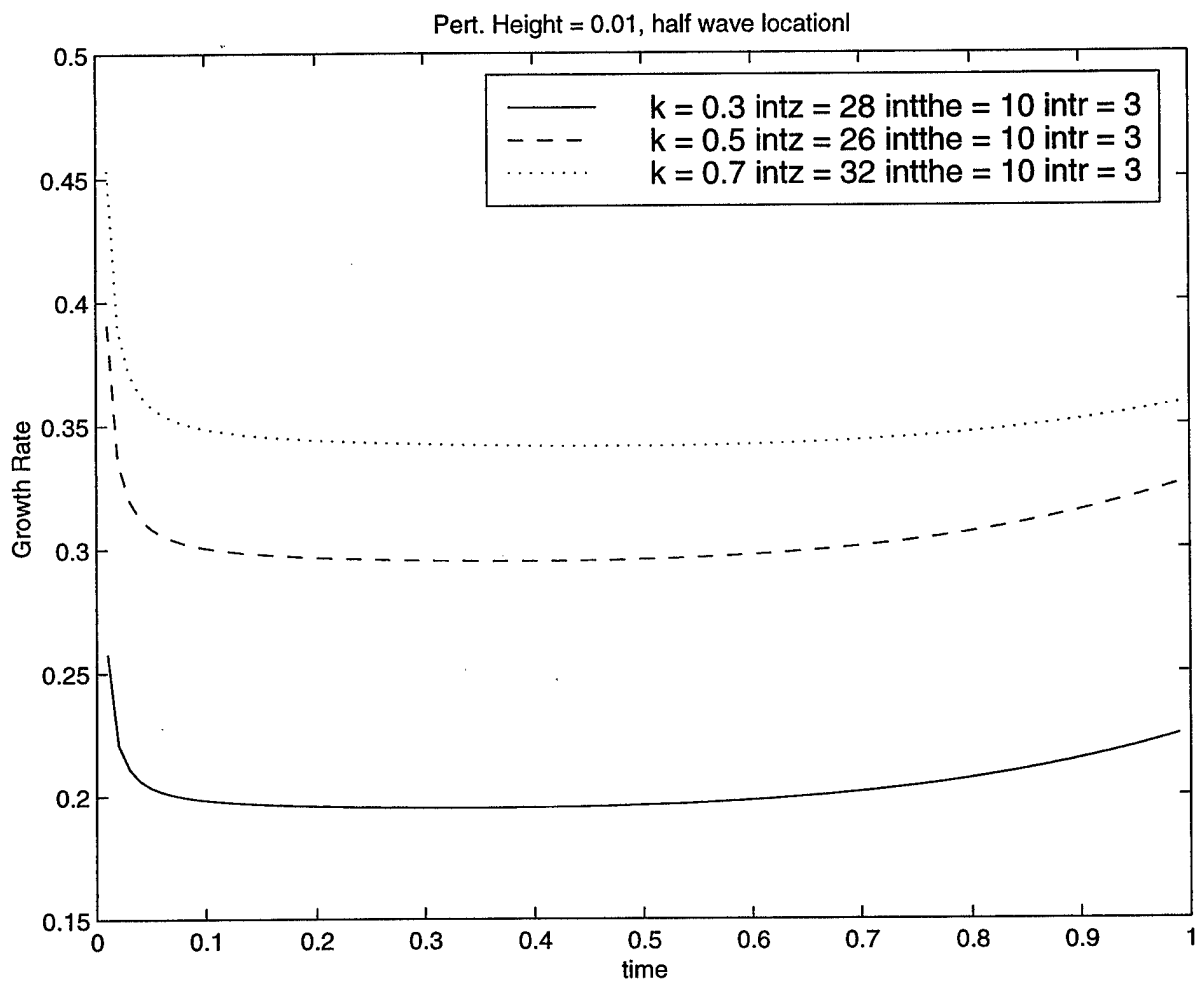


Figure 5.13 Track of Growth Rate with Time for Three Different k values at Their Optimized Grid Setup

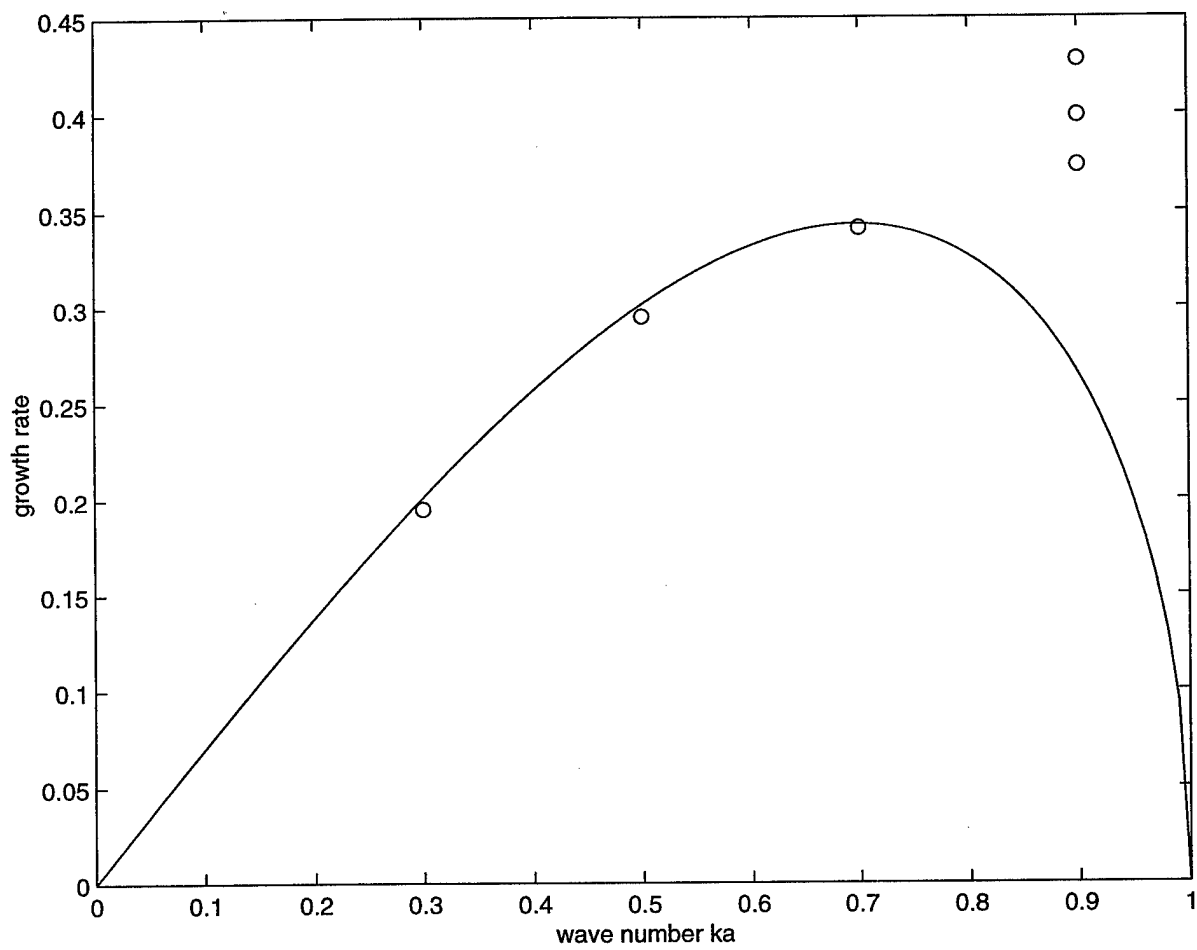


Figure 5.14 Comparison of Analytic and Numerical Solution for Linear Temporal Analysis: Perturbation Magnitude = 0.01

9 Appendix E - Dense Spray Model Description

Heister, S. D., "Modeling Primary Atomization Processes", AIAA 98-3837, 34th AIAA Joint Propulsion Conference, 1998.

MODELING PRIMARY ATOMIZATION PROCESSES

S. D. Heister *

January 28, 1999

Abstract

This paper summarizes recent progress in modeling complex atomization and injector internal flow processes using a variety of numerical techniques. This program has been developed under AFOSR sponsorship with the goal of characterizing the contributions of atomization processes to combustion instabilities in liquid rocket engines. Complete viscous, unsteady simulations of spray formation (including the dense spray region) should be available within the year.

Introduction

In a liquid rocket engine (LRE) combustion chamber, the atomization process serves as a precursor to complex vaporization, mixing, and reaction processes. Not only is the atomization process important to characterizing the steady-state performance of a LRE, but it also can play an important role in unsteady processes within the combustion chamber. In fact, numerous authors¹⁻⁵ have implicated the atomization process as a mechanism to (at least partially) explain high-frequency LRE combustion instabilities.

Even under steady conditions, our knowledge of the detailed processes leading to atomization of a liquid jet is quite modest. For this reason, there have been relatively few efforts aimed at improving our understanding of injection processes under dynamic conditions. Most previous efforts have been experimental in nature and have been motivated by LRE combustion stability concerns. Under AFOSR sponsorship, a series of two-dimensional, nonlinear models⁶⁻¹² have been developed to ascertain the influence of unsteady chamber conditions on basic atomization processes. These models utilize Boundary Element Methods (BEMs) to provide high resolution

surface shapes approaching *and beyond* actual atomization events.

As a result of these developments, we have been able to quantify the dramatic effects chamber unsteadiness can have on droplet sizes and distortion of liquid jets/columns emanating from impinging element injectors. In addition, viscous simulations have revealed that a "swelling" of the free surface takes place immediately outside the orifice exit. This phenomena, which has been observed in the die-cast industry, is attributed to boundary layer rearrangement due to the transition from a no-slip to a free-surface boundary condition. Results indicate the degree of swelling is directly proportional to the boundary layer thickness at the exit of the orifice. In fact, this conclusion helps us understand the role of orifice passage design in affecting subsequent atomization processes.

Recognizing the importance of the internal flow to the atomization process, we have also developed models capable of addressing this flowfield. Efforts¹³⁻¹⁵ in this area have focused on the role of cavitation in influencing orifice passage flows. At the present time, we have a fully viscous, unsteady, 3-D capability to resolve either single or two-phase flows in these passageways. While cavitation may not be of critical interest in high pressure rocket engine applications, the two-phase flow methodology is useful in extending solutions to the spray region formed outside the orifice. The approach is based on a pseudo-density treatment in which the pseudo-density varies in magnitude between the liquid and vapor (or gas) extremes. By developing a constitutive relation for the pseudo-density, one can investigate a variety of two-phase flows.

In this paper, we will highlight recent developments of a 3-D BEM tool capable of solving more general atomization problems. In addition, we will briefly describe the pseudo-density modeling approach and highlight a new model capable of resolving the entire spray (including dense spray region) while accounting for gas entrainment and momentum transfer between phases.

*Associate Professor, Associate Fellow AIAA
Purdue University, West Lafayette, Indiana, 47907,
Copyright © 1998 by the American Institute of Aeronautics
and Astronautics, Inc. All rights reserved.

Boundary Element Modeling

During the past two years, we have been developing a fully three-dimensional capability to simulate complex fluid surfaces under arbitrarily-large distortions. Originally, these developments were undertaken with Professor Chandrajit Bajaj of our Computer Science department. Professor Bajaj's group had agreed to implement some of their surface tracking/regridding strategies, while our group focused on the development of the fluid flow solver. Unfortunately, Professor Bajaj left Purdue for a position at the University of Texas in January of this year; for this reason, we had to substantially rescope the efforts.

During the past year, we have developed a fully 3-D, unsteady flow solver using linear Boundary Elements, as well as computational mesh generation capabilities for droplet and liquid jet geometries. Figure 1 highlights computational meshes generated for droplets via interpolation from octahedron polygons. This general technique can also be applied to arbitrary initial fluid/structural shapes. Using the octahedron grid generation package, simulations were performed for droplets oscillating in 2nd, 3rd, and 4th modes. An example simulation result is shown in Fig. 2 for a 3rd mode oscillation. Computed frequencies agree well with those in the literature for linear/nonlinear droplet oscillations. Further validation was conducted on the droplet case to insure that solutions were independent of grid. Furthermore, a rather exhaustive study was completed to insure convergence of all the complex integrals involved in the 3-D BEM.

Having validated the model, we set out to study the nonlinear stability of an infinite liquid jet. The infinite-jet assumption leads to periodic boundary conditions on a computational domain involving a single wavelength of a temporally-evolving instability. The use of a single wavelength reduces the size of the domain dramatically, but introduces substantial complications as a result of corners created at the ends of the wave. A typical computational mesh is depicted in Fig. 3; a structured triangular mesh was generated in this case. Using this mesh, we have evaluated the model against analytic results which predict the growth rate of an instability of a given wavelength.

Figure 4 provides a comparison of these results for axisymmetric instabilities imposed on an axial wave with wavenumber k . The solid curve represents the analytic result¹⁶, while the BEM calculations are shown as symbols on the plot. Computational resources constrained us to fairly coarse grids including 20-40 axial nodes and 10-20 circumferential nodes on

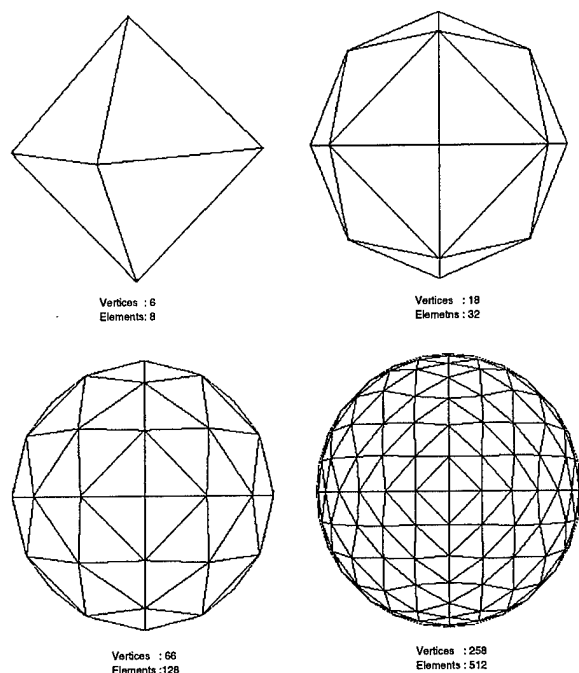


Figure 1: *Computational Mesh Generated from Octahedron Interpolations for use in Droplet Oscillation Simulations*

the interface. As a result of these coarse meshes, substantial disagreement is noted between model results and analytic solutions. In addition, the results point to the need for improved surface fitting (our current approach provides local fitting with a second-order polynomial after Chahine, et. al¹⁷). Since an advanced surface fitting and regridding capability has not been included due to the departure of Dr. Bajaj, the present model does not have the capability to handle large surface distortions. In the future, we hope to develop this capability ourselves.

Another area to be explored in the near future is the simulation of a pressure-swirl atomizer such as those used in numerous cryogenic and Russian rocket engines. These axisymmetric simulations will be explored through modifications of existing finite-length liquid jet codes. Orifice geometry, swirl velocity, fluid properties, and general unsteady inflow conditions can effectively be considered in the simulations. We expect to have simulations of this flow by the end of 1998.

Viscous, Two-Phase Flow Simulations

There is a critical need for a model capable of addressing fully coupled spray dynamics in which momen-

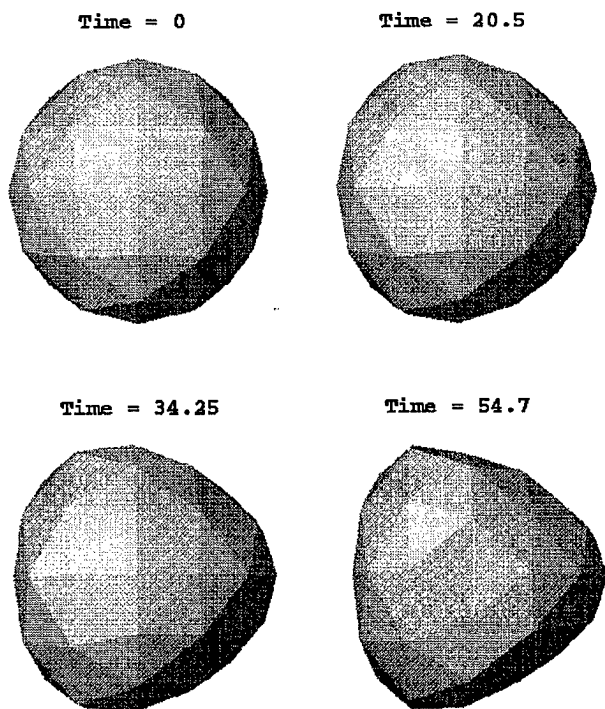


Figure 2: *Droplet Shapes at Various Times; 3rd Mode Oscillation*

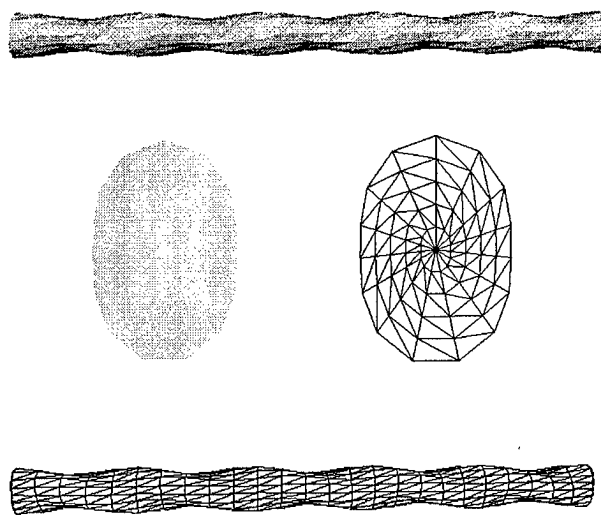


Figure 3: *Computational Mesh for Simulations of Nonlinear Stability of Infinite Jet*

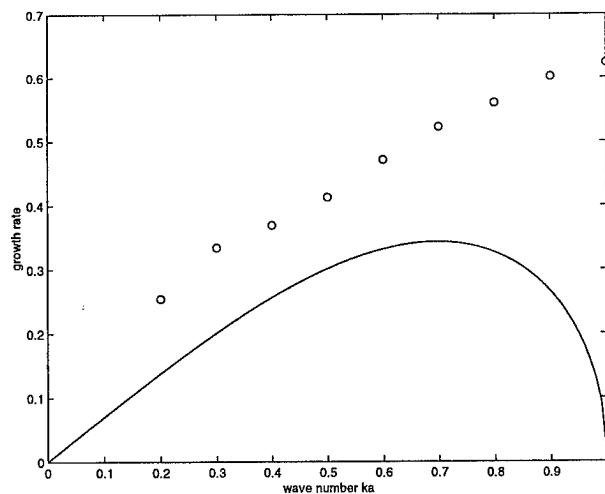


Figure 4: *Replication of Analytic Growth Rates Using the Infinite Jet BEM. Here, ω is the Growth Rate, k is the Axial Wavenumber, and n is the Circumferential Wavenumber*

tum transfer between phases is handled in an implicit fashion. Models based on linear theory are known to be inaccurate, yet full multidimensional simulations are well beyond computational capabilities. What we really desire is a mechanism to obtain averaged flowfield conditions which are a reflection of the local droplet number density (or local “void fraction”) without having to compute the flowfield around all the individual droplets. Models of this type have been in use for many years in assessing two-phase bubbly flows. Recently, models of this type have been successfully developed to assess unsteady behavior in cavitating flows. The models are based on a *pseudo-density* formulation, and are sometimes referred to as “single-fluid” models. Here, the pseudo-density is a fictitious parameter which varies between the liquid and gas density extremes. i.e. a pseudo-density value midway between liquid and gas densities would be representative of a mixture which is 50% liquid and 50% gaseous.

Cavitating Internal Orifice Flows

The single fluid models are powerful in that they are capable of performing fully viscous, unsteady calculations for complex two-phase flows. The main challenge in using this methodology stems from the fact that there is no equation of state which defines the fictitious pseudo-density. Therefore a constitutive relation for this parameter must be developed based on the characteristics of the two-phase flow. In cavitating flows, we have been successful in deriving a con-

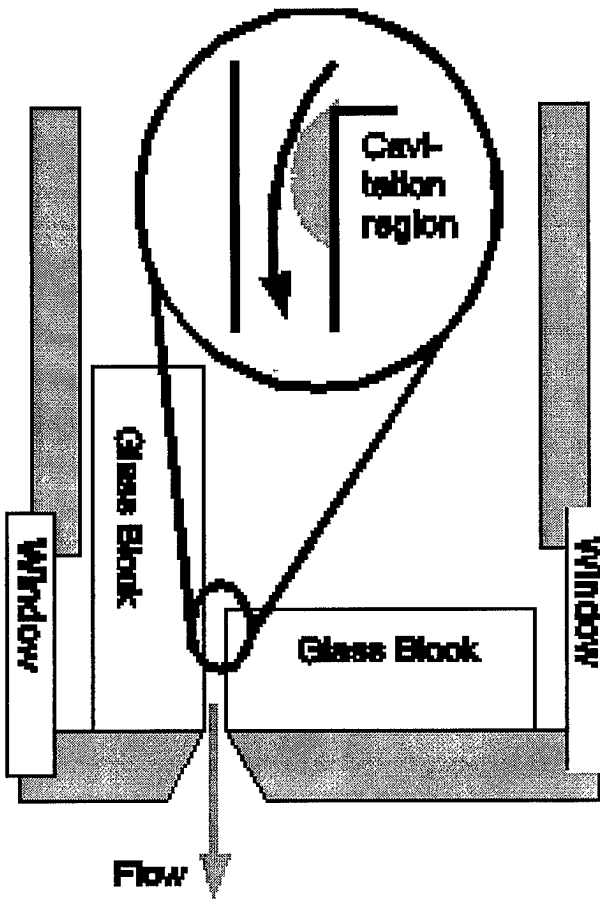


Figure 5: Schematic of 2-D Slot Experimental Apparatus¹⁸

stitutive relation for the pseudo-density based on the response of a single bubble to a time-varying external pressure (Rayleigh-Plesset equation). Using this approach, we have developed a time-dependent relation for the pseudo-density which is reflective of local flow-field conditions and the pressure history encountered by a given bubble.

Using this implementation, we have successfully modeled complex, unsteady cavitation processes in both external and internal flows. Recent simulations have focused on a 2-D slot flow in order to validate computations against recent experimental data obtained by Henry¹⁸. Figure 5 provides a schematic representation of the experimental apparatus used to obtain a single, unambiguous cavitation surface off the lip of a single slot.

Figures 6 and 7 provide some sample comparisons of the model with the experimental data. In Fig. 6, we compare the overall length of the cavity as a function of the imposed pressure drop for a slot

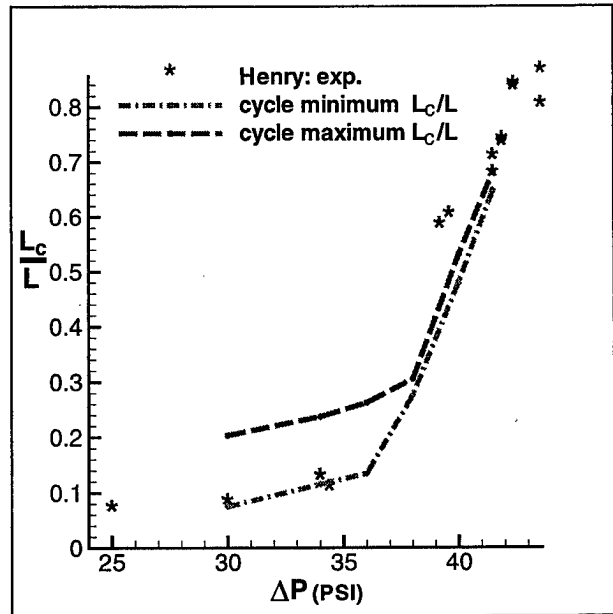


Figure 6: Comparison of Cavitation Length with Experimental Data of Henry¹⁸

with $L/D = 10.7$. Since the flowfield tends to be unsteady, we have included both minimum and maximum lengths obtained in the numerical simulation with Henry's data which was obtained at a given instant in time. Overall, the agreement is quite good considering the complex, turbulent cavitation processes which are evident in the experimental images.

A comparison with an actual image is shown in Fig. 7. Here, pseudo-density contours of 0.24, 0.49, 0.74 and 0.99 (from inside to outside) are shown in the broad white lines in the image. Once again, the computed flow is quasi-periodic, so the comparison is made for just one instant in this process; there is no way to correlate the timing with the single experimental image. In spite of this fact, comparisons using other points in the periodic process are quite similar. The model predicts two smaller regions of cavitation while the experimental data reveals a single large image. Overall, the extent of cavitation is predicted well. Turbulence effects, which are not modeled in the present code, are a probable explanation for the observed discrepancies.

Future Work - Dense Spray Model

While the pseudo-density formulation can be employed when the gas is the disperse phase, we must provide an alternate constitutive relation for ρ when the liquid is the disperse phase (as in the case of a spray). Since ρ is simply a reflection of the local liq-

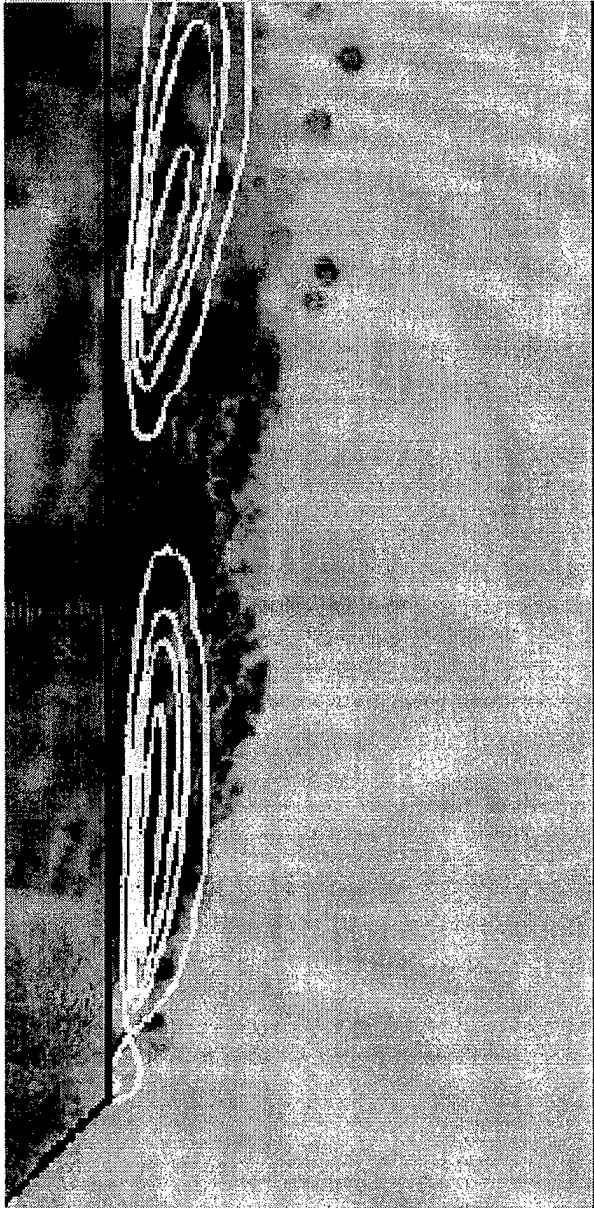


Figure 7: Comparison of Pseudo-Density Contours (in white) with Experimental Image for $\Delta P = 38$ psi, $L/D = 10.7$. Here, the Flow Direction is Upward and Outermost Density Contour Corresponds to $\rho = 0.99$.

uid volume in a given sample space, we could provide a straightforward calculation of pseudo-density if we knew the location and size of all the droplets in the flow. However, since there are too many droplets to track each one individually, we must consider a subset of the total droplet field with which to perform our calculation. If we presume that the spray can be represented by several discrete planes of droplets, each with identical characteristics, we could effectively compute pseudo-density by considering the dynamics of the droplets lying in just one of these planes. This procedure amounts to the presumption that the spray is “quasi-axisymmetric”; that the droplet sizes and velocities are similar in any azimuthal plane intercepting the main axis of the spray. Numerous experiments indicate that such a symmetry exists for nozzles, especially for the predominate case where the orifice passage is axisymmetric.

The unique treatment of a quasi-axisymmetric droplet field will provide the capability to track a manageable number of droplets in a single plane. While there is little research in the dense sprays arena, much is known about the dynamics of single droplets and groups of droplets. In recent years, we have seen advancements in knowledge of droplet collisions^{19,20}, secondary atomization^{21–24}, evaporation^{e.g., 25–28} behavior in both steady and unsteady environments, and a wealth of knowledge regarding group combustion and dynamics. It makes good sense to fold this knowledge into a comprehensive formulation for an entire spray. The recent development of pseudo-density codes and the vast research on droplet dynamics provides a unique opportunity for the development of the first comprehensive spray model.

Initial Conditions

Prescribing a set of well-posed initial conditions is always problematic in spray modeling. The most natural approach would simulate the opening of a valve and the motion of the initial slug of fluid through the orifice passage. However, this option is not viable using the current methodology since the complex interface tracking would introduce substantial complications to the envisioned algorithm. Moreover, using this approach, one would have to perform very long (and costly) calculations in order to reach a quasi-steady condition in the spray.

Given this state of affairs, we propose the geometry and initial conditions highlighted in Fig. 3. Basic inputs to the model include fluid properties, orifice diameter (D), injection velocity, (v_i), jet intact core length, (L_c), spray cone angle, (α), and initial

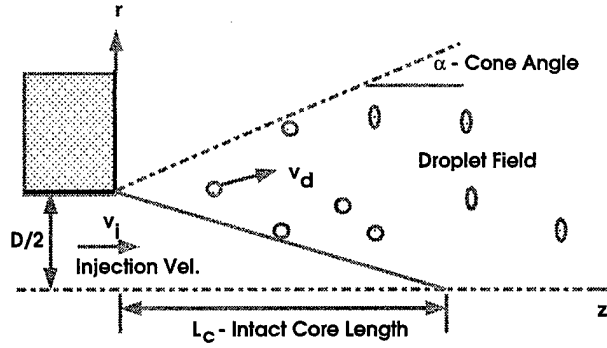


Figure 8: *Schematic Denoting Assumed Initial Conditions and Coordinate System for Quasi-Axisymmetric Model. Large Droplets of Uniform Size are “Launched” from the Conical Surface Shown. The Cone Angle, α , and Intact Core Length, L_c are Input from Experimental Observations*

droplet diameter, (d_i). Droplets are “launched” into the computational domain along the conical surface emanating from the lip of the orifice and terminating at the point $z = L_c$, $r = 0$. This approach is required since we intend to search for droplet collisions; there is insufficient surface area available at the exit plane to provide the proper massflux of droplets without having these droplets overlap. This is an important distinction, since simulations using the KIVA code²⁹ launch large “blobs” of fluid which represent large numbers of drops and overlap to a great degree in order to simulate droplet injection into the field.

The computational domain will include the edge of the conical surface bounded by a large cylinder. On the outer boundaries, constant pressure conditions can be assumed and velocities can be extrapolated from the interior of the domain. Individual droplets in the spray will pass through the “end” of the domain at a location, say, $z = z_{max}$. Spray statistics including droplet sizes and velocities can be obtained at this boundary for direct comparison with PDPA or Malvern experimental data. In fact, one can develop sets of spray statistics at arbitrary z locations using the proposed methodology.

Since the initial droplet size, d_i , cannot be readily determined from experimental or analytic means, there is a concern that this input may drastically effect the results. However, if we launch large drops, we can assure that all drops go through numerous secondary atomization and collision processes thereby making results less sensitive to this initial input.

Droplet Dynamics Module

Probably the most crucial element of our deterministic model of a fully-coupled dense spray is the response of individual droplets to the imposed flowfield. At the present time, no one has undertaken the arduous task of describing secondary atomization and collision processes for a dense spray. However, we believe the time is right for such a development for the following reasons:

- Recent work at Princeton provides a complete description of droplet collision/coalescence for both on and off-axis collisions of droplets composed of various fluids. These results can easily be incorporated parametrically into the proposed model.
- Recent work at Michigan and Wisconsin provides a quantitative description of secondary atomization process in terms of dimensionless parameters such as Weber and Ohnesorge numbers. Algebraic equations already exist for drop sizes resulting from the secondary atomization process, and effective drag coefficient data is also available from a variety of sources.
- Advances in computational power and parallel processing architectures make it possible to track tens, if not hundreds of thousands of individual droplets in a single calculation. While this alone is still not adequate for simulation of a complete spray, the unique methodology described previously will permit a quasi-axisymmetric model to be developed.

With these ideas in mind, we focus on a single drop at some arbitrary location within the spray as shown in Fig. 4.

We presume a coordinate system moving with the drop in a Lagrangian fashion. The x axis is aligned with the drop’s velocity vector such that drag forces act along this axis and “lift” forces act along the accompanying y axis. Note that a lift force can be present since the pseudo-fluid velocity vector will generally not be aligned with the droplet velocity vector (as shown in Fig. 4). This situation arises due to the fact that a group of droplets is present; local pseudo-density gradients manifested by the presence of neighboring droplets will account for droplet/wake interactions and other group dynamic effects. Assuming the drop is much denser than the surrounding gas, we can effectively neglect unsteady virtual mass and Basset forces such that drag and lift are the only forces acting on the drop. Under this situation, Newton’s

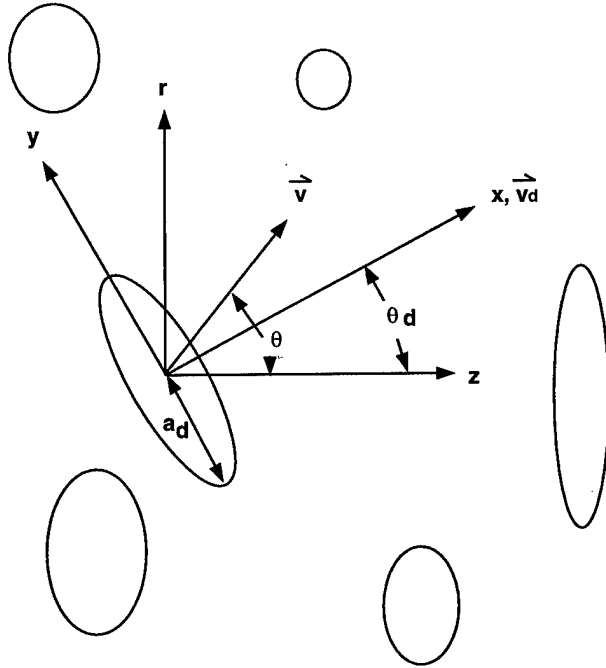


Figure 9: Motion of a Typical Drop within the Spray. Local Properties of the Pseudo-Fluid (\vec{v}) are Assumed to be Known as a Result of Solution of Navier-Stokes Equations

second law gives:

$$M_d \frac{d^2 x}{dt_d^2} = C_D A_D q \quad (1)$$

$$M_d \frac{d^2 y}{dt_d^2} = C_L A_L q \quad (2)$$

where M_d is the mass of the droplet, C_D and C_L are drag and lift coefficients, and t_d is the time as measured from the launching point for a given droplet. Assuming the droplet deforms into an ellipsoid, the effective cross-sectional areas A_D and A_L can be established using the initial and current droplet radii. Determination of the effective dynamic pressure acting on the drop (q) is not trivial in this case since the velocity returned from the Navier Stokes solver (\vec{v}) is a reflection of the local pseudo-density and not the density of the disperse phase. We propose to initiate our developments assuming:

$$q = \frac{\rho_g}{2} [(|\vec{v}_d| - |\vec{v}|) (|\vec{v}_d| + |\vec{v}|)] \quad (3)$$

This form effectively treats the pseudo-fluid velocity, \vec{v} , as that of a disperse phase, but it does provide the correct asymptotic limits for both dilute and very dense regions within the spray. In the dilute region of the spray ($\rho \rightarrow \rho_g$, $|\vec{v}| \rightarrow 0$), and the drag on

the drop is equivalent to a single drop propagating into a quiescent gas. In the dense region of the spray ($\rho \rightarrow \rho_l$, $\vec{v} \rightarrow \vec{v}_d$ and Eq. 6 reduces to $q = 0$ so that the drag vanishes in this limit. Note that the assumed form for q incorporates the "blockage effect" realized when a droplet is traveling in the wake of one or more other droplets. Since there is little research available to draw upon for further insight, the relevancy of Eq. 6 will have to be demonstrated as a part of the model development. Using this methodology and empirical data for force coefficients, one can integrate the trajectory of any droplet in the flow. To track the droplet deformation with time, we propose to use the technique of Ibrahim, et. al⁴⁹. Knowledge of the droplet deformation can be used to set breakup criteria in the secondary atomization model described below.

Droplet Collision/Secondary Atomization

Droplet/droplet collisions are known to be an important physical process occurring within a spray. Since droplets in the dilute region are decelerated due to the higher drag with the gaseous phase, they are continually subject to collisions with faster moving droplets emanating from the interior of the spray. Important momentum exchange and secondary atomization takes place as a result of this process.

Due to the recent basic research efforts in Professor Law's group at Princeton^{37,38}, we are in a good position to account for these physical processes in the proposed model. The Princeton research has shown that the collision process can be characterized in terms of a collision parameter, B , and the effective Weber number based on the relative collision velocity, We_c :

$$B = 2X/(d_1 + d_2) \quad We_c = \rho_l (d_1 + d_2) v_c^2 / (2\sigma) \quad (4)$$

where X is distance between droplet centers at the impact point, d_1 and d_2 are the diameters of the colliding drops, and v_c is the relative collision velocity. The type of liquid and overall pressure level have also been shown to be important in the collision process; at higher pressures the results appear to be relatively insensitive to this parameter.

Both virgin droplets and those formed as a result of a collision process are subject to secondary atomization caused by interaction with the gaseous phase. Within the past few years, much quantitative information regarding this process has been developed, primarily by Professor Faeth's research group at Michigan. Results from these studies^{39,40} provide predicted droplet sizes as a function of the size of the parent drop and the effective Weber and Ohnesorge

numbers characterizing the initial aerodynamic conditions to which the droplet was subjected.

There are two problems in using these data directly. Since the experiments were conducted by exposing the droplet to a uniform flow behind a weak shock wave, the droplet senses a dynamic pressure which is a maximum at the initial stages of the trajectory. In a dense spray, the droplet is shielded such that the dynamic pressure may be an increasing function of time. Therefore, it is not immediately clear how to characterize the Weber and Ohnesorge numbers under these conditions. This issue will need to be resolved through a series of numerical experiments in which effective Weber and Ohnesorge numbers are utilized to characterize the process.

The second problem arises from the breakup criteria utilized in the experiments. Many previous experiments using single droplets exposed to decaying dynamic pressure histories show that breakup occurs at a specific dimensionless time. Since the droplets emanating from the spray are subjected to a different dynamic pressure history, we propose to utilize a breakup criteria based on the overall deformation of the drop.

Pseudo-Density Routine

Through the use of droplet dynamics module, we should be able to determine the droplet size distribution throughout space (r, z) at any instant in time. By determining the liquid volume in any fixed sample volume, V_s , we can directly calculate ρ :

$$\rho \equiv V_l/V_s \quad (5)$$

where V_l is the total liquid volume lying within the selected sample volume. The main challenge lies in picking a sample volume which is small enough to reflect local flowfield conditions, yet large enough to permit ρ to vary smoothly.

Figure 6 describes the methodology for determining the local pseudo-density given at sample radius, R_s . The quantity R_{di} is the distance to droplet "i" as measured from the center of the sample volume. We must take into account the three-dimensionality introduced by the droplet field since the droplet volume lies outside the infinitely-thin computational plane. Moreover, we must consider droplets in adjacent planes which enter the assumed sample volume in order to get an accurate reflection of the local pseudo-density.

If we choose an R_s value, then we can evaluate ρ by adding up all droplet volumes which lie in the sphere

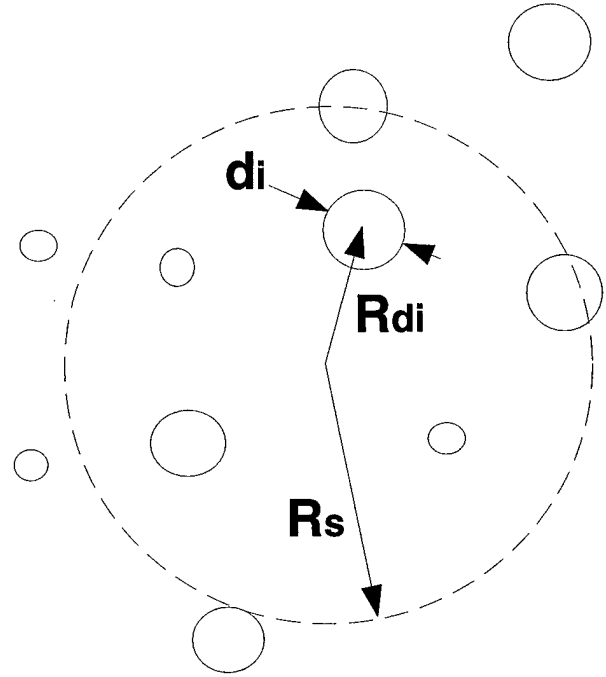


Figure 10: Determining the Local Pseudo-Density by Searching for Droplets which are Included in the Assumed Sample Volume. Droplets in Adjacent Planes also must be Considered in this Calculation.

of influence:

$$\rho = \frac{1}{\frac{4}{3}\pi R_s^3} \sum_{i=1}^n \frac{\pi}{6} d_{di}^3 \quad R_{di} < R_s \quad (6)$$

In general, there will be droplets which intersect the boundary R_s , but we will neglect this factor by accepting only droplets whose center lies within the stated boundary. On average this approach is justified since it will be equally likely for the droplet center to lie on either side of this boundary.

At the present time, we have completed preliminary versions of all the elements of the droplet dynamics module and have a capability to track of the order of 10^5 droplets in the computational plane. In addition, droplet collision/coalescence and secondary atomization submodels are nearly complete. A sample calculation for droplets entering a vacuum (i.e. no drag model) is shown in Fig. 11. Here, the evolution of the spray is detailed in a series of images at different times from the injection event. When complete, we will be able to build up databases of complete spray statistics (drop size and velocity distributions) at arbitrary axial or radial stations.

We anticipate that the model will be integrated with the viscous flow solver sometime this fall and checkout of test cases will begin in early 1999. When

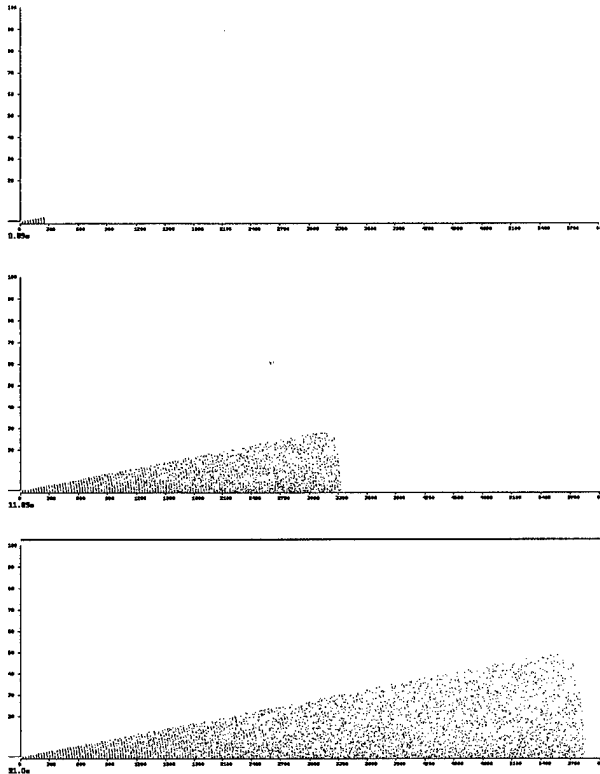


Figure 11: Sample Result of Dense Spray Model Depicting Droplet Field Developing in Time.

complete, the model will be capable of addressing a wide array of spray problems due to its general nature.

Conclusions

This paper has summarized both current and future efforts in the modeling of primary atomization processes with emphasis on liquid rocket engine applications. The 3-D boundary element model is complete, but will require surface fitting and regridding modules to become a truly effective tool. Models based on a pseudo-density formulation of the Navier-Stokes equations show much promise for these complex two-phase flows. We have successfully used such a model to describe viscous, unsteady, cavitating internal injector flows. Using similar notions, we are currently developing the first model capable of investigating the fully coupled dynamics of a dense spray under both quasi-steady and unsteady conditions. This general tool should be of great interest to the atomization community when completed and validated against experimental results.

Acknowledgement

The authors gratefully acknowledge the support of this work by the Air Force Office of Scientific Research under contract number F49620-96-1-0239 under the project management of Dr. Mitat Birkan.

References

1. Harrje, D. T. and Reardon, F. H., ed., *Liquid Propellant Rocket Combustion Instability*, NASA SP-194, 1972.
2. Jensen, R., (Ed.), "JANNAF Subcommittee on Combustion Stability - Annual Report," 27th JANNAF Combustion Meeting, Cheyenne, Wyoming, 1990.
3. Huynh, C., Ghafourian, A., Mahalingam, S., and Daily, J. W., "Combustion Design for Atomization Study in Liquid Rocket Engine," AIAA 92-0465, 1992.
4. Miesse, C. C., "The Effect of Ambient Pressure Oscillations on the Disintegration and Dispersion of a Liquid Jet," *Jet Propulsion*, October 1955, pp. 525-534.
5. Miesse, C. C., "Correlation of Experimental Data on the Disintegration of Liquid Jets," *Industrial and Engineering Chemistry*, Vol. 47, No. 9, 1955, pp. 1690-1701.
6. Spangler, C. A., Hilbing, J. H., and Heister, S. D., "Nonlinear Modeling of Jet Atomization in the Wind-Induced Regime", *Physics of Fluids*, V 7, No. 5, pp 964-971, 1995.
7. Hilbing, J. H., Heister, S. D., and Spangler, C. A., "A Boundary Element Method for Atomization of a Finite Liquid Jet", *Atomization and Sprays*, V 5, No. 6, pp 621-638, 1995.
8. Hilbing, J.H., and Heister, S.D., "Droplet Size Control in Liquid Jet Breakup," *Physics of Fluids*, V 8, No. 6, pp. 1574-1581, 1996.
9. Heister, S. D., Rutz, M., and Hilbing, J., "Effect of Acoustic Perturbations on Liquid Jet Atomization", *Journal of Propulsion and Power*, V13, No. 1, pp. 82-88, 1997.
10. Heister, S. D., "Boundary Element Methods for Two-Fluid Free Surface Flows", V19, No. 4, *Engineering Analysis with Boundary Elements*, pp. 309-317, 1997.

11. Hilbing, J. H., and Heister, S.D., "Nonlinear Simulation of a High-Speed, Viscous, Liquid Jet", *Atomization and Sprays*, V 8, pp. 155-178, 1997.
12. Rump, K. M., and Heister, S. D., "Modeling the Effect of Unsteady Chamber Conditions on Atomization Processes", *Journal of Propulsion and Power*, To Appear, 1998.
13. Chen, Y., and Heister, S. D., "Two-Phase Modeling of Cavitating Flows", *Computers and Fluids*, V 24, No. 7, pp 799-809, 1995.
14. Chen, Y., and Heister, S. D., "Modeling Hydrodynamic Non-Equilibrium in Bubbly and Cavitating Flows", *Journal of Fluids Engineering*, V 118, No. 1, pp 172-178, 1995.
15. Chen, Y. and Heister, S. D., "Modeling Cavitating Flows in Diesel Injectors", *Atomization and Sprays*, V6, pp 709-726, 1996.
16. Yang, H. Q., "Asymmetric Instability of a Liquid Jet," *Physics of Fluids*, pp. 681-689, 1992.
17. Chahine, G. L., "A Numerical Model for Three-Dimensional Bubble Dynamics in Complex Configurations," *22nd. American Towing Tank Conference*, 1989.
18. Henry, Mark E. *An Experimental Investigation of a Cavitation Slot Orifice*, Thesis, May 1997.
19. Jiang, Y.J., Umemura, A., and Law, C.K., "An Experimental Investigation on the Collision Behavior of Hydrocarbon Droplets", *J. Fluid Mech.*, 234, 171-190, 1992.
20. Qian, J., and Law, C.K., "Regimes of Coalescence and Separation in Droplet Collision", *J. Fluid Mech.*, 331, 59-80, 1997.
21. Hsiang, L.-P. and Faeth, G. M., "Drop Properties After Secondary Breakup," *Int. J. Multiphase Flow*, V 19, No. 5, 1993.
22. Hsiang, L.-P. and Faeth, G. M., "Near-Limit Drop Deformation and Secondary Breakup," *Int. J. Multiphase Flow*, Vol. 18, No. 5, 1992.
23. Krzeczkowski, S. A., "Measurement of Liquid Droplet Disintegration Mechanisms," *Int. J. Multiphase Flow*, Vol. 6, 1980.
24. Liu, Z, and Reitz, R., "Experimental Assessment of Shear or Boundary Layer Stripping Theories of High Speed Liquid Drops", *ILASS-97 Conference*, 1997.
25. Yang, V., Hsiao, G.C. and Shuen, J.S., "Droplet Behavior at Supercritical Conditions", *Recent Advances in Spray Combustion (Vol. 1)*, AIAA Volume 166, pp 413-437, 1996.
26. Abramzon, B., and Sirignano, W. A., "Droplet Vaporization Model for Spray Combustion Calculations", *Int. J. of Heat and Mass Transfer*, V32, No. 9, 1989.
27. Faeth, G.M., "Evaporation and Combustion in Sprays", *Prog. Energy Combustion Sci.*, 9, 1-76, 1983.
28. Faeth, G.M., "Mixing, Transport, and Combustion in Sprays", *Prog. Energy Combustion Sci.*, 13, 293-345, 1987.
29. A. A. Amsden, P. J. O'Rourke, and T. D. Butler, *KIVA-II - A Computer Program for Chemically Reactive Flows with Sprays*, Los Alamos National Labs., LA-11560-MS, 1989.
30. Ibrahim, E.A., Yang, H.Q., and Przekwas, A.J., "Modeling of Spray Droplets Deformation and Breakup", *J. Propulsion and Power*, 9, 227-239, 1993.